Upper Limits on Inclusive Branching Fractions to Narrow States in Radiative J/ψ Decays

Thesis by

Gregory P. Dubois

In Partial Fulfillment of the Requirements
for the Degree of
Doctor of Philosophy

California Institute of Technology
Pasadena, California

1992
(Defended February 4, 1992)

In memory of my mother and my father

Acknowledgments

As my graduate career has covered a remarkably long period, there are many more people who have touched my work and my life during these years in some meaningful way than I possibly can acknowledge adequately here.

David Hitlin was the person who interested me in Mark III, and through it introduced me to the world of experimental physics, when I asked him about a few pictures he had displayed on his office door of the experiment's first recorded events. I would like to thank him, once again, for seizing that moment and for bringing me into this wonderful enterprise. His keen insight into the important physics issues in any problem has been an inspiration, and he has been consistently both challenging and supportive throughout the years.

Bill Wisniewski, with whom I worked closely on many aspects of this experiment, provided inspiration and direction through his consistent and careful focus on an understanding of real-world detector systems, with all the problems and peculiarities never seen in the textbook and on the test bench. I most especially value his emphasis on understanding the performance of an experiment by letting the raw data tell its own story. He has been of material assistance throughout my work on this thesis, particularly in debugging the drift chamber and in providing new track dictionaries, and ultimately and essentially in helping me maintain my focus and complete the task. I enjoy working with him, and he has also been a great friend.

My long-time officemate and coworker, Chris Matthews, I must above all thank for his patience, particularly during our work on the data acquisition system. He has been a consistent source of interesting and productive ideas, of encouragement, and of friendship.

To single out only a few of the many members of the Mark III group with whom I have had the privilege to have worked is a difficult task. Nonetheless, I find in looking

back that I especially appreciate having had the collaboration and the companionship of Kirk Bunnell, Dan Coffman, Dave Coward, Al Odian, and Walter Toki.

Toby Burnett, Ron Cassell, Bijan Nemati, Larry Parrish, and Yanong Zhu all made important contributions to the J/ψ data reprocessing which absorbed so much of my time and energy. I enjoyed working with them, and I thank them for their efforts.

Many more people, of course, were involved in the design and construction of Mark III. They, and the dedicated SPEAR operations staff, have my great appreciation. I would also like to acknowledge the patience of Caltech, which unaccountably waited for me to finish, and my once and future colleagues at Oxford, who waited for me to return.

To my friends outside the circle of Mark III I owe an enormous debt of gratitude, especially to Jim Fanson, Helene Schember, and Steven Surtshin, for their inspiration, warmth, faith, encouragement, and understanding. David Wood has enlivened the last two years and provided the crucial distractions that allowed me to refocus my energies. Ruth McLay has played a very special role in my life in these final years, and although we are always amazed at how little we actually see of each other, her friendship has helped me through the darkest hours and made me appreciate the brightest ones all the more.

Although we wish it might have been for happier reasons, my sister and I have drawn closer together in the past year; this, and her wonderfully positive spirit, buoyed me up on many a frustrating day.

For my mother, whose love and wisdom never failed me, I can find no words to record here adequate to express my feelings. I could never have seen this project through without her. I wish she could have been here for its conclusion.

Abstract

The inclusive photon energy spectrum arising from J/ψ decays is studied in a sample of 4.83×10^6 produced J/ψ's, with the very good energy resolution available through the observation of converted photons in the Mark III spectrometer. The spectrum is inspected for evidence of monochromatic lines due to two-body radiative J/ψ decays to narrow states. The decays $J/\psi \rightarrow \gamma + \eta'(958)$ and $J/\psi \rightarrow \gamma + \iota/X(1450)$ are observed with limited statistical significance. No evidence is found for any other statistically significant structure in the inclusive spectrum. Upper limits are set on the branching fractions for the observed decays, as well as for the decays $J/\psi \rightarrow \gamma + \theta/f_0(1710)$ and $J/\psi \rightarrow \gamma + X(2230)$.

Contents

Part I Introduction

Part II The Mark III Experiment

Part III Inclusive Photon Data Analysis

List of Figures

List of Tables

Nomenclature and Definitions

Detector Coordinates The standard coordinate system used for the Mark III experiment is Cartesian and right-handed. The $+z$ axis is defined to be in the direction of travel of the positron beam; the $+y$ axis points upward, perpendicular to the plane of the storage ring; and the $+x$ axis points toward the center of the ring. The origin of these coordinates is at the nominal beam collision point; however, the actual collision point may be displaced from the origin by distances of order 10^{-3} m.

Spherical (r, θ, ϕ) and cylindrical (ρ, ϕ, z) coordinates are also used, defined in the usual way with respect to the standard Cartesian coordinates. A related variable often used in the discussion of particle tracks in the apparatus is the **dip angle**, λ, defined as $\lambda \equiv \frac{\pi}{2} - \theta_{polar}$.

Charged Track Parameters Charged tracks detected by the drift chamber system are parametrized by five quantities. These must be defined with respect to an implicit reference point, typically either the origin of the detector coordinate system, the measured true beam collision point, or the location of a secondary vertex. The track parameters are defined in terms of the point (x, y, z) on the track closest to the reference point (x_0, y_0, z_0), and the momentum (p_x, p_y, p_z) of the track evaluated at this location.

Three parameters describe the momentum: the curvature, κ, defined as $\kappa \equiv 1/p_{xy} = (p_x^2 + p_y^2)^{-\frac{1}{2}}$; the azimuthal angle, ϕ, of the momentum in the detector cylindrical coordinates; and the quantity s, the tangent of the dip angle, defined as $s \equiv tan\lambda \equiv p_z/p_{xy}$. The two remaining parameters describe the position of the track: the impact parameter, ξ, defined as $\xi \equiv ((x - x_0)^2 + (y - y_0)^2)^{\frac{1}{2}}$, and the z offset, η, defined as $\eta \equiv z - z_0$.

PART I
Introduction

Chapter 1 Theoretical Considerations and Experimental Review

Section 1 Overview

The startling discovery of the J/ψ in 1974,[1, 2] followed by the discovery of the predicted[3] charmed D mesons in 1976,[4, 5] was an important step in the development of confidence in the quark model, and provided a satisfying confirmation of the GIM mechanism[6] in weak decays.

In the seventeen years that have followed, the charmonium and charmed meson systems have continued to be of great interest. The weak decays of the D mesons have been studied in great detail, providing insight into the heavy quark decay process, while the study of the charmonium states has illuminated the QCD quark binding force.

The study of the J/ψ itself has contributed something more. Due to its ease of production, its narrow width, and its copious hadronic decay modes, it has provided a laboratory for the study of many of the light mesons, and a window on the possible existence of non-$q\bar{q}$ states.[7, 8]

The decays of the J/ψ occur through four principal channels: the hadronic decay through a three gluon intermediate state (Figure 1.1a); the electromagnetic hadronic decay through a virtual photon (Figure 1.1b); the leptonic decay through a virtual photon (Figure 1.1c); the radiative hadronic decay through a two gluon intermediate state (Figure 1.1d); and the M1 radiative transition to the η_c (Figure 1.1e). The branching fractions for these channels, respectively, are approximately 60%, 18%, 13%, 8%, and 1%. The hadronic decays are suppressed by the OZI (Okubo-Zweig-Iizuka) mechanism,[9, 10, 11] since the mass of the J/ψ is below the threshold for the production of charmed D meson pairs. This permits the other categories of decays a larger fraction of the total width of the J/ψ than might be expected solely from the ratio of the strong and electromagnetic coupling constants.

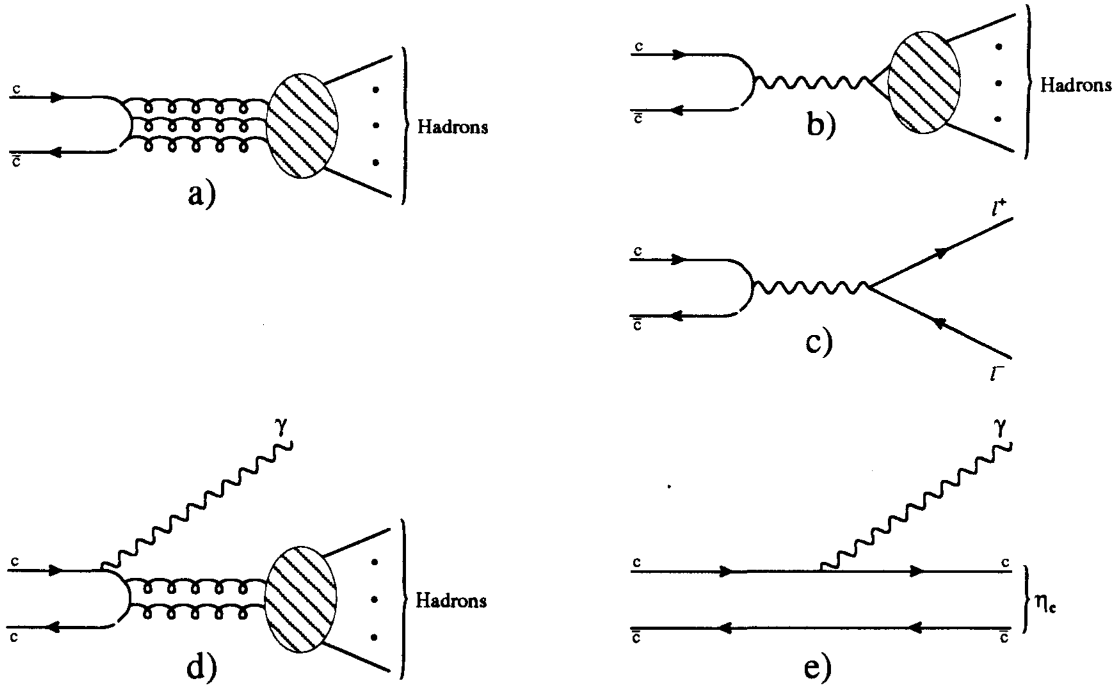

Figure 1.1 J/ψ decay Feynman diagrams: a) strong hadronic; b) electromagnetic hadronic; c) leptonic; d) radiative hadronic; e) M1 radiative transition to η_c.

The radiative hadronic decay channel is the subject of this thesis; specifically the possibility of the production through this channel of non-$q\bar{q}$ states, such as gluonic mesons. We shall now review the known and predicted properties of J/ψ radiative decays, discuss the question of the identification of observed hadronic resonances as candidate non-$q\bar{q}$ states, and present the current status of two sometime candidates, the $\iota/X(1450)$ system and the $\theta/f_0(1710)$.

Section 2 The J/ψ Radiative Decay

The process $J/\psi \longrightarrow \gamma + gg$ is amenable to calculation within the framework of perturbative QCD[8]. The radiative partial width obtained, to first order, is

$$\Gamma(J/\psi \to \gamma gg) = \frac{32}{9}(\pi^2 - 9)\alpha_s^2 \alpha e_c^2 \frac{|\Psi(0)|^2}{m_c^2}(1 - 0.9\alpha_s/\pi),$$

where α_s is the strong interaction coupling constant, α is the electromagnetic coupling constants, e_c and m_c are the charge and mass of the charmed quark, and $\Psi(0)$ is the J/ψ quark wave function at the origin. In the particular convention used for the first order corrections in this and the following equations, α_s is to be evaluated at $q^2 = M_{J/\psi}^2$. It should be noted that, while the value of α_s in this region of q^2 is small enough, ~ 0.15, that the perturbation series may be expected to converge, it is still sufficiently large that this first-order calculation cannot be expected to provide any more than an approximation to the true differential cross-section.

The three-gluon hadronic width is, to first order,

$$\Gamma(J/\psi \to ggg) = \frac{40}{81}(\pi^2 - 9)\alpha_s^3 \frac{|\Psi(0)|^2}{m_c^2}(1 + 4.9\alpha_s/\pi),$$

yielding a ratio

$$\frac{\Gamma(J/\psi \to \gamma gg)}{\Gamma(J/\psi \to ggg)} = \frac{16}{5}\frac{\alpha}{\alpha_s}(1 - 5.8\alpha_s/\pi),$$

which evaluates to approximately 0.08, somewhat below the observed ratio of ~0.13.

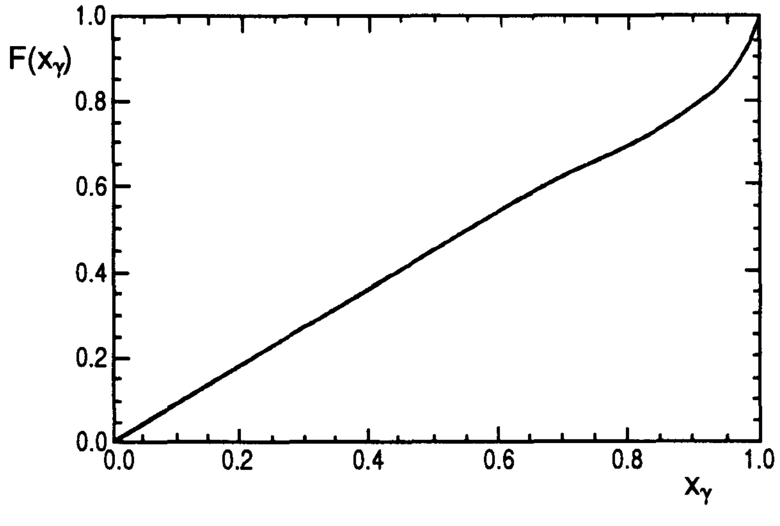

Figure 1.2 Perturbative QCD prediction for the radiative photon spectrum in J/ψ decays.

The shape of the radiative photon spectrum may also be predicted, using perturbative techniques. The result[12] is a spectrum nearly proportional to $x_\gamma \equiv 2E_\gamma / M_{J/\psi}$, as shown in Figure 1.2. Several experiments[13, 14, 15, 16] have measured this spectrum; the result of the Mark II analysis[16] is shown in Figure 1.3. The prediction from Reference [12], convoluted with the experimental resolution, is shown as the dashed line in the figure. The observed spectrum is clearly considerably softer than the perturbative prediction.

Several attempts have been made to refine the calculations of the spectrum (see, for instance, References [17, 18]), but although these have yielded slightly softer spectra, they continue to be in conflict with the data. A recent study[19] has attempted a new approach, a nonperturbative calculation using a QCD multipole expansion. The authors do not expect this calculation to be valid for $x_\gamma < 0.8$. However, their result, shown as the solid curve in Figure 1.3, appears to be in good agreement with the data for the highest values of x_γ.

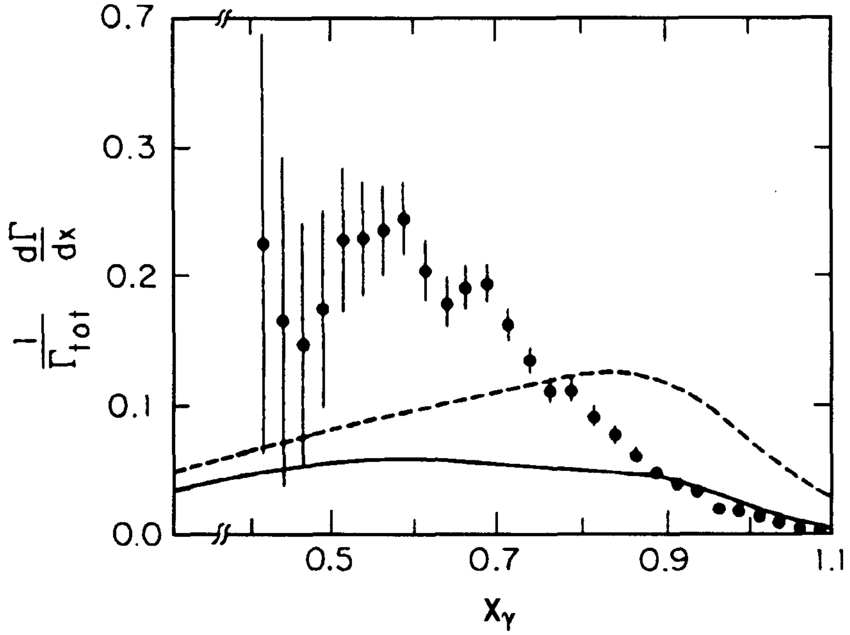

Figure 1.3 Observed radiative photon spectrum, with theoretical predictions, adjusted for the experimental energy resolution, overplotted. Dashed line: perturbative QCD; solid line: high-x QCD multipole expansion.

There does not yet appear to be any satisfactory calculation able to reproduce the entire spectrum; this is not especially surprising, however. Ultimately we do expect the presence of resonances coupling to the *gg* intermediate state to affect the shape of the spectrum. A full calculation of the spectrum, then, would depend on a full understanding of low-q^2 *gg* hadronization. The only currently plausible way to obtain this information is through lattice gauge theory calculations, but only with several orders of magnitude of improvement in computing capacity over that presently available.

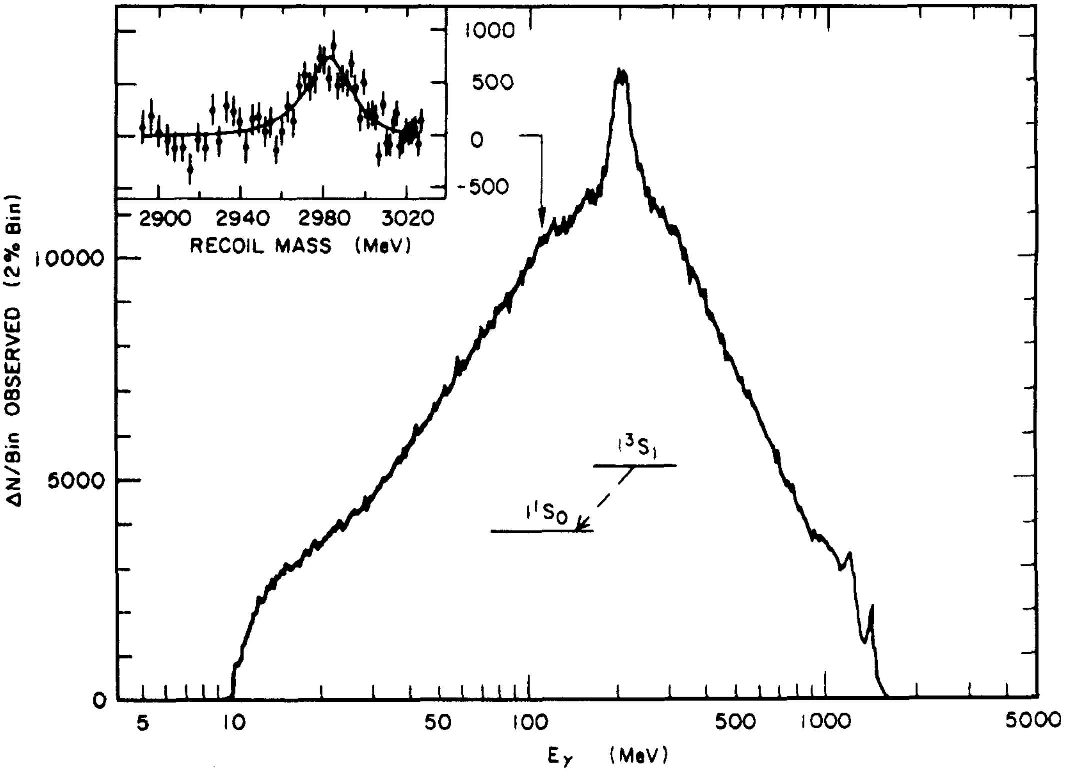

Figure 1.4 Inclusive photon spectrum observed in J/ψ decays by the Crystal Ball experiment.

The Crystal Ball experiment has examined the inclusive photon spectrum from J/ψ decays, but without reporting a quantitative analysis of the features in the spectrum.[20] Their result is shown in Figure 1.4. This spectrum can not be compared directly with those above. It is not fully corrected to remove the contributions of secondary photons, *e.g.*, those from π^0 decays. The most interesting feature of the spectrum is the presence of several apparent peaks near the end point of the spectrum, corresponding to low recoil masses. (The peak at 0.2 GeV is an artifact resulting from contamination of the data sample by charged particle tracks.) Unfortunately, no quantitative analysis of these peaks has been presented. The two particularly clear peaks appear to correspond to the decays $J/\psi \rightarrow \gamma\iota/X(1450)$ and $\gamma\eta'(958)$. A broad shoulder below these peaks is at an energy corresponding to recoil masses of approximately 1.7 GeV/c^2.

Section 3 Glueball Properties and Identification

The non-Abelian nature of the QCD Lagrangian implies the existence of a gluon-gluon interaction at tree level, in contrast to QED where photon-photon interactions occur only at the one-loop level or higher. It is therefore expected that there may exist bound states consisting solely of gluons. The possible properties of such states have been a subject of considerable study. The name *glueball* for such states has been accepted widely.

It is possible to construct color singlet states from still other combinations of quarks and gluons, such as $q\bar{q}g$ and $q\bar{q}q\bar{q}$, and others of progressively greater complexity. Such states are collectively known as *hybrids*. There is considerable disagreement on the possible properties of such states, or indeed whether they would be resonant bound states at all.

Calculations of the properties of bound states of gluons (and light quarks) in QCD are in the low-q^2 regime, where, in light of the approximate unit magnitude of the QCD coupling constant, non-perturbative methods are required. Unfortunately, while much progress has been made in this area, it remains challenging to predict accurately the masses of even the well-established light-quark bound states, let alone hypothetical glueball or hybrid states.

Nonetheless, enough has been learned about the theoretical mass spectrum of these objects, as well as their widths and decay properties, to serve as a guide to experimental efforts. The lowest-mass states in the various possible spin-parity configurations are all generally expected to lie in the 0.5–2 GeV/c^2 regime. This mass region is easily accessible in J/ψ decays; moreover, there is an additional factor which may make the J/ψ an especially interesting laboratory for the search for glueballs. Various workers have suggested that the color-singlet two-gluon intermediate state in the radiative hadronic decay of the J/ψ should favor the formation of glueballs. This "enhanced glueball production" hypothesis has focused interest on J/ψ radiative decays for many years.

The identification of an observed state as a glueball is fraught with difficulty. The predicted spin-parity assignments, widths, and decay patterns of glueballs are different from those of $q\bar{q}$ states, but not so much as to be truly distinctive. Moreover, glueballs are expected to mix with $q\bar{q}$ states of the same spin-parity, further complicating the picture. The only exception to this is for glueball states with spin-parity assignments not accessible to $q\bar{q}$ states, the so-called *oddballs*. Discovery of a resonance with such a "forbidden" spin-parity would be clear evidence for a non-$q\bar{q}$ state, though determination of its nature (*e.g.*, glueball or $q\bar{q}g$ hybrid) would require further study.

Although the identification of a glueball by its properties alone appears to be a difficult task, there is a further useful handle. The existence of a glueball, whether in a pure state or mixed with a conventional $q\bar{q}$ meson, would add an additional state to those expected in a given mass range for a specific spin-parity assignment. Assuming that the relevant $q\bar{q}$ nonets were well understood, with candidates identified for all predicted states, the existence alone of this "extra" state would be a significant signal of its possible exotic nature. Unfortunately, surprisingly few of even the ground-state meson nonets have been filled completely. While the $^{2S+1}L_J = {}^1S_0$ (pseudoscalar), $^3S_1$ (vector), $^1P_1$ (axial vector $C{=}-1$), and $^3P_2$ (tensor) nonets are well understood, the situation is less clear for the $^3P_0$ (scalar) and $^3P_1$ (axial vector $C{=}+1$) nonets, and very little is certain about D-wave (except for the $^3D_3$ nonet) or radially excited states. A search for "extra" states, therefore, requires considerable care to be taken in the evaluation of the reliability of the less well-established $q\bar{q}$ meson nonet assignments.

Tables 1.1–1.4 display a summary of the current state of knowledge and speculation with respect to the identification of predicted $q\bar{q}$ meson quantum states with observed resonances. A new generation of hadron beam experiments and recent increases in the sophistication of analyses of the J/ψ data of the Mark III and DM2 experiments has greatly expanded and clarified this picture over the past several years, but much work remains to be done. The resonance names in the tables are taken from the current issue of the Review of Particle Properties.[21] Resonances listed with a "?" are those not considered "well established" by the Particle Data Group. The shaded locations in the tables are nonet assignments, currently considered ambiguous or questionable, which will be discussed in further detail below. Blank entries appear for other states with missing or unclear assignments. It should be noted that there are a large number of putative resonances reported in the 1.5–2.5 GeV/c^2 mass region, many of which could easily be assigned to entries in these tables. We do not lack for resonance candidates, on the whole, but rather for detailed information on the resonance widths and decay patterns, and for clear consistency between experiments.

Table 1.1 Ground states and first excited states of the L=0 $q\bar{q}$ meson nonets.

2^3S_1		$K^*(1370)$	$\omega(1390)$	$\phi(1680)$	1^{--}
2^1S_0	$\pi(1300)$	$K(1460)$?	$\eta(1295)$		0^{-+}

1^3S_1	$\rho(770)$	$K^*(892)$	$\omega(783)$	$\phi(1020)$	1^{--}
1^1S_0	π	K	η	$\eta'(958)$	0^{-+}
	I=1	I=½	I=0		

Table 1.2 Ground states and first excited states of the L=1 $q\bar{q}$ meson nonets.

3^3P_2		$K_2^*(1980)$			2^{++}
3^3P_1					1^{++}
3^3P_0		$K_0^*(1950)$			0^{++}
3^1P_1		$K_1(1650)$			1^{+-}

2^3P_2	$a_2(1320)$	$K_2^*(1430)$	$f_2(1270)$	$f_2'(1525)$	2^{++}
2^3P_1	$a_1(1260)$	$K_{1A}(1400)$	$f_1(1285)$		1^{++}
2^3P_0		$K_0^*(1430)$			0^{++}
2^1P_1	$b_1(1235)$	$K_{1B}(1270)$	$h_1(1170)$	$h_1(1380)$	1^{+-}
	I=1	I=½	I=0		

Table 1.3 Ground states of the L=2 $q\bar{q}$ meson nonets.

3^3D_3	$\rho_3(1690)$	$K_3^*(1780)$	$\omega_3(1670)$	$\phi_3(1850)$	3^{--}
3^3D_2		$K_2(1770)$			2^{--}
3^3D_1		$K^*(1680)$?			1^{--}
3^1D_2	$\pi_2(1670)$	$K_2(1580)$?			2^{-+}
	I=1	I=½	I=0		

Table 1.4 Ground states of the L=3 $q\bar{q}$ meson nonets.

4^3F_4	$a_4(2040)$?	$K_4^*(2045)$	$f_4(2050)$	$\xi/X(2230)$?	4^{++}
4^3F_3	$a_3(2050)$?	$K_3(2320)$?			3^{++}
4^3F_2					2^{++}
4^1F_3					3^{+-}
	I=1	I=½	I=0		

Section 4 The $\iota/E/X(1450)$ Question, and the 1^{++} and Radially Excited 0^{-+} Nonets

Much of the uncertainty in the identification of the resonances comprising the ground state 1^{++} nonet and the first radial excitation of the 0^{-+} nonet arises from a common source. There is a large quantity of experimental data, obtained from both hadron beam and J/ψ decay experiments, on a variety of apparent resonant structures in the 1.4–1.5 GeV/c^2 mass region, in both the $K\bar{K}\pi$ and $\eta\pi\pi$ final states. The number of true resonances in this region, and their quantum numbers, remain subjects of considerable interest.

The observation of structure near 1.4 GeV/c^2 in the $K\bar{K}\pi$ invariant mass spectrum in radiative J/ψ decays was first made by the Mark II experiment,[22] in an examination of the final state $K^o_S K^\pm \pi^\mp$. They were unable to determine a spin-parity assignment from their data, but tentatively identified the structure with the $E(1420)$, a state observed in hadronic interactions. At that time, the spin-parity of the E was not well detemined, but appeared likely to be 1^{++}. The Mark II measurement was soon reproduced by the Crystal Ball experiment[23] in the $K^+K^-\pi^o$ final state. A spin-parity analysis of their data returned the assignment $J^{PC} = 0^{-+}$ for the state. In light of the conflict with the 1^{++} assignment for the $E(1420)$, the structure observed in radiative J/ψ decays was assumed to be a new resonance, given the name "ι".

The existence of structure in the 1.4 GeV/c^2 $K\bar{K}\pi$ invariant mass region in radiative J/ψ decays was readily confirmed by the Mark III experiment in an early analysis.[24] Assuming the observed structure, shown in Figure 1.5, originated from a single resonance, the following parameters were obtained, from the $K^0_S K^\pm \pi^\mp$ mode:

$$M = 1.456 \pm 0.005 \pm 0.006 \text{ GeV}/c^2$$

$$\Gamma = 0.095 \pm 0.010 \pm 0.015 \text{ GeV}/c^2$$

$$B(J/\psi \to \gamma X(1456)) \cdot B(X \to K\bar{K}\pi) = (5.0 \pm 0.3 \pm 0.8) \times 10^{-3},$$

where the isospin of X is assumed to be zero in correcting for other $K\bar{K}\pi$ final states. Consistent results were obtained from analysis of the $K^+K^-\pi^o$ and $K^0_S K^0_S \pi^o$ final states, confirming the $I = 0$ assumption.

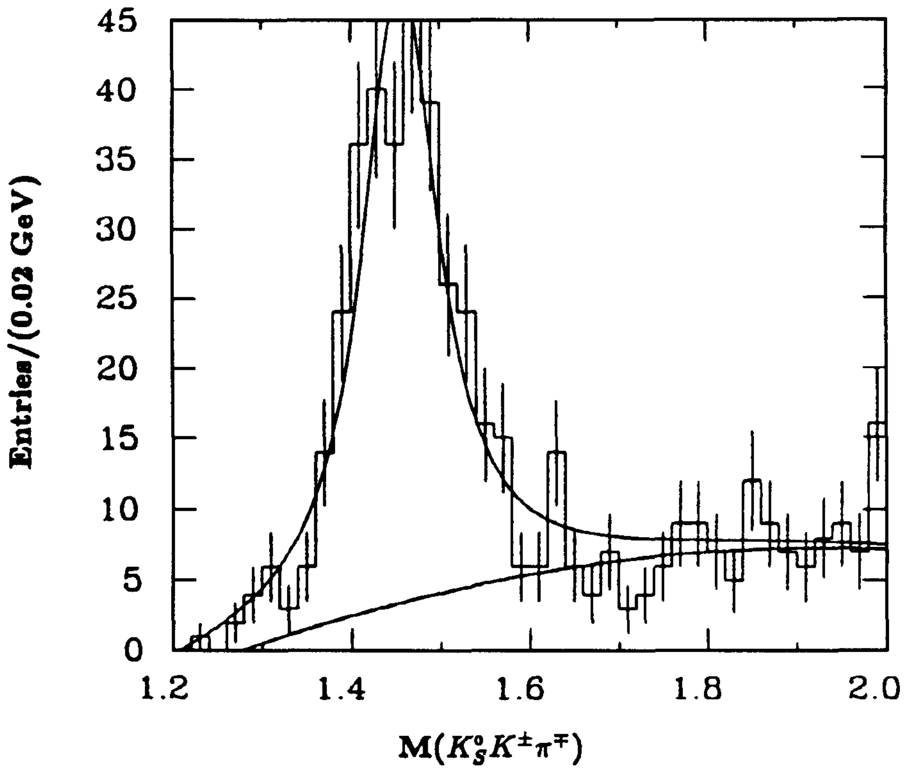

Figure 1.5 $K^0_S K^\pm \pi^\mp$ invariant mass spectrum observed in the initial Mark III analysis of $J/\psi \to K\bar{K}\pi$.

A preliminary analysis of the $K\bar{K}\pi$ Dalitz plot, considering the possible $a_0(980)$ and $K^*\bar{K}$ intermediate states,[1] produced the result:

$$\frac{B(X \to K^*\bar{K})}{B(X \to K\bar{K}\pi)} < 0.35, \text{ at the 90\% C.L.}$$

Using a three-body helicity formalism, a spin-parity analysis was performed on this data set. This technique does not depend on the knowledge of any possible two-body intermediate states in the decays of X. A pseudoscalar spin-parity assignment was found to be preferred.

The pseudoscalar assignment, together with the limit on the $K^*\bar{K}$ branching ratio, continued to suggest that this state was unlikely to be the $E(1420)$.

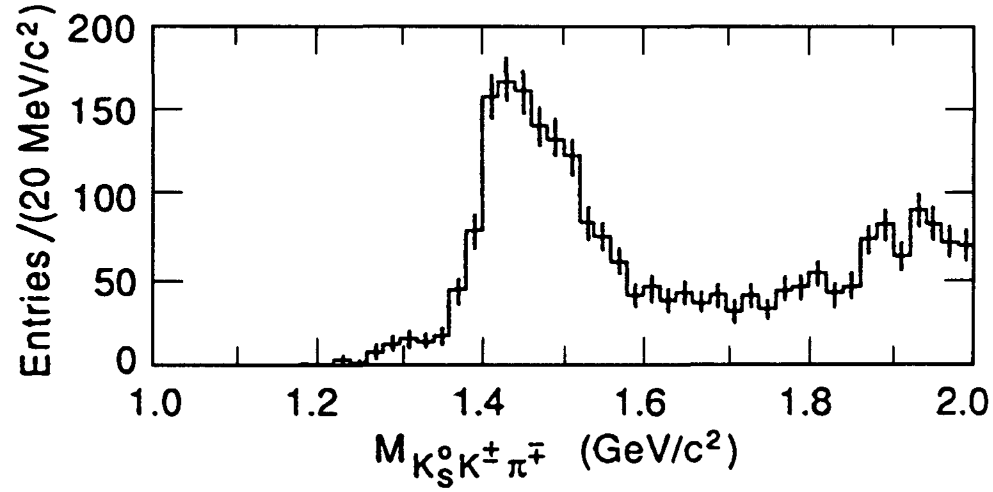

Figure 1.6 $K^0_S K^\pm \pi^\mp$ invariant mass spectrum observed in the published analysis of the full Mark III $J/\psi \to K\bar{K}\pi$ data sample.

Subsequently, analysis of the full Mark III J/ψ data sample has revealed the picture to be more complicated. With the increase in data sample size, it became clear that the shape of the peak in the $K\bar{K}\pi$ invariant mass (see Figure 1.6) was not consistent with interpretation as a single Breit-Wigner line shape. Furthermore, the structure of the

---

[1] The mention of $K^*\bar{K}$ also implies the charge-conjugated state $\bar{K}^*K$.

$K\bar{K}\pi$ Dalitz plot was found to vary from low to high masses within the peak. A partial-wave analysis[25] of the $K^0_S K^\pm \pi^\mp$ final state concluded that the data were best described using a combination of three decay channels, all proceeding to $K\bar{K}\pi$. Assuming the three channels represented the clustering of three resonances in the "ι" mass region, the intensity spectra resulting from the partial-wave analysis were fit, producing the resonance parameters and branching fractions shown in Table 1.5. Similar results have been obtained by the DM2 experiment.

Table 1.5 Results of Breit-Wigner fits to the intensity distributions from a partial-wave analysis of the 1.4 GeV/c^2 $K^0_S K^\pm \pi^\mp$ mass region in radiative J/ψ decays, from the Mark III analysis.

Amplitude	M (GeV/c^2)	Γ (GeV/c^2)	$10^3 \cdot B(J/\psi \to \gamma X) \cdot B(X \to K\bar{K}\pi)$
0^{-+} $a_0(980)\pi$	$1.416\ ^{+0.008}_{-0.008}\ ^{+0.007}_{-0.005}$	$0.054\ ^{+0.037}_{-0.021}\ ^{+0.013}_{-0.024}$	$0.66\ ^{+0.17}_{-0.16}\ ^{+0.24}_{-0.15}$
1^{++} $K^*\bar{K}$	$1.443\ ^{+0.007}_{-0.006}\ ^{+0.003}_{-0.002}$	$0.068\ ^{+0.029}_{-0.018}\ ^{+0.008}_{-0.009}$	$0.87\ ^{+0.14}_{-0.14}\ ^{+0.14}_{-0.11}$
0^{-+} $K^*\bar{K}$	$1.490\ ^{+0.014}_{-0.008}\ ^{+0.003}_{-0.016}$	$0.091\ ^{+0.067}_{-0.031}\ ^{+0.015}_{-0.038}$	$1.03\ ^{+0.21}_{-0.18}\ ^{+0.26}_{-0.19}$

Under the original interpretation of the $\iota/X(1450)$ signal as a single pseudoscalar resonance, its production with the largest single hadronic radiative branching fraction from the J/ψ was considered one of the strongest indicators for its consideration as a glueball candidate. With its reinterpretation as three resonances, each produced with a branching fraction smaller than that for the conventional decay $J/\psi \to \gamma\eta'(958)$, this is no longer a primary consideration. However, the proliferation of states in the 1.4 GeV/c^2 mass region raises new questions of possible "extra" states not classifiable into any of the expected $q\bar{q}$ nonets.

It is natural to attempt to identify the $J^{PC} = 1^{++}$ state at 1.443 GeV/c^2 with the well-established $f_1(1420)$.

Table 1.6 First radial excitation of the pseudoscalar $q\bar{q}$ meson nonet.

2^1S_0	$\pi(1300)$	$K(1460)$?	$\eta(1295)$	$\eta(1490)$	0^{-+}
	I=1	I=½	I=0		

Table 1.7 Ground state and first radial excitation of the axial vector C=+1 $q\bar{q}$ meson nonet.

3^3P_1					1^{++}
2^3P_1	$a_1(1260)$	$K_{1A}(1400)$	$f_1(1285)$	$f_1(1420)$	1^{++}
	I=1	I=½	I=0		

Section 5 The $\theta/f_0(1710)$ Question, and the 0^{++} Nonet

The Crystal Ball experiment, in an analysis of the process $J/\psi \rightarrow \gamma\eta\eta$, reported[26] the existence of a peak in the $\eta\eta$ invariant mass distribution, with parameters $M = 1.640 \pm 0.050$ GeV/c^2 and $\Gamma = 0.220^{+0.100}_{-0.070}$ GeV/c^2. Assuming the data arose from the decay of a single resonance, which they named "θ", the results of their analysis favored a spin-parity assignment of 2^{++}. In light of the then-current predictions for the possible existence of tensor glueball states in this mass region, and the expectation that such states might be copiously produced in radiative J/ψ decays, this discovery occasioned considerable interest. Subsequently, the Mark II experiment reported[27] the observation of structure in the K^+K^- invariant mass distribution in the process $J/\psi \rightarrow \gamma K^+K^-$. In this analysis, the structure in the 1.5–1.8 GeV/c^2 mass region, identified with that seen by the Crystal Ball, was resolved into two peaks, one the previously known $f'(1525)$, and one new state, with parameters $M = 1.700 \pm 0.030$ GeV/c^2 and $\Gamma = 0.156 \pm 0.020$ GeV/c^2.

This observation has since been confirmed by the Mark III[28] and DM2[29] experiments, in both the K^+K^- and $K^0_SK^0_S$ final states. Spin-parity analyses performed by these experiments have not yielded entirely consistent results. The Mark III angular analysis reported in Reference [28] strongly favored $J^{PC} = 2^{++}$ for the 1.7 GeV/c^2 state, while the DM2 analysis was unable to distinguish between 0^{++} and 2^{++}. More recently, a moments analysis, taking full advantage of all the angular correlations in the decays, was performed by Mark III.[30] This analysis finds that the 1.7 GeV/c^2 peak in the $K\bar{K}$ mass spectrum is of a predominantly scalar, 0^{++}, nature, although it cannot entirely exclude the possibility of a small 2^{++} contribution.

All experiments' spin-parity analyses of the $f'(1525)$ region in $J/\psi \to \gamma K\bar{K}$ return $J^{PC} = 2^{++}$, as expected.

PART II
The Mark III Experiment

Chapter 2 The SPEAR Storage Ring

SPEAR is an electron storage ring located at the Stanford Linear Accelerator Center. Following a 20 month construction period, it began operation in April of 1972.[31, 32, 33] Initially, the maximum center-of-mass energy for e^+e^- colliding beams was approximately 5.5 GeV. With the installation of a new, higher-power RF acceleration system in October of 1974, this limit was raised to 7.4 GeV.[34] In November of 1974, using the SLAC-LBL magnetic detector, the J/ψ particle was co-discovered at SPEAR.[2] Until the eventual termination of colliding beam operation, in 1988, the storage ring continued to produce a remarkable flow of discoveries and detailed information on the charmonium and open charm systems, as well as the τ lepton. (With a new synchrotron as a dedicated electron injector, SPEAR is presently continuing its highly successful career as a synchrotron radiation source.)

A selection of parameters of the storage ring are presented in Table 2.1, with emphasis on the values obtained when running at the J/ψ energy.[35, 36] The fractional energy spread per beam quoted in the table leads to a center-of-mass energy spread at the J/ψ of approximately 800 keV. As this is considerably larger than the intrinsic width of the J/ψ, the effective production cross-section is greatly reduced from its peak value. During typical running conditions for the Mark III experiment at SPEAR, the peak J/ψ production rate was approximately one per second.

The uncertainty in the absolute energy calibration of SPEAR is larger than the beam energy spread. Therefore, the beam energy setting for J/ψ running was chosen by performing an energy scan over the resonance, locating the point yielding the largest hadronic event rate. The SPEAR control system was then able to maintain the beam energy at this value to a typical precision of 250 keV over time scales of days to weeks. Additional scans were occasionally carried out following accelerator shutdowns, or in the

Table 2.1 Machine parameters of the SPEAR storage ring. Parameters whose value varies with energy are marked with a '*', and are evaluated for the single beam energy, 1.5485 GeV, corresponding to J/ψ production.

Center-of-mass energy	E_{CM}	2.5 - 7.4 GeV
Number of bunches	n	1
Crossing interval	Δt	781 ns
RF Harmonic Number	$f_{\mathrm{RF}}/f_{\mathrm{circ}}$	280
Circumference	$2\pi R$	234 m
Dipole bend radius	ρ	12.7 m
Crossing angle	θ_{cross}	0
Maximum beam injection energy		2.35 GeV
Peak luminosity*	$\mathcal{L}_{\mathrm{max}}$	4.5 × 10^{29} cm^{-2} sec^{-1}
Luminosity lifetime*	$\tau_{\mathcal{L}}$	$\sim$ 3 hr
Maximum beam current, per beam*	I_{max}	5 mA
Beam-beam tune shift*	ΔQ	$\sim$ 0.03
Synchrotron radiation energy loss, per turn, per beam*		40 keV
Polarization buildup time*	τ_{pol}	18.5 hr
Fractional energy spread, per beam*	δ_E	3.7 × 10^{-4}
Beam size at interaction point, horizontal	σ_x^*	$\sim$ 500 μm
Beam size at I.P., vertical	σ_y^*	$\sim$ 50 μm
Bunch length	σ_ℓ	4 cm

event the ratio of the hadronic event rate to the luminosity measured from small-angle Bhabha scattering appeared to have fallen, indicating a possible shift in energy away from the J/ψ production peak.

It is worth noting that there was no possibility of obtaining polarized J/ψ's through the radiative beam polarization mechanism, in view of the very long polarization buildup time at the necessary beam energy. The observation of the decay of polarized J/ψ's might, however, be an interesting goal for a future experiment, as the information available from such measurements would be of considerable assistance in determining the spin-parity of the decay products.

Chapter 3 Summary of Data-Taking

The Mark III experiment was proposed, and approved by SLAC, in 1978. The spectrometer was assembled in its initial configuration and first put into operation in the Fall of 1981. Following its shakedown run, data were collected at a variety of energies, as outlined in Table 3.1. The table displays the approximate dates, the nominal running points identified either by resonance name or specific energy, the integrated luminosity or, in the case of the narrow resonances J/ψ and ψ', the number of particles produced, and the range of run numbers covered by each running period. Run numbers are sequentially generated identifiers for intervals of active data-taking. The "runs" which these identify varied in duration from seconds to several hours. Typically, a run was a single continuous period of data-taking with stably colliding beams, ended by either the loss of the stored beams, the filling of a complete magnetic tape with logged data, or a detector failure. Run numbers not included in the table generally correspond to periods of non-production data taking or of debugging of the apparatus.

Table 3.1 History of Mark III Data Samples

Dates	C.M. Energy	N / Luminosity	Run Numbers
Spring 1982	J/ψ	0.92×10^6	421 – 921
Fall 1982	$\psi(3685)$	0.119×10^6	1012 – 1046
Fall 1982	$\psi(3770)$	1.51 pb^{-1}	1047 – 1312
Spring 1983	J/ψ	1.79×10^6	1324 – 1643
Spring 1983	$\psi(3770)$	3.89 pb^{-1}	1644 – 2085
Winter 1984	$\psi(3770)$	4.16 pb^{-1}	2219 – 2982
Spring 1985	J/ψ	3.04×10^6	3111 – 3867
Winter 1986	4.14 GeV	6.30 pb^{-1}	4094 – 4741
Fall 1988	$\psi(3685)$	0.202×10^6	5002 – 5269

The normalization for the J/ψ data is discussed in detail below. The sizes of the other data samples in Table 3.1 are taken from the following publications: ψ': Reference [37], 4.14 GeV: Reference [38], and $\psi(3770)$: Reference [39]. Since no officially sanctioned values for the sizes of the three individual $\psi(3770)$ data samples were ever published, the values in the table were obtained by scaling early estimates of their sizes so that their sum equalled the published integrated luminosity.

Section 1 Normalization of the J/ψ Data

In order to obtain the number of produced J/ψ's in each collected data sample, the following procedure was developed. The Spring 1983 data set was examined in detail. Each event was classified into one of several categories: one-prong, co-linear two-prong, non-co-linear two-prong, three-prong, and four-or-more-prong. A large sample of events in each of the categories but co-linear two-prong was visually scanned in order to evaluate the efficiency and error rates of the classification criteria and the levels of contamination by background events not arising from J/ψ decays.

The trigger efficiency for each category was obtained from a study of the Fall 1982 ψ' data set, using the decay mode $\psi' \to \pi^+\pi^- J/\psi$. Events containing a J/ψ were selected by an inclusive identification of $\pi^+\pi^-$ pairs with the unique momentum corresponding to a recoiling J/ψ. The $\pi^+\pi^-$ pair alone was required to have satisfied the trigger criteria. The recoil in these "tagged J/ψ" events was then inspected to determine its classification and whether it would have been sufficient to satisfy the trigger criteria in the absence of the $\pi^+\pi^-$ pair. Thus, a mean trigger efficiency for each category was obtained.

The number of events in each category was then corrected for the trigger efficiency and for the levels of background and systematic biases determined by the visual scan. Co-linear two-prong events were assumed to arise solely from the processes $J/\psi \to e^+e^-$

and $J/\psi \rightarrow \mu^+\mu^-$.[1] The number of $\mu^+\mu^-$ events was determined through an analysis with stringent classification criteria to require identified muons and reject cosmic ray events, corrected for the detection efficiency obtained from a Monte Carlo analysis. The number of e^+e^- events was derived by assuming the equality of the two leptonic branching fractions.

During the J/ψ data taking periods, the Mark III event trigger was not equipped to recognize events with no charged tracks in the final state. A estimate of (3.5±0.5)% for the total branching fraction to such final states was obtained by inspection of the "tagged J/ψ" data sample described above. Combining the hadronic and leptonic event counts with this correction, the Spring 1983 data sample was found to contain a total of $(1.79 \pm 0.11) \times 10^6$ produced J/ψ events. The error arises largely from the uncertainties in the background determination in the visual scan.

The J/ψ counts for the Spring 1982 and Spring 1985 data samples were obtained by scaling the Spring 1983 total by the relative numbers of detected $J/\psi \rightarrow \mu^+\mu^-$ events in each data sample. Including a small additional contribution to the errors from this inter-normalization procedure, the result for the full J/ψ data sample is:

$$N_{(1982,1983,1985)} = (5.75 \pm 0.43) \times 10^6.$$

This procedure is described in additional detail in Reference [40].

Section 2 Normalization for this Analysis

The analysis of J/ψ decays presented in this work uses only the Spring 1983 and Spring 1985 data samples. The Spring 1982 data, alone among all the samples in the table above, was taken with the detector, particularly the drift chamber, in a slightly different

---

[1] The $p\bar{p}$, $\pi^+\pi^-$, and K^+K^- decay modes were not taken explicity into account, but as the measured branching fractions for these modes total to ~1.5% of the sum of the two leptonic modes' branching fraction, the correction arising from this source would be negligible in view of the size of the error on the normalization.

configuration from the later data, one which precludes the use of the final version of the Mark III event reconstruction software. The early version that was originally used to reconstruct the Spring 1982 data has been exploited successfully in various physics analyses. However, the present analysis required several enhancements and modifications to the reconstruction software. Retrofitting these into the early software, or modifying the current software to allow reconstruction of data in the Spring 1982 configuration, would have been a difficult task, disproportionately so in view of the small relative size of that data sample.

Omitting the Spring 1982 data sample from the normalization procedure results in a count of produced J/ψ's of

$$N_{(1983,1985)} = (4.83 \pm 0.37) \times 10^6.$$

This is the number to be used in the present analysis.

Chapter 4 The Spectrometer

Section 1 History and Overview

The J/ψ was identified at SPEAR by the SLAC/LBL Magnetic Detector, now commonly known as Mark I. This was one of the first examples of the by-now ubiquitous *4π magnetic detector*—a device designed to observe, as far as possible, all the products of the beam collisions. Although this detector had very limited photon detection and particle identification capabilities, the discoveries it made possible proved the worth of the 4π concept and encouraged its further development.

This detector was followed at SPEAR in 1978 by the Mark II, an all-new construction which replaced Mark I's magnetostrictive spark chamber with one of the first large-scale cylindrical drift chambers, and added a liquid argon barrel electromagnetic calorimeter. After three very successful years at SPEAR, Mark II was moved to the new PEP storage ring to pursue the study of higher-energy collisions. When this move was planned, a follow-on magnetic detector was proposed for SPEAR, in recognition of the many interesting questions remaining in the charm energy region.

The inevitably named Mark III spectrometer was conceived as a general-purpose detector optimized for the SPEAR energy region. The primary design goal was the ability to reconstruct complete final states in charmed particle decays with high efficiency. This required uniform coverage of as great a fraction of the 4π sr solid angle as possible for both charged tracks and photons, high detection efficiency for low energy photons, and uniform and high-precision particle identification. These requirements led to the following more specific criteria: minimal mass for the inner support structures of the drift chamber; a drift chamber wire layout designed for redundancy and ease of track recognition; a highly efficient trigger with wide angular acceptance; a time-of-flight system with time resolution better than 200 ps; and an electromagnetic calorimeter inside the solenoid coil, with a minimal number of gaps in its angular acceptance. This placement of the calorimeter was the most significant change from the Mark I and Mark II configurations.

The principal compromise made in the design was the choice of a calorimetry technology with good spatial resolution emphasized over good energy resolution. This choice was driven by the recognition that most Mark III data analyses would attempt complete reconstruction of exclusive final states, and would therefore be able to use constrained kinematic fitting procedures. Studies of the performance of these procedures made clear that a poor measurement of the energy of a photon would be almost completely compensated by the kinematic constraints as long as the direction of the photon were well-measured.

Nine years of experience with Mark III data analysis have confirmed the correctness of this choice. Such complex final states as $J/\psi \rightarrow \gamma\omega\omega$, with four charged particles and five photons, and $\psi(3770) \rightarrow D^+D^-$, $D^+ \rightarrow K^-\pi^+\pi^+$, $D^- \rightarrow K^o_S\pi^-\pi^-\pi^+$, with eight charged particles, have been studied successfully and productively. Nevertheless, for inclusive studies, such as of J/ψ radiative decays, where no kinematic constraints are available, the resolution of the electromagnetic calorimeter is quite inadequate for the detection of any narrow structure in the photon energy spectrum, leading to the decision to restrict the analysis presented in this thesis to converted photons observed in the drift chamber.

Figures 4.1 and 4.2 contain, respectively, axial and transverse views of the Mark III apparatus.

The motivation and design criteria for the Mark III spectrometer are discussed in Reference [41]. The spectrometer, as built, is described in Reference [42]; further details on several of the detector subsystems are available in other publications, referenced below.

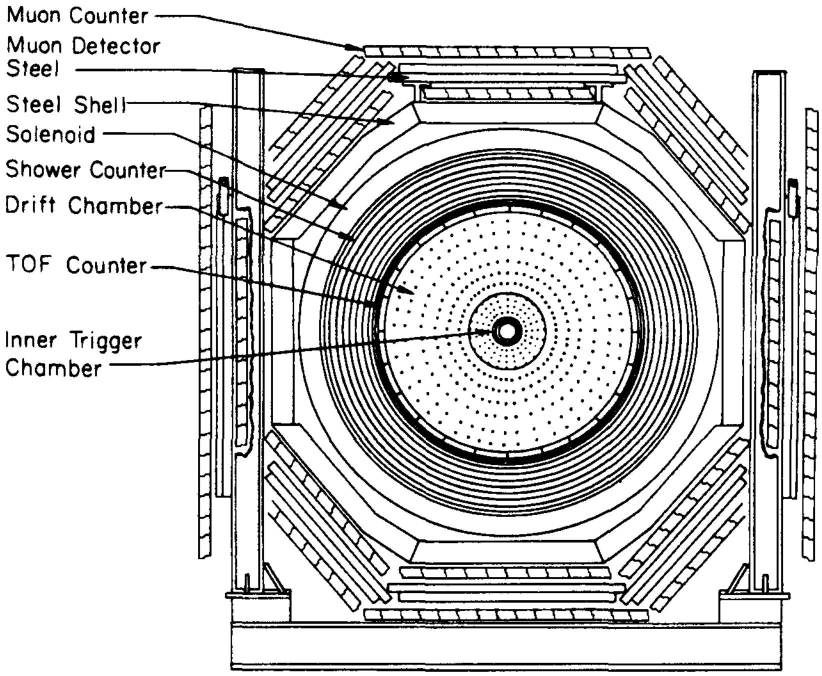

Figure 4.1 Axial view of the Mark III spectrometer.

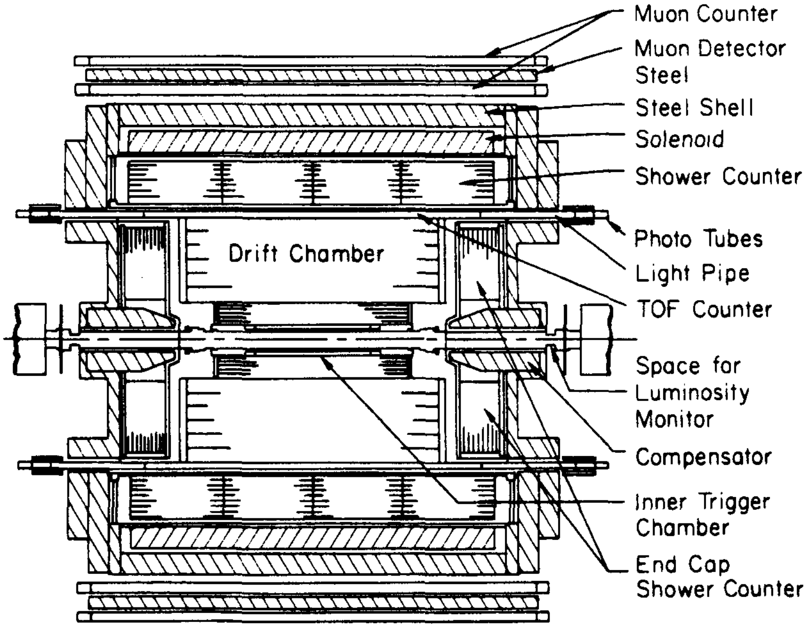

Figure 4.2 Transverse view of the Mark III spectrometer.

The inclusive converted photon analysis presented in this thesis depends almost exclusively on the charged track momentum measurements from the drift chamber system. Accordingly, although the drift chamber and related systems will be discussed in some detail below, the description of the other systems will be abbreviated. Interested readers are referred to the detector system publications and to the many other Mark III doctoral theses.

Section 2 Drift Chamber

The Mark III central drift chamber is composed of two separate physical devices: an inner chamber with four cylindrical wire planes,[1] and a main chamber with thirty cylindrical planes arranged in seven layers, two of which are twisted for stereo readout. The inner chamber and three layers of the main chamber are instrumented for charge division measurement of the longitudinal coordinate, and the innermost layer of the main chamber for dE/dx measurement.

The mean charged particle momenta in charmonium and charmed meson decays are predominantly below 1 GeV/c; therefore, the measurement errors on charged tracks are dominated by the effects of multiple Coulomb scattering. Minimizing this effect requires the minimization of the material traversed by charged particles before and during their passage through the drift chamber. This was a major goal of the Mark III design. The thicknesses of material, in radiation lengths, in the beam pipe and drift chamber are summarized in Table 4.1.

The spatial resolution achieved by the drift chamber varies from layer to layer, as discussed below, resulting in an overall momentum resolution for all tracks of

$$\frac{\sigma_p}{p} \simeq 1.5\% \cdot \sqrt{(1+p^2)}, \text{ for } p \text{ in GeV.}$$

---

[1] This chamber was inoperative in the 1986 running cycle, and was replaced with a high-resolution straw chamber vertex detector[43] in the final, 1988 cycle. The vertex detector will not be further discussed in this writing.

The decay process $J/\psi \rightarrow \mu^+\mu^-$ provides an excellent source of a large number of charged tracks of known momentum, 1.5448 GeV/c^2. Analysis of a sample of these tracks, restricted to the central 65% of the solid angle surrounding the interaction region by the acceptance of the muon identification system, yields the following results for the drift chamber system's performance:

- Overall momentum resolution: σ_p = 0.036-0.038 GeV/c for the 1983 and early 1985 J/ψ data, and σ_p = 0.041-0.043 GeV/c for the later 1985 data. The decrease in resolution in the later data is due to the absence of information from the outermost layer of the chamber. Numerous cells in the layer had developed high voltage discharge problems and the layer was removed from service to protect the rest of the chamber.
- Dip angle (z) resolution: $\sigma_{\tan\lambda} = 0.008$
- Azimuthal angle resolution: $\sigma_\phi = 1.6$ mr
- Transverse vertex position (impact parameter) resolution: $\sigma_\xi = 270$ μm
- Longitudinal (z) vertex position resolution: $\sigma_z = 5.5$ mm

The main drift chamber is described in detail, including construction information, in Reference [44]. No separate publication is available for the inner drift chamber.

Table 4.1 Material thicknesses contributing to multiple scattering errors in the drift chamber

Beam pipe (7.5 cm radius, 1.5 mm thick Be)	0.0040
Inner chamber (Layer 1)	0.0068
Main chamber inner wall	0.0016
Main chamber gas	0.0075
Main chamber wires	0.0015
Total material	0.0214

Inner Drift Chamber (Layer 1)

A large 4π detector is subject to a considerable flux of cosmic rays. In order that the data acquisition system not be overwhelmed by the rate of these events, one of the most important requirements on a triggering system is the ability to distinguish events as having originated from the actual beam collision point, at the known time of beam crossing. The more precisely the trigger is able to enforce these requirements, the more "grazing" and out-of-time cosmic rays that can be rejected. While it is possible to track the charged particles in an event, project their trajectories back to a common primary vertex, and require this vertex to be located in the collision region, this is a complicated procedure, and, given the technology available when the Mark III was designed, one not at all suited for the very fast decisions required of a trigger.

A far simpler technique is the use of a small detector device near the collision point, one whose size alone enforces the spatial origin requirement. This device must also be capable of setting a reasonably narrow window around the beam crossing time. The previous large magnetic detectors at SPEAR had used a set of scintillation counters around the beam pipe for this purpose. This scheme provided the required spatial and temporal resolution, but left a large amount of material in the path of the particles emerging from the collision, worsening the multiple scattering problem and limiting the detection efficiency for low energy photons. The use of scintillators presented the additional problem of extracting the resulting light from the detector's magnetic field in order to allow the use of photomultiplier tubes.

The Mark III design instead uses a very low mass inner drift chamber to implement the beam vertex requirement in the trigger. A chronotron circuit is used in order to enforce the beam crossing time window. This arrangement is described further in the discussion of the trigger in Section 7.

The inner drift chamber consists of four layers of 32 drift cells each, labeled 1a–1d. Adjacent layers are offset in azimuth by ½ cell, a requirement of the chronotron circuit used in the trigger. The chamber is bounded and the layers separated by layers of 2 mm Rohacell foam covered with 0.5 mm of aluminized Mylar, supported on Lucite rings at the ends of the chamber. This produces a very light yet rigid structure (the entire chamber can easily be lifted by a single person). Additional design details are presented in Table 4.2.

Table 4.2 Inner drift chamber specifications

Inner wall radius		9.2 cm
Outer wall radius		13.65 cm
Cell half-width (sense wire to guard wire)	inner layer (a)	0.96 cm
	outer layer (d)	1.29 cm
Cell thickness		1.1 cm
Sense wires		38 μm stainless steel
Field wires		178 μm BeCu
Gas		70% Ar, 30% C_2H_6
Gas flow rate		5 volumes/day

The cells themselves are formed by alternating sense/field wires, held at +2000–2200 V, with guard wires held at –200 V, all centered radially within a layer's cylindrical space. The conductive inner and outer walls of the layer are grounded. The negative guard wire potential is chosen to provide a sharper cutoff of the drift time distribution at the expense of a slight loss of efficiency as ionization produced very close to the guard wire drifts to the cell wall rather than the sense wire. An axial view of the inner drift chamber structure, with a detail of the cell geometry, is shown in Figure 4.3.

The cell configuration produces a highly non-uniform electric field across the cells, leading to difficulties in parametrizing the time-to-distance relation required to obtain

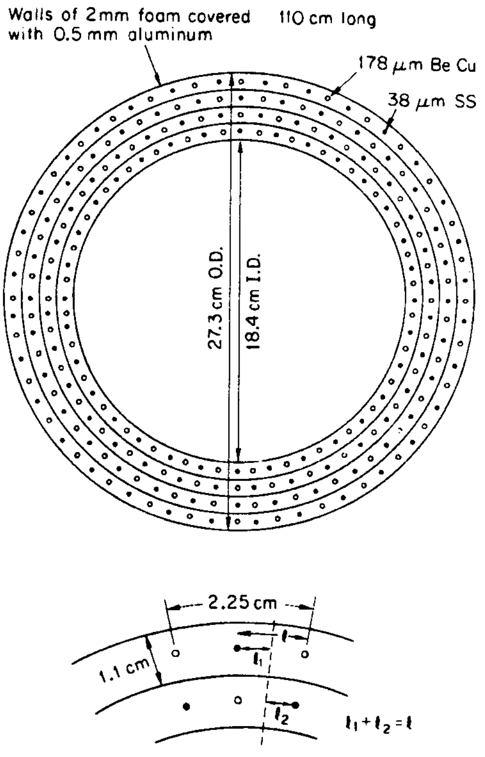

Figure 4.3 Axial view of the inner drift chamber (Layer 1).

spatial coordinates from the raw data. While detailed studies have shown that local spatial resolutions of approximately 250 microns could be achieved, in practice, in the reconstruction of large samples of tracks, the effective resolution obtained is in the range 280–330 microns. The per-layer efficiency for charged particles has varied in the range 90–95%, depending on the guard wire voltages and the presence of noise. Under certain beam conditions, very high hit rates from spurious tracks and synchrotron radiation X-rays can degrade the performance of the inner chamber.

Main Drift Chamber (Layers 2–8)

The main drift chamber is, as outlined above, divided into seven cylindrical layers. The innermost, Layer 2, is composed of twelve cylindrical sense wire planes, while each of the others, Layers 3–8, are composed of three sense wire planes. Each layer has a number of cells equal to sixteen times its layer number. Thus, as Layers 3–8 are centered at radii proportional to their layer numbers, the sizes of the cells remain approximately constant throughout the drift chamber.

The wires in Layers 4 and 6 are twisted, in opposite directions, from axial alignment in order to couple the measurements from these layers with the z position of tracks in the chamber. By combining information from these so-called *stereo layers* with that from the axially oriented layers, it is possible to determine the dip angle of a reconstructed track.

Figures 4.4 and 4.5 display axial and transverse views of the drift chamber.

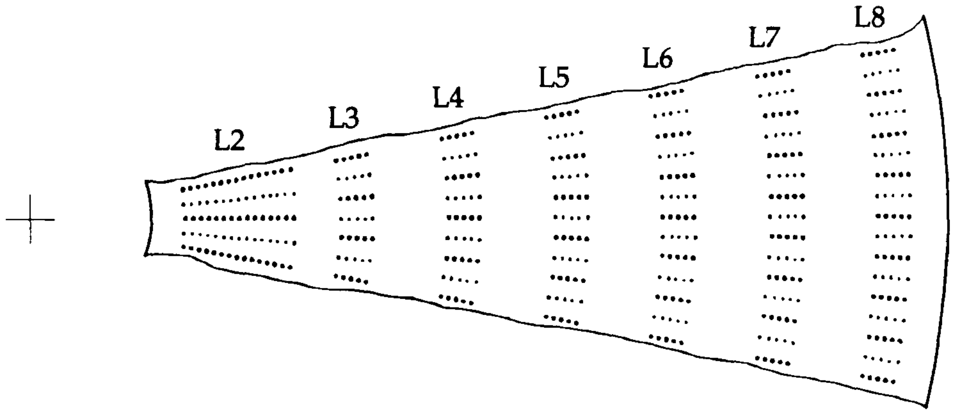

Figure 4.4 Mark III drift chamber: view along the beam axis of one sector: 1/16 of the chamber.

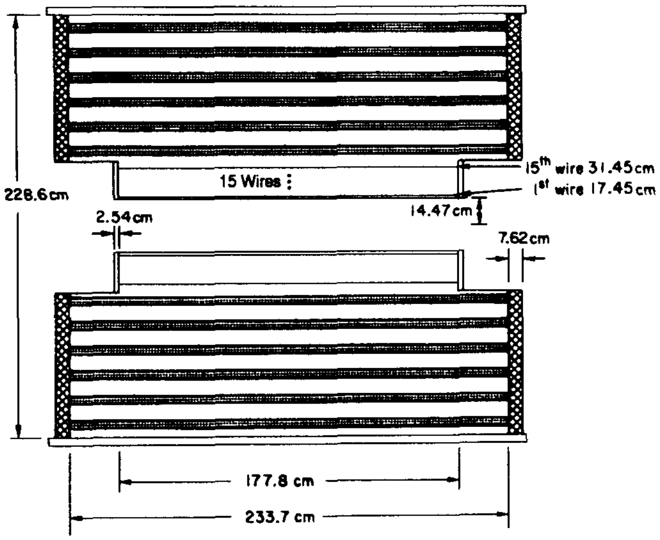

Figure 4.5 Mark III drift chamber: view perpendicular to the beam axis.

The drift chamber gas is an 89% argon, 10% CO_2, 1% methane mixture, a gas which has been found to be resistant to polymerization or the formation of "whiskers" under the high voltage operating conditions. A trace amount of water vapor was added to the gas during the 1985 J/ψ run in order to attempt to suppress a problem of excessive current draw from the high voltage supply, thought to be due to local avalanche formation. Although this remedy has been found to be successful in several experiments, the results were inconclusive in the Mark III chamber.

The cell structure in Layers 3–8 follows a common pattern. The cells are bounded by radial rows of five field wires, held at approximately –4200 V, alternated with radial rows of one guard wire, three sense wires, and one guard wire. The guard wires are of a resistive material, allowing the collection of charge division information; Layers 3, 5, and 7 were instrumented for this purpose. The structure of a single cell is shown in Figure 4.6. The cell width increases slightly with radius in the layer; therefore, the field wire voltages are graded to maintain a radially constant electric field across the cell. The field was chosen to be in the constant-velocity regime of the gas, where the drift velocity is relatively field-independent. The field is also high enough that the gain is saturated, resulting in relatively constant pulse heights from all tracks. Additional details of the design of Layers 3–8 may be found in Table 4.3.

Table 4.3 Specifications for Layers 3–8 of the main drift chamber.

Length	233.7 cm
Outer radius	114.3 cm
Guard and charge division wires (#1 and #5)	57 μm stainless steel
Sense wires	20 μm tungsten
Field wires	175 μm BeCu
Radius of central wire (#3)	N × 13.45 cm
Number of cells	N × 16

Table 4.3 (Continued) Specifications for Layers 3–8 of the main drift chamber.

Stereo angle of Layer 4	7.7°
Stereo angle of Layer 6	-9.0°
Cell half-width, wire #3	2.64 cm (580 ns)
Staggering	±400 μm

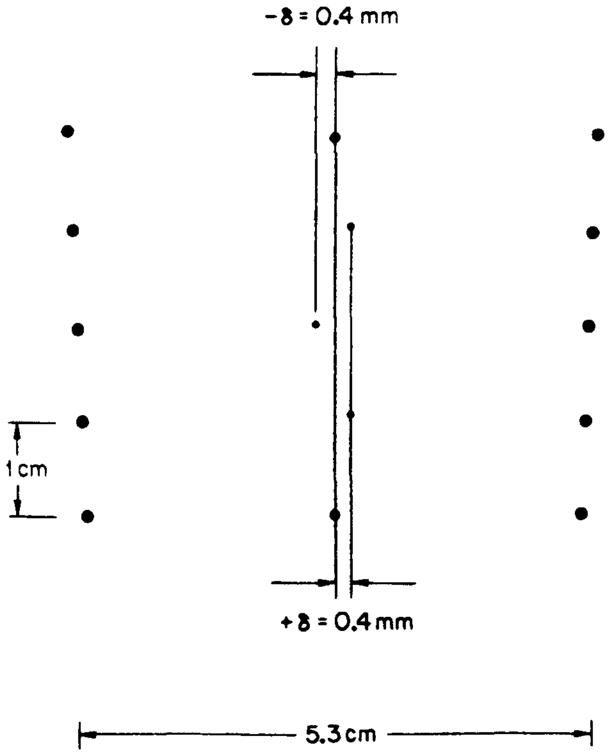

Figure 4.6 Schematic diagram of a single cell in Layers 3–8 of the main drift chamber.

The density of sense wires is considerably higher in Layer 2, which is composed of fifteen cylindrical wire planes. The innermost and outermost wires are guard wires. The central wire, although of the sense wire material, is not instrumented. The twelve active sense wires are divided, for the purposes of the data acquisition system into four sublayers of three wires each, Layers 2a–2d. The high wire density was motivated by the desire to obtain a large number of measurements for decaying tracks, or tracks at large dip angles leaving the ends of the drift chamber. Figure 4.7 displays the configuration of a single Layer 2 cell.

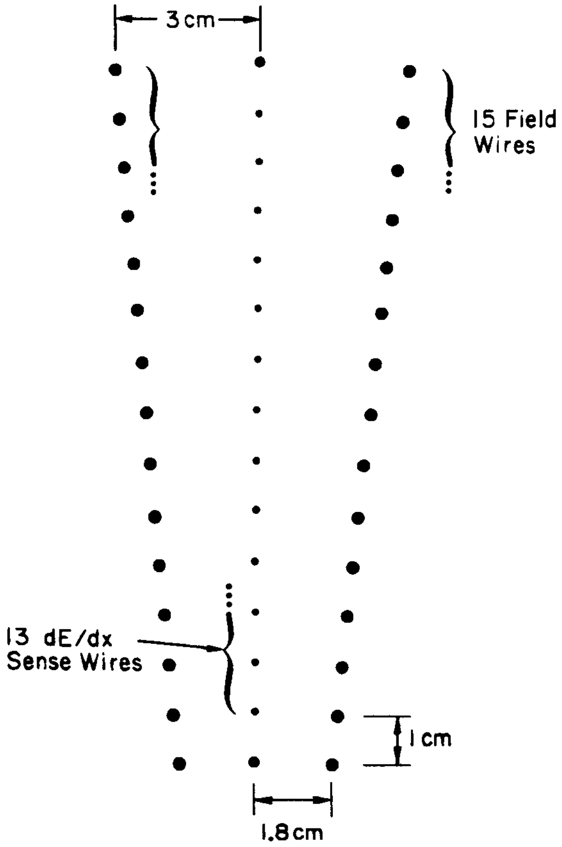

Figure 4.7 Schematic diagram of a single cell in Layer 2 of the main drift chamber.

The electric field in Layer 2 is adjusted to a lower level than in the outer layers, with field wire voltages in the range -3200 to -4200 V. At this field, the gas gain is not saturated; the pulse heights on the wires are proportional to the ionization deposited in the cells. Layer 2, unlike the outer layers, is instrumented for the readout of pulse heights. The resulting information is used to obtain a measurement of the dE/dx energy loss for charged particles. For slow particles in the $dE/dx \propto 1/\beta^2$ region of energy loss, this information can be used for particle identification. The system performance allows useful separation of pions and kaons up to momenta of approximately 0.6 GeV/c.

Additional details of the design of Layer 2 are presented in Table 4.4.

Table 4.4 Specifications for Layer 2 of the main drift chamber.

Length	177.8 cm
Inner radius	14.47 cm
Guard wires (#1 and #15)	57 μm stainless steel
Sense wires	20 μm tungsten
Field wires	175 μm BeCu
Radius of wire #1	17.45 cm
Radius of wire #15	31.45 cm
Number of cells	32
Cell half-width, wire #2	1.81 cm (400 ns)
Cell half-width, wire #14	2.99 cm (660 ns)
Staggering	±150 μm

The measurement of a drift time yields, after appropriate calibration, a measure of the distance between a charged particle track and a sense wire. There is, however, an ambiguity. It is impossible to determine from this measurement whether the track passed by on the $+\phi$ or the $-\phi$ side of the wire in azimuth. This is known as the *left-right ambiguity*. When a charged particle trajectory is ultimately fit through all the measurements along the track, it is possible to select the correct resolutions for this ambiguity by comparing the fit qualities for the different possibilities, at the cost of considerable computation time.

In the Mark III drift chamber, the left-right ambiguity is resolved, for most tracks, at the cell level. The sense wires within a cell are staggered in azimuth. It is then possible to construct a quantity from the measured times whose value reveals the correct left-right assignment. For the three wires in a cell in Layers 3–8, the quantity is

$$\Delta \equiv v_{drift}\left(\frac{t_1 + t_3}{2} - t_2\right),$$

where v_{drift} is the mean drift velocity (50 μm/ns), and t_1, t_2, t_3 are the measured times from the three wires, with t_2 the time from the (staggered) central wire. A typical distribution of this quantity is shown in Figure 4.8. The separation between the peaks reflects the wire stagger, increased somewhat by the deflection of the wires due to electrostatic forces. A value of Δ in one or the other peak corresponds to a track on one or the other side of a cell. The entries in the center of the plot result from tracks passing between the sense wires within the cell. The widths of the peaks reflect the local intrinsic position resolution of the outer layers. Using this plot, that local resolution, for Layers 3–8, can be determined to be approximately 220 microns.

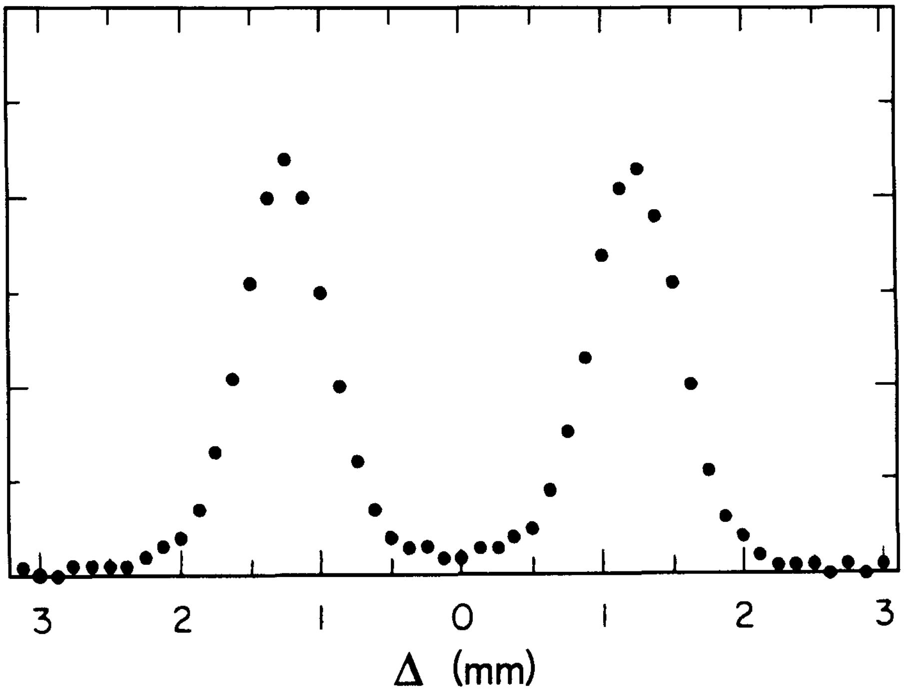

Figure 4.8 Distribution of the left-right ambiguity resolution variable Δ.

The actual position resolution achieved is somewhat worse — approximately 250–260 microns. The discrepancy is largely due to systematic errors introduced in the determination of the wire locations, and the parametrization of the electrostatic deflection of the wires. The position resolution achieved for Layer 2 is considerably worse — 300–370 microns, where the intrinsic resolution is approximately 270 microns. Some of the degradation of resolution in Layer 2 appears to be due to the lower gas gain chosen for dE/dx measurement. Operation in the unsaturated regime produces pulse height variations not present in the outer layers, resulting in a degradation to the time resolution resulting from the systematic time shift with pulse height. This does not appear to account for the entire effect, however, and the cause of the remainder is not well understood.

Section 3 Time-of-Flight System

Given a charged particle momentum measurement from the drift chamber, it is possible to obtain an estimate of the mass of the particle from a measurement of its velocity. This can be obtained by a measurement of the time required for the particle to travel a known distance.

The Mark III time-of-flight (ToF) measurement system consists of a set of forty-eight scintillation counters arranged in a cylindrical shell between the drift chamber and the shower counter. The counters are, therefore, located within the detector solenoid's field, necessitating the use of light guides to allow the positioning of the photomultiplier tubes, one at each end of each counter, outside the field region. The active portion of the system covers the central 80% of the solid angle around the interaction region.

The system provided travel time resolutions for hadronic tracks of approximately 190–210 ps over the life of the apparatus. This is sufficient to provide a 3σ separation of the pion and kaon mass hypotheses up to particle momenta of 0.8 GeV/c, and a 2σ separation up to 1.0 GeV/c.

The design, construction, and early performance of the ToF system are described in detail in Reference [45].

Section 4 Shower Counter

The shower counter, or electromagnetic calorimeter, is of a gas-sampling design. Twenty-four layers of rectangular proportional chamber tubes alternate with twenty-three layers of ½–radiation length of a lead-antimony alloy. The shower counter covers the central and end regions of the apparatus with modules of similar design.

The central 76% of the solid angle around the interaction point is covered by a single monolithic module of cylindrical symmetry. Each proportional chamber layer in the central module is divided azimuthally into 320 axially oriented cells. Each end of the detector is covered with an *end cap,* a set of five modules, where the subdivision was necessary in order to permit the insertion and removal of the modules for access to the ends of the drift chamber and ToF system. The central hole for the passage of the beam pipe is square in cross-section. The cells in the end cap modules are arranged vertically, trimmed so as to fit within the cylindrical space available. There are 94 cells in each layer, counting the cells above and below the beam pipe gap separately. The configuration of an end cap is shown in Figure 4.9. The end caps extend the solid angle coverage of the shower counter system to 94% of 4π sr.

Of the twenty-four layers, in the inner six every cell is instrumented individually; in the remaining layers, the cells are instrumented in radial groups of three. There are therefore twelve independent measurements in depth for each cell: six single layers and six triple layers. The two ends of each cell are read out separately, and the relative pulse heights used to determine the position along the cell at which the ionization was deposited.

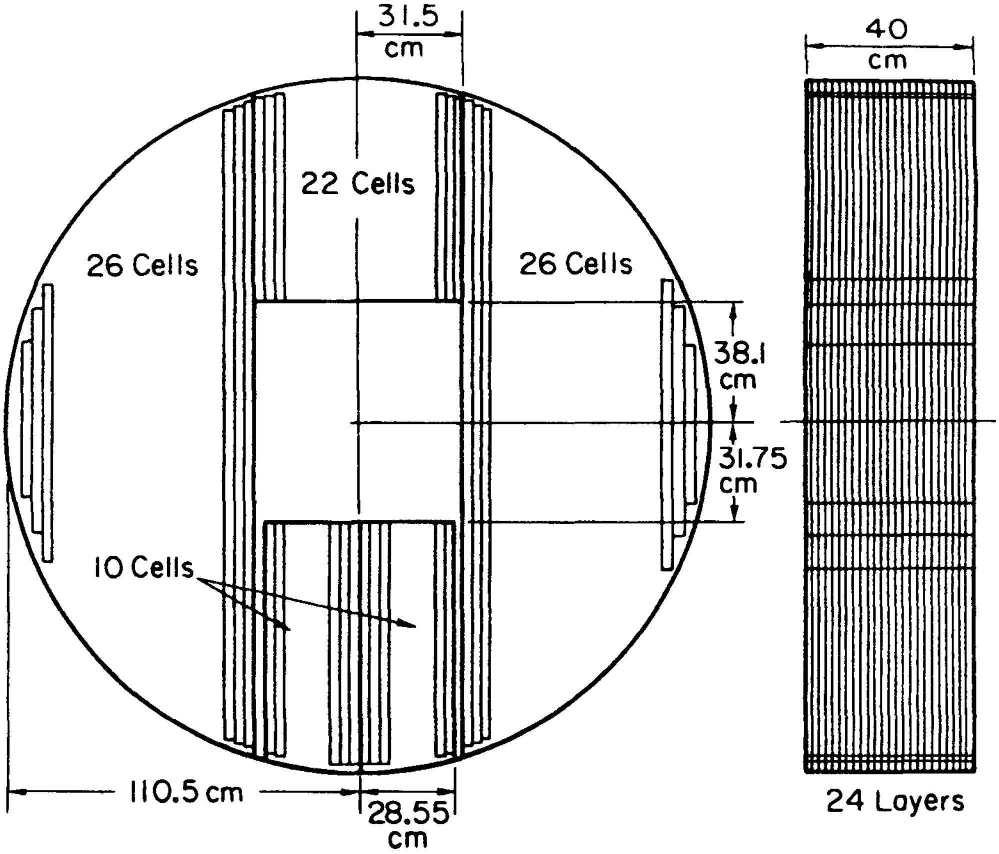

Figure 4.9 Axial and transverse views of a shower counter end cap.

The energy and position resolutions achieved for the central shower counter are:

$$\frac{\sigma_E}{E} = \frac{17.5\%}{\sqrt{E/(1\mathrm{GeV})}}$$

$$\sigma_\phi = 7 \text{ mr},\ \sigma_z = 0.8\% \times (wire\ \ length),$$

and for the end caps:

$$\frac{\sigma_E}{E} = \frac{17\%}{\sqrt{E/(1\mathrm{GeV})}}$$

$$\sigma_x = 7 \text{ mr},\ \sigma_y = 1.0\% \times (wire\ \ length).$$

The shower counter was located inside the solenoid coil in order to minimize the amount of material preceding it, and maximize the detection efficiency for low energy photons. This goal was well met, as can be seen from the plot of detection efficiency as a function of energy displayed in Figure 4.10. The efficiency is essentially flat down to energies of 0.1 GeV. The useful detection efficiency for physics analyses extends below 0.075 GeV.

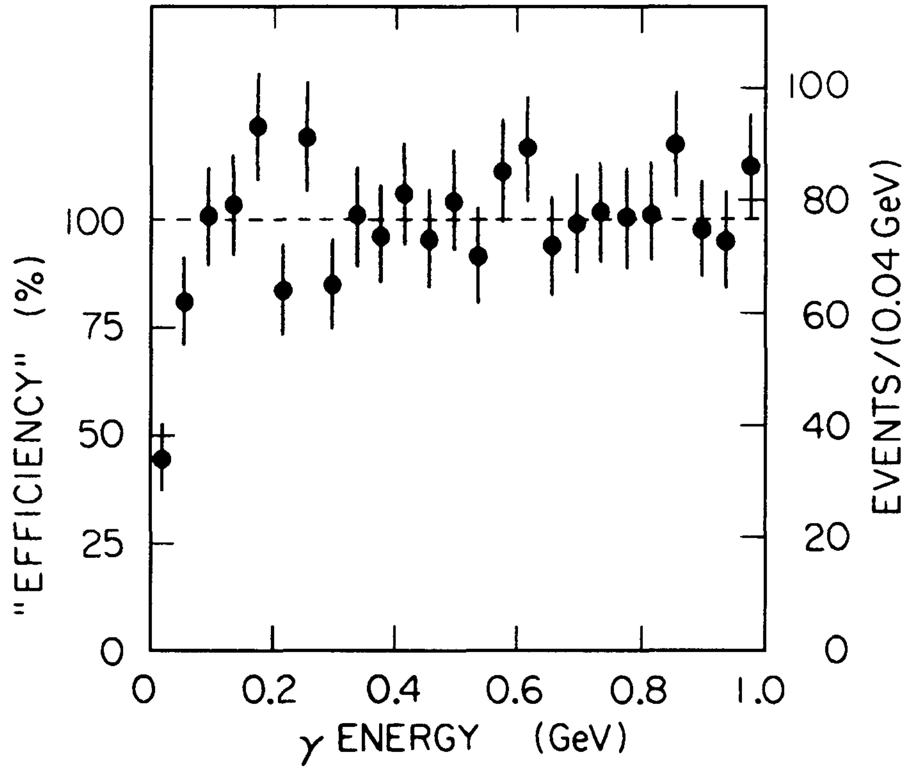

Figure 4.10 Detection efficiency for photons in a fiducial region of the shower counter system, as a function of energy.

The central, or "barrel" shower counter is described in detail in Reference [46], and the end cap shower counters in Reference [47].

Section 5 Solenoid

The Mark I magnet flux return steel was retained and used in the construction of the Mark III experiment. However, since the solenoid was now to be outside the shower counter, its thickness was no longer a major design constraint, and could be increased in order to lower its power consumption. A new conventional coil was therefore wound to generate the design field of 0.4 T at the center of the detector.

An axial magnetic field, when imposed on a beam in a storage ring, has the undesirable effect of coupling the horizontal and vertical motions of the beam. In the initial Mark III configuration, this effect was compensated by the introduction of small solenoids around the beam line at each end of the detector which were arranged to cancel the total axial field integral through the detector on the beam axis. Following the "mini-β" modifications[35] to SPEAR in 1984, it was no longer possible to insert compensating solenoids of sufficient strength in the space available. The field was partially compensated by the so-called "bucking coils" which were used to shield the final quadrupoles from the detector field and prevent the saturation of their iron, but full compensation could only be achieved through the use of rotated quadrupoles to provide a cancellation of the vertical-horizontal coupling.

Since the detector solenoid, with diameter comparable to its length, is not an ideal solenoid, its field can not be expected to be uniform. An accurate knowledge of the field is essential to the correct reconstruction of the trajectories of charged particles in the drift chamber. The field was measured, before the detector components were inserted in the solenoid, with a configuration of Hall probes that could be moved throughout the field volume. An analytic model has been developed, using 17 parameters, which reproduces the axial and radial field components to an accuracy of 0.2% across the space occupied by the drift chamber.[48]

Section 6 Muon Detector

In order to provide a muon identification capability, the central region of the detector, outside the shower counter, coil, and 20 cm of flux return steel, is surrounded by two layers of proportional tubes, separated by an additional 13 cm of steel. The tubes are axially aligned with the detector and arranged in an octagon of planar arrays in each layer. The tubes are staggered so as to ensure at least a single hit for any track passing through an array. The arrays are composed of a series of modules, each containing eight tubes. The tubes are read out at one end of the module; non-adjacent pairs of tubes are connected in series at the opposite end. It is therefore possible to determine the longitudinal position of a hit by charge division within each such pair of tubes. The non-adjacency reduces the likelihood that both tubes within a pair will be hit in the same event. The system covers approximately 65% of the solid angle surrounding the interaction point.

The muon detection system is highly efficient ($\gtrsim 95\%$) for muons of momentum above 0.7 GeV/c. Below this momentum, the detection efficiency drops rapidly due to the range-out of muons in the flux return steel, falling to zero below 0.6 GeV/c. High momentum hadrons can penetrate the steel, leading to a mis-identification as a muon. Pions in the momentum range 1.0–1.5 GeV/c have approximately a 14% probability of reaching the inner muon detection layer, with 4.5% reaching the outer layer.

There is no separate publication describing the Mark III muon system, but additional details are available in Reference [49], a Mark III doctoral thesis.

Section 7 Trigger

Electron-positron bunch crossings occur in each SPEAR interaction region at 1.28 MHz, or once every 781 ns. While the rate of true s-channel e^+e^- interactions is quite small, in the 0.1–1 Hz range depending on beam energy, the spectrometer must be ready to acquire such events at as large a fraction of bunch crossings as possible.

(This fraction is often known as the livetime ratio.) A livetime ratio of less than its ideal value of one is equivalent to a proportional drop in the luminosity of SPEAR. Livetime ratios of less than 90% therefore have generally been considered unacceptable.

The full readout of a Mark III event takes approximately 30 ms, during which time the spectrometer is unable to acquire further events. In order to maximize the livetime ratio, the number of events fully acquired must be kept as low as possible. The actual design requirement is still more stringent, however. In order to meet the goal of a 90% livetime ratio, it must be possible to recognize at least that fraction of all bunch crossings as uninteresting, and reset the data acquisition electronics in preparation for the next crossing, within a single 781 ns interval.

In order to meet both goals, rapid rejection of most beam crossings, and a small final number of fully acquired events, the Mark III trigger is organized in a series of levels, each using more information from the spectrometer and taking more time for its decision than the one before. The first level (known as Level 0), uses simple information from the time-of-flight system and from the inner layers of the drift chamber to generate a decision within 580 ns of the beam crossing, allowing sufficient time for the reset for the next event. The next level, Level 1, uses one or two[2] additional beam crossings to make a more careful decision, primarily using a digital processor to recognize tracks in an x-y view of the drift chamber. During all of the major physics runs of the Mark III experiment, the Level 1 trigger was entirely adequate to reduce the data stream to the few per second rate acceptable for final acquisition. Nevertheless, a final Level 2 trigger was available should the capabilities of Level 1 have been exceeded. Level 2 uses information from the charge division wires in the drift chamber to ensure that the transverse projection

---

[2] A second additional beam crossing was required only when the so-called *two-track non-adjacency* requirement was included in the trigger decision. This requirement that there be at least two charged tracks separated by at least one-sixteenth of 2π radians in azimuth was not used in normal J/ψ running.

of acquired events is consistent with interactions occurring at the nominal beam crossing point at the center of the spectrometer.

The trigger has the capability to use shower counter information in both Level 0 and Level 1, making it possible to recognize events containing no charged tracks. However, the external logic required to pre-process the shower counter signals in order to implement such a *neutral trigger* was not available during the Mark III J/ψ data runs. A prototype of such a system was added for the 1986 D_s run; however, its sole application was the detection of Bhabha scattering events where the outgoing electron and positron emerged at a sufficiently small angle to the beam that the charged tracks could not be recognized by the trigger.

Additional information on the design of the trigger may be found in Reference [50].

Trigger Conditions

Level 0 Information Only two pieces of information were available to Level 0 during the J/ψ running: the "chronotron OR" and "Cruz Box" signals.

Chronotron OR The chronotron OR signal is defined as the logical OR of the outputs of the chronotron circuits associated with each cell in Layer 1. Referring to Figure 4.3, because of the ½ cell offset between sublayers in Layer 1, for radial tracks the quantity $\ell_1 + \ell_2$ should equal ℓ, the full width of a cell. In practice, this is not precisely the case. The cell width varies between sublayers in Layer 1, and all tracks are not radial. The latter approximation is, however, very good at the small radius of Layer 1. Sixty-four chronotron circuits, one for each half-cell overlap region, were used to process the information from Layers 1a and 1b. The chronotron, a bidirectional tapped delay line,[51] is used to enforce the $\ell_1 + \ell_2 = \ell$ condition. The OR of all the chronotron signals is then required to fall within a narrow time window in order to reject out-of-time tracks, presumably cosmic rays. The advantage of the chronotron approach is that it permits a

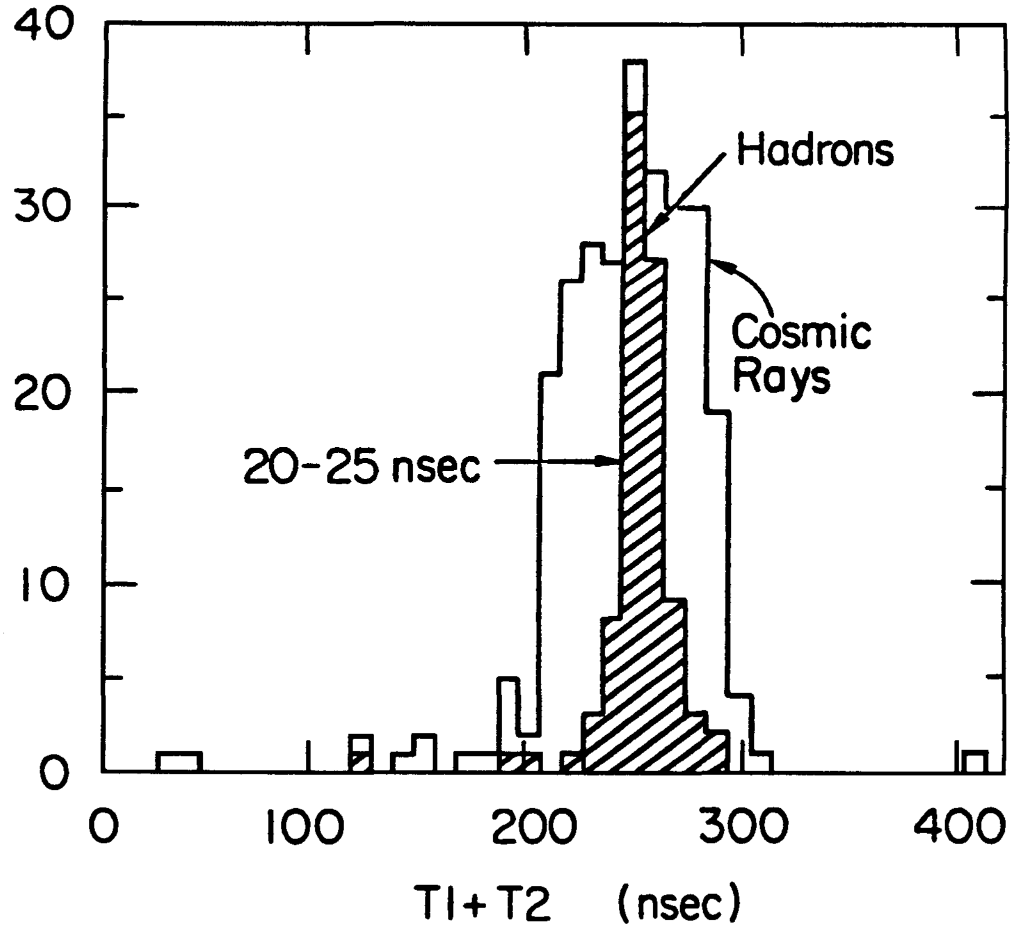

Figure 4.11 Distribution of the quantity $t_1 + t_2$ for hadronic and cosmic ray events. The event identification is from offline analysis.

much narrower window to be set than would be possible for the unprocessed Layer 1 signals. The maximum drift time in Layer 1a and 1b is approximately 250 ns. Requiring only that a hit fall within the 250 ns interval, out of the total crossing interval of 781 ns, following a beam crossing would still retain over 30% of hits due to cosmic rays. The window set on the chronotron OR for J/ψ running was set to 100 ns. As can be seen in Figure 4.11, which displays the time distribution of the chronotron signal for hadronic events and for cosmic rays, this was a rather loose requirement for the desired events; however, it rejected 87% of cosmic ray tracks.

The chronotron OR rate during normal J/ψ running was in the range 500–5000 Hz, with the higher value approaching levels that led to unacceptable dead time. This rate was completely dominated by beam-related backgrounds. Despite the fact that only a small fraction of this rate stemmed from cosmic ray events, it is important to note that the higher-level trigger stages have little ability to distinguish cosmic rays from desirable tracks, so the rejection power of the chronotron is still essential. The ultimate rate of cosmic ray events acquired was approximately 1 Hz, 25–30% of the total, under the J/ψ trigger conditions. A large increase in the cosmic ray rate would have had a significant impact on the livetime ratio.

Cruz Box The Cruz Box[3] signal is obtained from a similar chronotron system applied to the time-of-flight counters. The signals from the final dynodes[4] of the ToF photomultiplier tubes at each end of a counter are run into a chronotron circuit which, in this case, enforces the requirement that the sum of the measured times corresponds to the known length of the counter.

A complex, programmable device[52] is then used to combine the chronotron outputs from the 48 counters into a single signal to the trigger. This device permits the selection of particular groups of counters as well as windows of position along the counters. For normal running, however, it was configured so that its output was a simple OR of all its inputs, with the entire length of the counters enabled.

The Cruz Box signal rate during normal J/ψ running was of the order of several hundred Hz.

---

[3] The name derives from its construction at the University of Santa Cruz, one of the member institutions of the Mark III collaboration.

[4] These signals were used in order to avoid tapping, and thereby possibly degrading, the anode signals from the photomultipliers. Extreme care was taken with the anode signals in order to obtain the sub-nanosecond resolution of the ToF system.

Level 1 Information The primary function of the Level 1 trigger logic is to identify charged tracks in the drift chamber data. Tracks are constructed from information from Layers 1b, 3, and 5 of the drift chamber. The patterns of hit cells in these layers for valid tracks were calculated in a simulation and stored in programmable array logic (PAL) circuits. Using these circuits, the trigger is able to perform a very fast identification of tracks in the hits received from the drift chamber. The inputs to this process are cell hits, constructed from the individual wires in order to allow for the presence of dead wires. Hit cells in Layers 3 and 5 are defined as cells with two of the three wires having been hit. Layer 1b hit cells are defined as coincidences between Layer 1b and Layers 2a and 2b; however, the Layer 2 requirement was removed from this coincidence throughout the J/ψ running due to inefficiency. Cells which prove to be inefficient can be overridden in the track-finding, so that trigger processing will continue under the assumption that the cell is always hit. This was necessary for one or two cells in Layer 1 throughout much of the J/ψ running.

The stored patterns correspond to tracks of momentum greater than 0.050 GeV/c. The PAL circuits are designed with a provision to exclude low momentum track patterns in steps up to 0.200 GeV/c, should it necessary to tighten the trigger conditions. This capability was unused in the J/ψ running.

J/ψ Triggers The trigger design allows for up to six independent sets of conditions for the acceptance of an event to be defined and concurrently evaluated. For the bulk of J/ψ running, only two such triggers were defined:[5] the "two-track" trigger and the "one-track-ToF" trigger.

The two-track trigger required, in Level 0, only the chonotron OR signal to be asserted. In Level 1, it required two identified tracks. This trigger was therefore sensitive

---

[5] The extra trigger "slots" were often used to define redundant copies of the standard triggers in order to provide a check for failures in the trigger processor.

to any event with two charged tracks reaching at least Layer 5 before exiting the ends of the drift chamber. The Layer 5 requirement limits the solid angle acceptance of this trigger to the central 88% of 4π sr.

The one-track-ToF trigger required, in Level 0, both the chronotron OR and the Cruz Box signals to be asserted. However, in Level 1, only a single identified track was required. This trigger was sensitive to any event with at least one track reaching the time-of-flight system. The solid angle acceptance for this single track was therefore 76%. A simple one-track trigger without the ToF requirement would have accepted a very large amount of beam-related background, leading to unacceptable dead time.

The Level 0 event rate, with these two triggers enabled, was simply equal to the chronotron OR rate, given the definition of the two-track trigger. The final event rate at Level 1 was 3–5 Hz for J/ψ running, with a livetime ratio of 85–92% during normal conditions. Unusually poor quality of the stored beams could increase the chronotron OR rate to tens of kilohertz or higher, leading to a livetime ratio of 50% or less. Under such poor conditions, the particle flow into the detector generally leads to large amounts of current being drawn from the various systems' high voltage power supplies, something which can cause damage, particularly to the drift chamber. Therefore, even apart from the undesirability of running with poor livetime, no attempt was made to take data under such conditions.

Timing

The detailed operation of the trigger, as well as the rest of the data acquisition electronics, depends on a very precise sequencing of events, starting with the beam crossing and continuing through all the stages of the trigger, data acquisition if desired, and reset of the electronics for the next crossing.

A very sharp and temporally stable signal of the moment of beam crossing is provided by a *beam pick-off*, an electrode inserted into the SPEAR vacuum chamber, on which a signal is induced when an electron or positron bunch passes.

A series of delays must be laid out, starting from this signal, to set off each of the actions in the triggering and data acquisition sequence. The sequencing times must be reliable to better than 2 ns, approximately, in order not to introduce a significant contribution to the time resolution of the drift chamber electronics.[6] Generating these delayed sequencing signals with a system of delay lines would require an enormous amount of equipment, would be inflexible, and would result in progressively poorer quality signals at later times.

Instead, a programmable, digital system was chosen, based on a specially designed CAMAC module known as a *time mark generator* (TMG).[7] The TMG generates eight independent precise timing signals by counting off separately adjustable numbers of cycles of a fast clock signal starting from a common synchronization pulse. As used in Mark III, the synchronization pulse is the SPEAR beam crossing, at 1.28 MHz, and the clock signal is at 89.6 MHz, precisely 70 times the beam crossing frequency. The TMG's logic thus allows selection, under computer control, of delays from the beam crossing time at intervals of the clock period of 11 ns, ranging from zero to 69 clock periods, or 0–770 ns. (Note that each of the eight outputs of the TMG generates a signal at the frequency of the synchronization pulse. All that is adjustable is the relative timing of the signals; there is no gating.)

Timing Signal Sources When the TMG system was initially installed, the required

---

[6] The timing for the time-of-flight system must be stable to better than 100 ps in order not to degrade the overall ToF resolution of ~180 ps. It is generated by a separate special-purpose system, using the signal from an additional beam pick-off.

[7] The TMG was actually a replacement for an early, nonprogrammable system using one-shot circuits which was found to be insufficiently reliable.

clock and synchronization signals were obtained from the storage ring's RF control system. The basic SPEAR klystron RF frequency is 358 MHz, exactly 280 times the ring's circulation frequency. The RF control system's frequency division logic, which maintains the phase lock between the circulation ("$\times 1$") and klystron ("$\times 280$") signals, generates several auxiliary signals, among them a "$\times 70$". This 89.6 MHz signal, which is also precisely locked to the "$\times 1$", was used as the TMG clock signal. The "$\times 1$" signal itself provided the synchronization pulse.

This scheme satisfied the requirements of the TMG, but it suffered from one significant flaw. The single stored bunch in each beam in SPEAR may travel in any of the 280 *buckets* defined by the RF timing structure. While the electron and positron bunches must be in the same bucket in order to collide at the interaction points, the moment of collision may be shifted by any number of 2.789 ns intervals from the time of the RF control system's "$\times 1$" signal.

The actual bucket into which beam is stored is controlled at injection time by the SPEAR operators; it cannot be changed without losing the stored beam. Experience has shown that, for reasons which are not well understood, the choice of buckets is not arbitrary; certain buckets appear to store beam more readily than others. For this reason, the operators often selected a preferred bucket which would remain the same for days or weeks. However, occasionally this preference would change; sometimes only for a single injection, sometimes to a new stable preference. When such a *bucket shift* would occur, the timing of the beam crossing would shift with respect to the TMG-derived timing of the trigger and the (non-ToF) data acquisition electronics. Most such shifts were small: no more than one or two buckets. The triggering and data acquisition timing windows were wide enough that these shifts generally caused no loss of data; however, they did require correction in the analysis of drift chamber data.

Bucket shifts were determined by hand, by inspecting the Mark III operators' records of the readings of a TDC set up to measure the time between the "×1" signal and the actual moment of beam crossing as obtained from a beam pick-off. The resulting timing corrections were then entered, by hand, into a database read by the drift chamber reconstruction package. This procedure was error-prone and occasionally failed to detect bucket shifts which lasted for only one or two data runs.

It was clear that a timing system based on the measured beam crossing time would be more reliable. The difficulty was that, although the beam pick-off signal would have provided the necessary synchronization signal for the TMG, no phase-locked clock signal with a period of $\sim$10 ns was available. This problem was finally solved for the Spring 1985 data-taking cycle.

The solution was a straightforward application of the concept of the phase-locked loop, made somewhat challenging by the requirement of nanosecond-level timing stability. The resulting device, the Beam Phase-Locked Oscillator (BPLO),[8] took the beam crossing signal as input and produced a phase-locked "×70" signal, as well as a buffered version of its input. Although any integral multiple of the beam crossing frequency could have been chosen, it was decided to continue using the factor of 70 to minimize the impact of the installation of the BPLO on the rest of the timing system.

The BPLO was installed at the beginning of the Spring 1985 J/ψ data taking cycle. The required beam crossing signal was derived from a beam pick-off, processed by a specially designed module[9] that converted the variable size, bipolar pick-off signal to a standard NIM pulse. The "×1" and "×70" signals from the SPEAR RF timing system were simply replaced with those from the BPLO, and with a single adjustment

---

[8] Beam Phase-Locked Oscillator, SLAC Module 445–135.

[9] One-Flavor Beam Trigger, SLAC Module 445–134.

to compensate for the different times of the SPEAR RF and BPLO signals, the Mark III timing system was returned to normal operation.

The new timing system performed well, and was retained in continuous operation for the remainder of the life of the experiment. The BPLO device produced an auxiliary signal permitting observation of its phase-locked status. The Mark III data acquisition system was modified to monitor this signal. No phase locking failures were observed by this system at any time during conditions of stable colliding beams.

Section 8 Data Acquisition

The data acquisition system is faced with the task of, given an event acceptance decision from the trigger, digitizing and logging the information in each of the detector systems as rapidly as possible, in order to minimize the associated dead time. Simplifying slightly, the sequence of events involved, in the Mark III design, is the following, beginning with the apparatus in a live (*i.e.*, ready to acquire an event) state, and following it through the acquisition of an event accepted by the trigger (T_0 is the beam crossing time, and ΔT is the crossing interval, 781 ns):

1. ($T_0 - \Delta T + 580$ ns) All sample-and-hold circuitry reset.
2. ($T_0 + 0$ ns) Beam crossing. “Interesting” event, *e.g.*, J/ψ hadronic decay, occurs.
3. ($T_0 + 580$ ns) Resets suppressed due to trigger acceptance of event based on Level 0 information. Resets will continue to be suppressed until the event data acquisition is complete.
4. ($T_0 \rightarrow T_0 + {\sim}1000$ ns) Times, voltages, and charges collected by TAC and sample-and-hold circuitry.
5. ($T_0 + \Delta T + 580$ ns) Final trigger event acceptance decision. Resets again suppressed. Trigger issues two signals: “begin digitization,” to the Brilliant ADCs (to be described below), and an “acquire this event” interrupt to the data acquisition computer, a

Digital VAX-11/780. If an enabled trigger requires the two-track-nonadjacency condition, an extra beam crossing is required for this decision.

6a. Digitization proceeds in parallel in each of the BADCs in the detector subsystems. Each BADC cycles through the set of sample-and-hold circuits assigned to it, digitizing the signal and applying a threshold and a quadratic calibration. Concurrently...

6b. ... the VAX processes the "event" interrupt, and begins collecting data from the CAMAC system, starting with the trigger. Once it has read the trigger information for the event, which has been available since the moment the event was accepted, it begins a process of polling the BADCs in sequence, waiting for them to complete the digitization and correction cycle initiated by the "start" signal from the trigger, and then collecting their data.

7. (T_0 + 30 ms) All of the BADCs have completed the digitization cycle, and their data has been read in by the VAX. The VAX issues an "event reset" signal to the trigger and then releases control of the CAMAC system.

8a. The trigger issues reset signals to the sample-and-hold circuits for six consecutive beam crossings, in order to allow the system to stabilize. It is then ready to acquire an event, and the entire process can begin again. Concurrently...

8b. ... the VAX adds some structural formatting to the acquired data, and logs the event to tape.

In addition to the processing of the event stream, the data acquisition system provides facilities for beginning and ending the collection of data, controlling the trigger conditions, analyzing a subsample of the data as it is collected, and monitoring the quality of the data and the performance of the apparatus.

The Brilliant ADC

All of the event data produced by the detector subsystems is originally in analog form and must be digitized in order to be recorded. It would be prohibitively expensive to have a dedicated analog-to-digital converter (ADC) attached to every one of the ~10,000 channels in the apparatus. For this reason, a multiplexing approach was adopted. The analog signals are collected by sample-and-hold circuits, or, in the case of the drift chamber and ToF timing signals, combined time-to-amplitude and sample-and-hold circuits. The circuits are packaged into CAMAC modules, with additional logic which permits the selection of a single channel within a module to have its stored signal routed to an output connector. Each single crate (or, in some cases, a pair of crates combined into a single logical crate) is assigned a device known as a Brilliant ADC, or BADC.

The BADC, a SLAC-designed CAMAC module, contains an ADC circuit and a custom microprocessor with a program stored in read-only memory (ROM). The BADC is capable of taking control of the CAMAC crate in which it resides and interrogating the other modules in the crate. It has a single analog input connector.

The analog outputs of all the sample-and-hold modules in a crate are wired together and connected to the BADC's analog input. In normal data acquisition, when the BADC has received a "start" instruction, under the control of its stored program it commands each module in the crate, in sequence, to connect each of its stored signals to its analog output. The BADC then digitizes the signal.

The program also permits performing zero-suppression and calibration correction on the digitized data acquired. A threshold may be defined for each of the up to ~2000 channels controlled by the BADC. When a digitized signal value does not exceed the threshold, it is discarded. A set of quadratic calibration constants may also be defined for each channel. The configuration of channels to be digitized, and the thresholds and calibration constants, are downloaded to the BADC by the VAX at the start of each data-taking run.

When the digitization and correction cycle is completed, the BADC produces a signal indicating that its data is ready and that it may be interrogated by the data acquisition computer. In the Mark III system, these signals are collected by specially designed CAMAC modules in a manner that allows the VAX to perform other tasks while waiting for the completion of the BADC cycles.

When the BADC receives a request for the stored data, it proceeds to transmit a series of pairs of sixteen-bit words, each consisting of a channel address and the digitized value associated with that channel. Channels with no signal above threshold are suppressed, saving time and limiting the event size.

The BADCs have additional features which, among other purposes, are used in the online calibration process that determines the constants to be downloaded, but these are beyond the scope of this discussion.

PART III
Inclusive Photon Data Analysis

Chapter 5 Detection of Converted Photons

Section 1 Overview

The goal of this work is the measurement of properties of the direct photons emitted in radiative J/ψ decays. The electromagnetic calorimeter of the Mark III experiment is, as described above, of a gas-sampling design, and does not deliver high-resolution measurements of the energies of detected photons. In order to overcome this problem, in this analysis we have chosen to detect photons through the observation in the drift chamber of the electron-positron pairs resulting from conversions of photons in the inner material of the apparatus. This procedure provides a photon energy resolution based on the momentum resolution of the drift chamber, which is considerably better than the energy resolution of the electromagnetic calorimeter.

Conversion Probability

The design of the Mark III detector emphasized, among other goals, the high-efficiency reconstruction of complete exclusive final states, including low-energy photons. To this end, the apparatus was designed with as little material as possible between the interaction region and the calorimeter. Accordingly, the probability for pair conversions of photons before the calorimeter is very low. For high energy photons and thin absorbers, the probability for pair conversion approaches $\frac{7}{9}l$, where l is the material thickness in radiation lengths. The amount of material traversed perpendicularly by a photon going from the beam pipe to the outside of the drift chamber, inclusive, is 0.0214 radiation lengths (X_0), as summarized in Table 4.1. However, since the electron and positron must be detected and well-measured in the drift chamber, the effective material thickness available to this analysis is somewhat less.

The original track recognition algorithm used in the analysis of Mark III data required a track to have at least one hit in the Layer 1 trigger chamber. This reduced the available material for production of detectable photon conversions to the beam pipe and four of the five walls making up the Layer 1 structure, for an effective converter thickness of 0.0094 X_0.

In order to increase the detection efficiency for converted photons in this analysis, the "missing layer" criteria were loosened to allow the reconstruction of tracks with no hits in Layer 1. Under these criteria, the entire Layer 1 structure, as well as the aluminum hexcell inner wall of the main drift chamber, become available to this analysis. Tracks with no Layer 1 hits are required to have at least two hits in the inner three wire cylinders of Layer 2. (Futher details of the "missing layer" criteria are presented in Appendix A.) Using the loosened criteria, the available effective converter thickness is 0.0124 X_0, corresponding to a conversion probability for high energy photons traveling perpendicularly to the beamline of 0.96%.

Since the inner detector structure is cylindrical, the amount of material traversed by a photon leaving the interaction region increases with increasing angles away from the perpendicular. Futhermore, the probability of conversion has a modest energy dependence over the energy region of interest in J/ψ decays. These effects are taken into account in the Monte Carlo simulation of the detection efficiency.

Section 2 Conversion Vertex-Finding

The distinctive property of electron-positron pairs originating from a photon conversion is their small opening angle with respect to the angular resolution of the drift chamber. The characteristic opening angle for the conversion of a photon of energy E_γ is $\theta_{open} \sim m_e/E_\gamma$. This angle is of the order of 1 mr or less for photons of the energies with which this analysis is concerned.

The identification of these pairs in this analysis depends exclusively on the charged particle track information from the drift chamber. The principal criterion in this identification is the small opening angle, supplemented by the requirement that the pair's trajectory appear to intersect the known location of the beam collision point. The location of the conversion vertex is required to fall within the radial region of the apparatus from the beam pipe to the inner wall of the main drift chamber. This suppresses background from π^0 Dalitz decays and other internal conversion processes which produce e^+e^- pairs at the collision point with a small opening angle.

Figure 5.1 displays an idealized view, in the plane perpendicular to the detector's magnetic field (the *bend plane*), of the conversion in the beam pipe of a photon with 0.3 GeV/c transverse momentum. The photon is assumed to convert into an electron and a positron with 0.2 GeV/c and 0.1 GeV/c transverse momentum, respectively. In order to allow a more detailed consideration of the geometry of the conversion vertex, a region including the interaction point and the conversion point is displayed in an expanded view in Figure 5.2. In this figure the curvature of the tracks has been exaggerated for the sake of clarity.

The trajectories determined for charged particles by the track reconstruction program are computed without the use of a vertex constraint: it is not assumed that the track originates from the beam interaction point. However, in order to obtain a momentum vector for a charged particle, the momentum must be evaluated at a specific point on the track. In the standard track data returned to the user by the reconstruction program, the momenta are evaluated at the point of closest approach, in the bend plane, to the origin of the coordinate system.[1] This choice of evaluation point leads to a biased reconstruction of the momenta of particles produced far from the coordinate origin, such as the electrons

---

[1] The coordinate origin is used in preference to the beam interaction point (I.P.) because the position of the I.P. is normally not known until the reconstructed data have been analyzed. The position of the I.P. can be as much as 5mm away from the coordinate origin, and its position varies slowly with time due to adjustments to the storage ring optics.

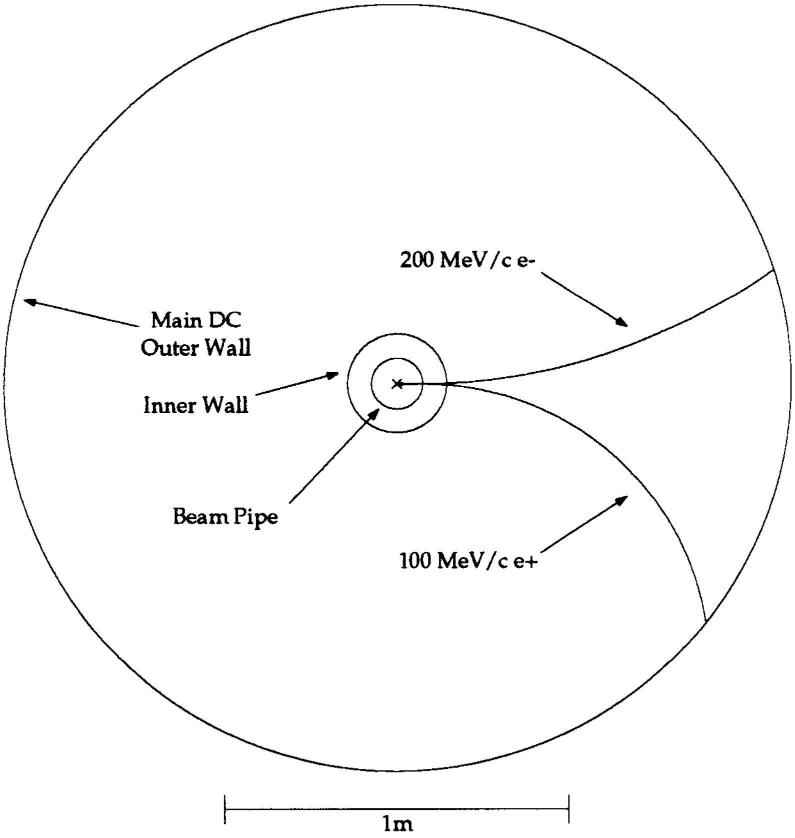

Figure 5.1 Axial view of the conversion in the beam pipe of a photon with 0.3 GeV/c transverse momentum, producing an electron and positron of 0.2 GeV/c and 0.1 GeV/c transverse momentum, respectively. The beam crossing point is marked with an "×" at the center of the beam pipe. The photon is assumed to have been produced at this point. The direction of the detector's magnetic field is out of the plane of the diagram.

resulting from photon conversions. Nevertheless, only the direction in the bend plane of the momentum is affected by this choice, and an improved estimate may be obtained by transporting the momentum vector along the particle trajectory to any desired evaluation point.

As indicated by the diagram in Figure 5.2, the geometry of photon conversions leads to a systematic bias in the angle between the electron and positron momenta as evaluated at the coordinate origin. The bias increases for larger conversion radii and for lower energy photons. For the range of radii of reconstructed converted photons in

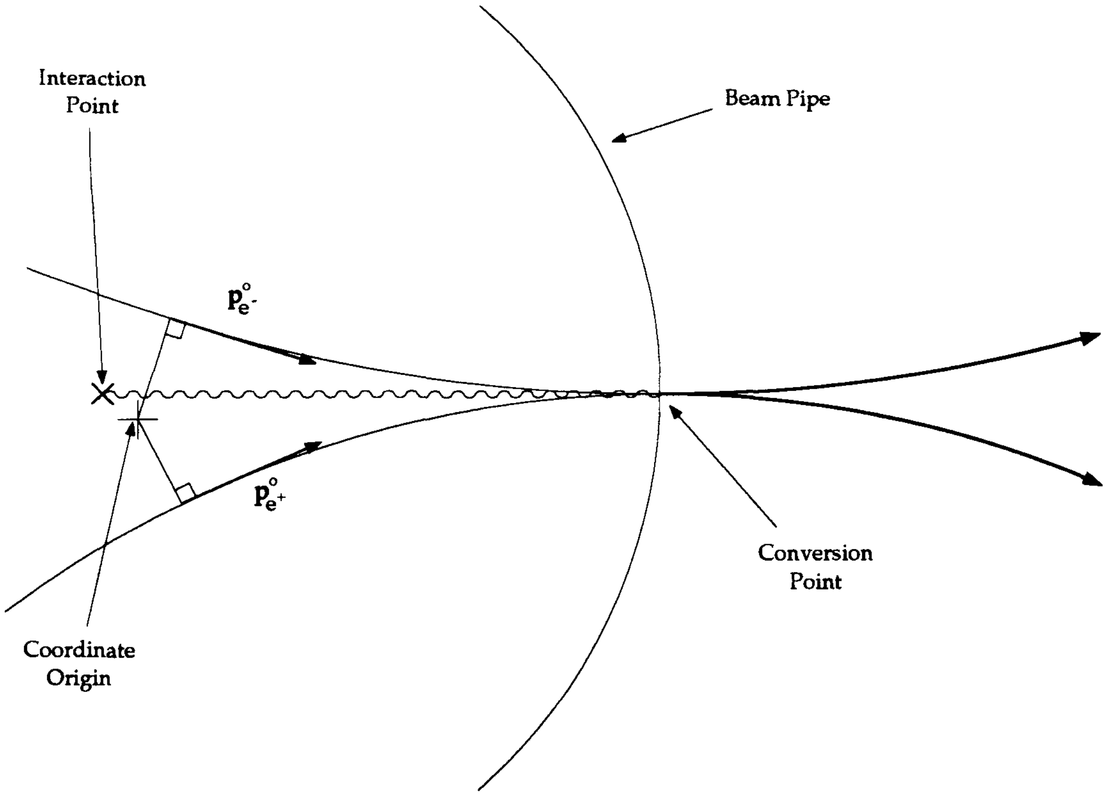

Figure 5.2 Expanded view of the region containing the interaction point and the photon's conversion point in the above diagram. The curvature of the tracks has been exaggerated in order to clarify the geometry. The heavy lines represent the actual trajectories of the electron and positron; the backward continuations of the projected track circles are drawn in a lighter weight. The momentum vectors shown, $p^o_{e\pm}$, are the track momenta evaluated at the trajectories' closest approaches to the coordinate origin.

the Mark III apparatus, and for photon energies greater than 0.5 GeV, the bias is of the order 100–200 mr, with the positron's momentum offset in the $+\phi$ direction from the electron's. This bias is to be compared with the intrinsic opening angle of approximately 1 mr and the single-track angular resolution of the drift chamber in the bend plane of approximately 2 mr.

The small intrinsic opening angle is the most distinctive feature of electron-positron pairs arising from photon conversions. As a result of the angular bias discussed above, however, the opening angle constructed from the momentum vectors normally returned by the reconstruction program is a very poor variable in which to observe this feature. Due to the broadening of the opening angle distribution, an efficient selection of conversion candidates on this basis alone would provide inadequate background rejection.

It is therefore necessary to attempt to reconstruct the conversion vertex and evaluate the momenta at that location in order to obtain the more precise information needed for a satisfactory identification of conversion candidates.

Standard algorithms are available for the reconstruction of two-particle vertices, such as those arising from the decays of K^o_S or Λ particles. However, these algorithms generally depend upon the assumption that the particles are produced with a non-zero opening angle and therefore that their trajectories will cross in the bend-plane projection. These algorithms are unsuitable for the present purpose.

The algorithm used in this analysis is specialized to the unique properties of the e^+e^- pairs arising from photon conversions. The helices of the electron and positron tracks are, ideally, nearly tangent at the point of conversion. Projected into the bend plane, the tracks should appear as two nearly tangent circles. The task of the conversion vertex finder is to determine the location of the photon conversion by obtaining an estimate of the point of tangency, in the face of track parameters that, including the effects of measurement errors, do not describe precisely tangent circles.

In order to perform the vertex position calculation, candidate pairs of oppositely charged tracks are divided into categories based on the configuration of the projections of the tracks in the bend plane. Each projected trajectory forms an arc of a circle; the circles are completed, and the pair classified according to the overlap of the two resulting circles. The configurations corresponding to the defined categories, I–VI,[2] are displayed

---

[2] A Category 0 is defined as the case where the centers of the two circles are exactly coincident. In this case, there is no way to define a unique vertex, so the procedure picks an arbitrary point and returns an error indication. No Category 0 pairs are actually

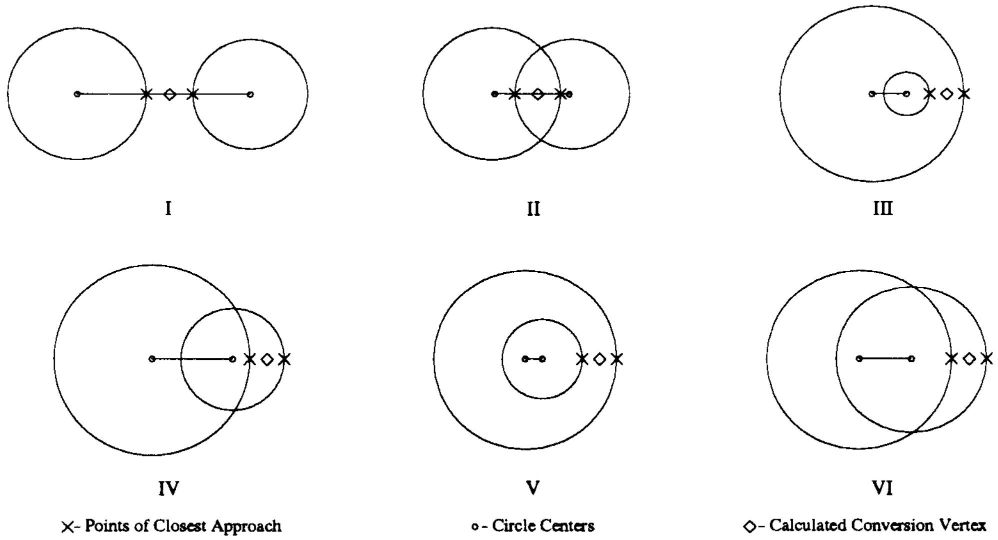

Figure 5.3 Summary of the definitions of the various categories of crossing types.

in Figure 5.3. In each case, the conversion location is taken to be on the line joining the circle centers, midway between the points on that line where it intersects the two circles. The location selected as the conversion point in the bend plane is marked with a diamond symbol in each diagram in the figure.

The z coordinate of the conversion point is taken to be the mean of the z coordinates of the points on the tracks closest to the estimated conversion location. These points are marked with crosses in the diagrams. The symbol $\mathbf{x}_{conv}$ is used for the 3–vector location of the conversion point.

Even a very loose restriction on the opening angle between the uncorrected momenta $\mathbf{p}^{o}_{e^{\pm}}$ eliminates all but Category I and II pairs. Inspection of the diagrams shows that this is reasonable behavior. Only in those categories are the track curvatures opposite near the estimated conversion point, as expected for oppositely charged particles traveling in approximately the same direction.

---

found in the data, however.

For each track in a pair, the track parameters are re-evaluated at the points of closest approach to the candidate conversion point. The momenta at these points, $\mathbf{p}^*_{e\pm}$, are obtained by transporting the momenta evaluated at the coordinate origin, $\mathbf{p}^o_{e\pm}$, along the track helices to the new points. The sum of the recalculated momentum vectors, $\mathbf{p}_{conv} \equiv \mathbf{p}^*_{e+} + \mathbf{p}^*_{e-}$, is taken as the momentum of the pair.

Section 3 Pair Characterization Variables

The vertex-finding procedure assumes that the projected track circles are tangent. Therefore, by construction, the momentum vectors evaluated at the conversion point, $\mathbf{p}^*_{e\pm}$, are parallel in the bend plane, and this algorithm does not attempt a direct estimate of the opening angle at that point. However, equivalent information suitable for identifying candidate pairs as photon conversions is available.

Six variables are defined. Two describe the separation between the track helices at the estimated point of conversion; this separation should be zero to within the precision of the measurement for tracks arising from a real conversion. Two describe the alignment of the electron-positron pair's momentum evaluated at the estimated point of conversion with the displacement from the beam interaction point to the conversion point; for a real photon conversion, these vectors should be aligned to within the precision of the measurement. The fifth variable describes the alignment of the electron and positron momenta in the r-z plane at the estimated conversion point; their trajectories should be parallel for a real conversion. The final variable is the transverse distance of the conversion point from the detector centerline; real conversions detectable in the apparatus should originate only in the annular region beginning with the beam pipe and continuing out through the inner wall of the main drift chamber.

The track separation variables Δ and Δz are defined as follows. The circle separation, Δ, is defined as the distance in the bend plane between the circles that are the projections of the tracks, measured along the line connecting the centers of the circles. The sign of the circle separation is defined to be positive for Category I (disjoint) and negative for Category II (overlapping) tracks. The z separation, Δz, is defined as the difference in the z-coordinates of the points (marked in Figure 5.3 with the symbol "$\times$") on the tracks corresponding to the points on the projected circles nearest the estimated conversion point:

$$\Delta z \equiv z^*_{e^+} - z^*_{e^-}.$$

Both Δ and Δz would be zero for the ideal case of tangency of the track helices. The transverse separation variable Δ is a measure of the correctness of the assumption that the two tracks were indeed parallel at a common point of origin.

The vertex-momentum alignment variables $\Delta\phi_{r,p}$ and $\Delta \tan\lambda_{r,p}$ are defined according to the following procedure. The momentum of the electron-positron pair at the estimated conversion point, $\mathbf{p}_{conv}$, and the location of this point, $\mathbf{x}_{conv}$, are determined by the vertex-finding procedure described above. The known beam interaction point location,[3] $\mathbf{x}_{beam}$, is then used to calculate the displacement of the conversion point from the interaction point:

$$\mathbf{\Delta x}_{conv} \equiv \mathbf{x}_{conv} - \mathbf{x}_{beam}.$$

The bend plane alignment variable, $\Delta\phi_{r,p}$, is defined as the angle in the bend plane between $\mathbf{\Delta x}_{conv}$ and $\mathbf{p}_{conv}$. A positive value for this variable corresponds to a rotation of the vertex displacement in the $+\phi$ direction from the momentum vector. The variable is defined to take on values in the range $(-\pi, \pi]$. The polar alignment variable, $\Delta \tan\lambda_{r,p}$, is defined as the difference of the tangents of the dip angles of the momentum and the vertex displacement vectors. A positive value of this variable corresponds to a larger value of

---

[3] Determined on a run-by-run basis from an examination of the electron and positron trajectories in $e^+e^- \rightarrow e^+e^-$ elastic scattering events.

$\tan\lambda$ for the vertex displacement than for the momentum. Both of these variables would be zero in the ideal case.

The size of the interaction region places some limits on the precision to which the vertex-momentum alignment can be required, since the alignment is calculated with respect to the measured centroid of the beam. The 1σ transverse size of the beam is roughly $50\mu \times 500\mu$. This can contribute up to approximately 7 mr to the misalignment in the bend plane, a relatively small effect. However, the longitudinal bunch size of 3–5 cm can lead to a misalignment in $\Delta\tan\lambda_{r,p}$ of up to approximately 0.5, and this dominates the width of the distribution of this variable.

The polar tangency variable, $\Delta\tan\lambda$, is defined as the difference of the tangents of the dip angles of the positron and electron track momenta. Positive values correspond to a larger value of $\tan\lambda$ for the positron momentum. The $\Delta\tan\lambda$ variable, too, would be expected to be zero in the ideal case of tangent track helices.

Finally, the conversion radius, r_{conv}, is defined as the perpendicular distance of the estimated conversion point from the detector axis. No real photon conversions would be expected to occur inside the volume of the beam pipe, due to the absence of material. Conversions occurring outside the inner wall of the main drift chamber would be expected to miss progressively more of the planes of Layer 2 with increasing radius. Tracks originating from such "late" conversions no longer satisfy the requirements of the track recognition procedure, as described in Appendix A, and so such conversions can not be reconstructed.[4] The expected range of radii for real photon conversions is

---

[4] This is a slight oversimplification. Tracks originating from "late" conversions would, of course, miss all of Layer 1. Under the missing-hit criteria of the track dictionary used in this analysis, such tracks must be detected in all of Layers 2A, 2B, 3, and 5. Layer 2A and 2B hits are counted when at least four of the six inner (for 2A) or outer (for 2B) wires of Layer 2 are hit. Therefore, assuming perfect efficiency, a track could originate following the first two wires of Layer 2 and still generate a Layer 2A hit; however, the additional material thus available for production of detectable photon conversions is only a 3.8% contribution to the total. The inclusion of the effect of imperfect detection efficiency can be expected to reduce this to approximately 3%.

therefore [0.075, 0.145] m. The actual range of r_{conv} will, of course, be broadened by measurement error.

Section 4 Selection of Photon Conversions

The full Mark III reconstructed J/ψ event sample is stored on over 500 tape cartridges and totals approximately 67 GB of data. It is very time-consuming to read the entire data set, and, as only a very small fraction of all events are expected to contain a converted photon, the event selection proceeds in two phases: a loose selection which reduces the size of the data set to the point that it is convenient to re-read on a regular basis, and a final selection. These are described separately below.

Preliminary Selection

In each event, all possible pairs of a positive and a negative track are formed. Both tracks are required to have successful three-dimensional reconstructions of their momenta. Using the momenta evaluated for the tracks at their point of closest approach to the coordinate origin, the cosine of the uncorrected opening angle, $\cos\theta^o_{open}$, is calculated as:

$$\cos\theta^o_{open} \equiv \frac{\mathbf{p}^o_{e+} \cdot \mathbf{p}^o_{e-}}{|\mathbf{p}^o_{e+}||\mathbf{p}^o_{e-}|}$$

As a loose preliminary selection, the requirement

$$\cos\theta^o_{open} > 0.96$$

is imposed. The distribution in this variable, as discussed above, is broadened by the selection of evaluation point for the momentum. The broadening increases with decreasing photon energy, and so the efficiency of this test is energy-dependent. For photons of energy greater than 0.5 GeV, it is a loose requirement; in a Monte Carlo simulation, only 5.6% of converted photons with generated energy in the range [0.5, 0.6]

GeV *fail* this test.[5] The inefficiency rises to 19.8% in the range [0.2, 0.3] GeV, but at this energy a much larger fraction of converted pairs are lost as the lower momentum track falls below the drift chamber pattern recognition's minimum transverse momentum cutoff and fails to be reconstructed at all.

As mentioned above, this requirement on $\cos\theta^o_{open}$ eliminates all but Category I and II track pairs.

In the preliminary pair selection, the further requirement

$$\cos\Delta\phi_{r,p} > 0.5$$

---

[5] This is 5.6% of all photons which a) converted in the Monte Carlo simulation and b) had both of the resulting tracks reconstructed.

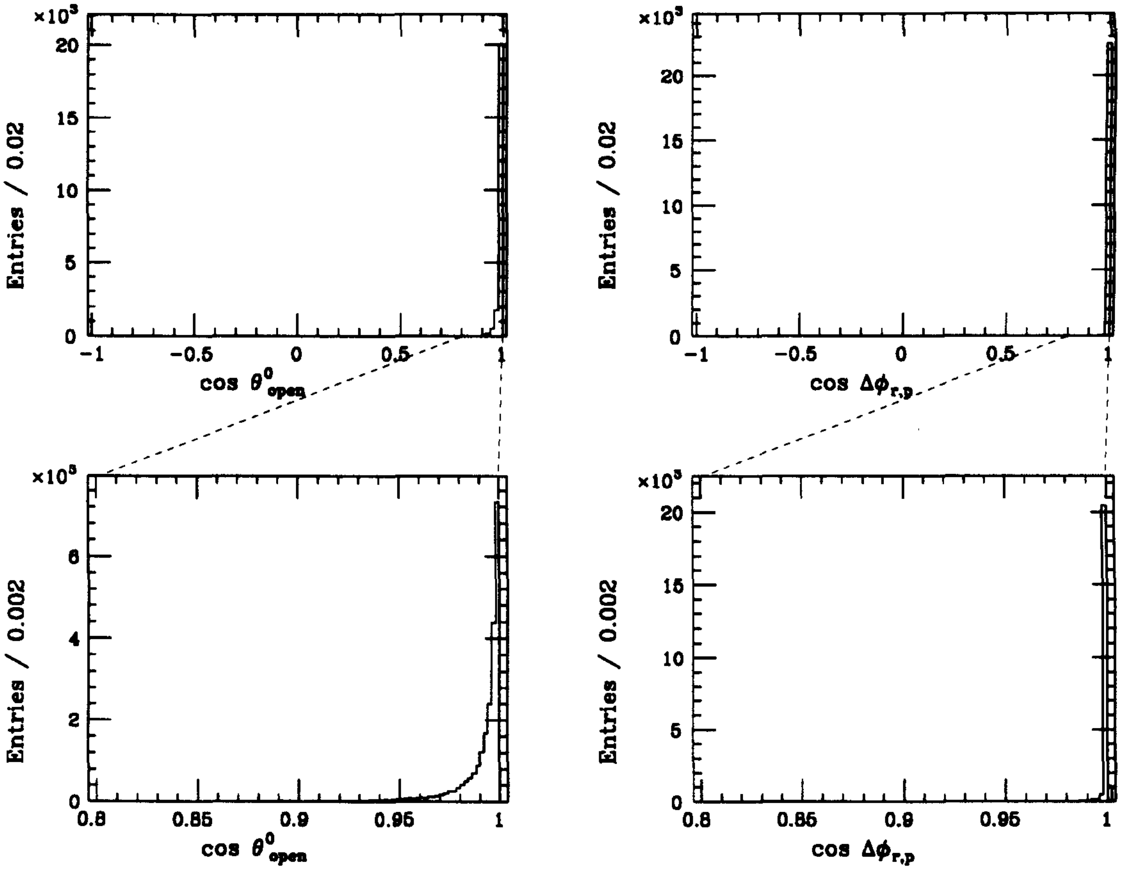

Figure 5.4 Distribution of the preliminary selection variables $\cos\theta^o_{open}$ and $\cos\Delta\phi_{r,p}$ for Monte Carlo converted photons.

is imposed, demanding that the momentum and the vertex displacement of the pair be roughly aligned. This is a very loose requirement for converted photons: only 1.1% of all reconstructed converted pairs in the Monte Carlo simulation fail this test.

Figure 5.4 displays the distributions of $\cos\theta^o_{open}$ and $\cos\Delta\phi_{r,p}$ resulting from the Monte Carlo simulation. The Monte Carlo data set consists of a sample of 4.3×10^6 photons generated isotropically in the laboratory, with a uniform distribution of energy over the kinematical range accessible in J/ψ decays, and allowed to convert as appropriate to the thickness of the material in the inner detector structure. The histograms contain entries for each converted photon with both resulting tracks reconstructed. This stage is reached by $(0.553 \pm 0.004)\%$ of all generated photons, and 0.65% of those with generated energies above 0.5 GeV.

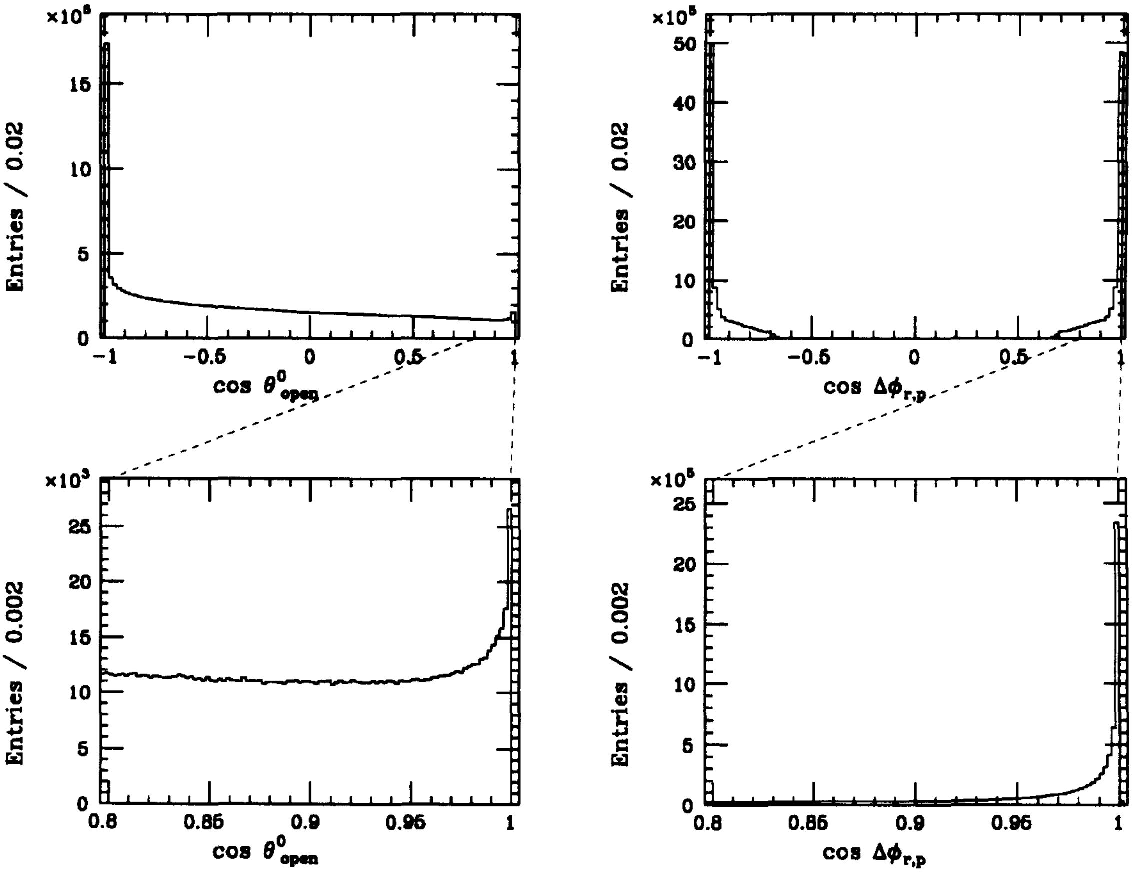

Figure 5.5 Distribution of the preliminary selection variables $\cos\theta^o_{open}$ and $\cos\Delta\phi_{r,p}$ for all track pairs in the data.

Of these Monte Carlo simulated pairs, a further $(92.3 \pm 0.2)\%$ (94.6% of those with energies above 0.5 GeV) satisfy the preliminary selection criteria discussed above.

Figure 5.5 displays the distributions of $\cos\theta^{o}_{open}$ and $\cos\Delta\phi_{r,p}$ in the data. Approximately 1.8% of all the events in the J/ψ data sample contain a pair which passes the preliminary restrictions on these variables, resulting in a data sample for further analysis of manageable size: 2.1 GB on 14 tape cartridges.

Final Selection

The final identification of e^+e^- pairs arising from photon conversions is done by imposing requirements on the six pair characterization parameters introduced above. Figure 5.6 displays the distributions of the six parameters in the Monte Carlo simulation following the preliminary selection, and Figure 5.7 displays the distributions for the data.

Each distribution, in both the data and the Monte Carlo simulation, shows a peak at the expected location, corresponding to tangential particle trajectories in the candidate pairs.

A conversion radius requirement is not imposed until the end of the selection process. The distinctive shape of the radius distribution, corresponding to the range of material and detection sensitivity from the beam pipe through the inner wall of the drift chamber, permits an immediate visual evaluation of the effects of the selection process on the data. Note that even at this stage of loose selection, an accumulation of entries is visible in the expected range in the radius distribution in the data.

Based on the study of the Monte Carlo simulation, and checking against the observed distributions in the data, the selection of candidate converted pairs is narrowed by imposing requirements on each of the geometrical variables defined above.

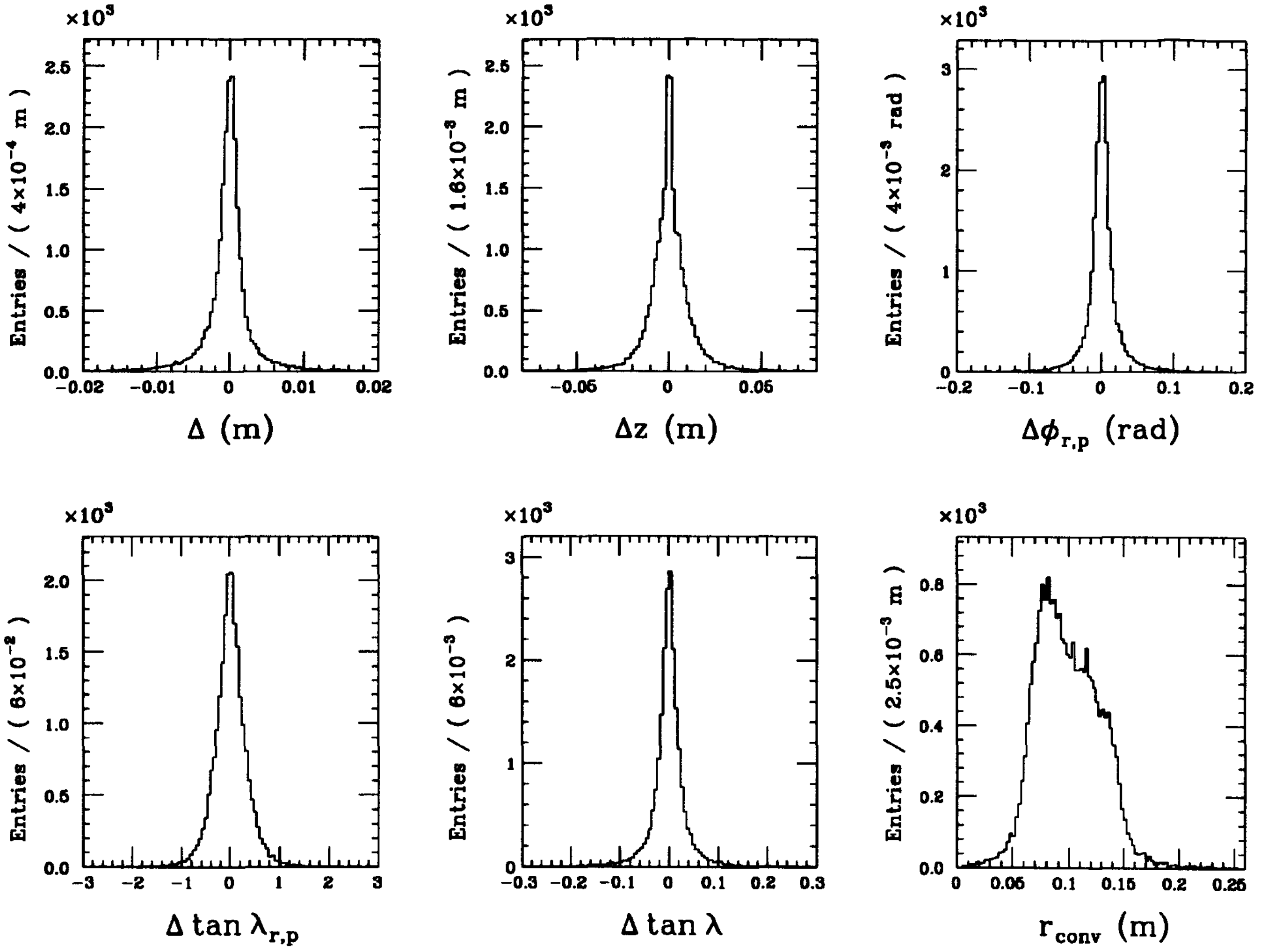

Figure 5.6 Distributions of the six pair characterization variables for Monte Carlo events which have passed the preliminary selection stage.

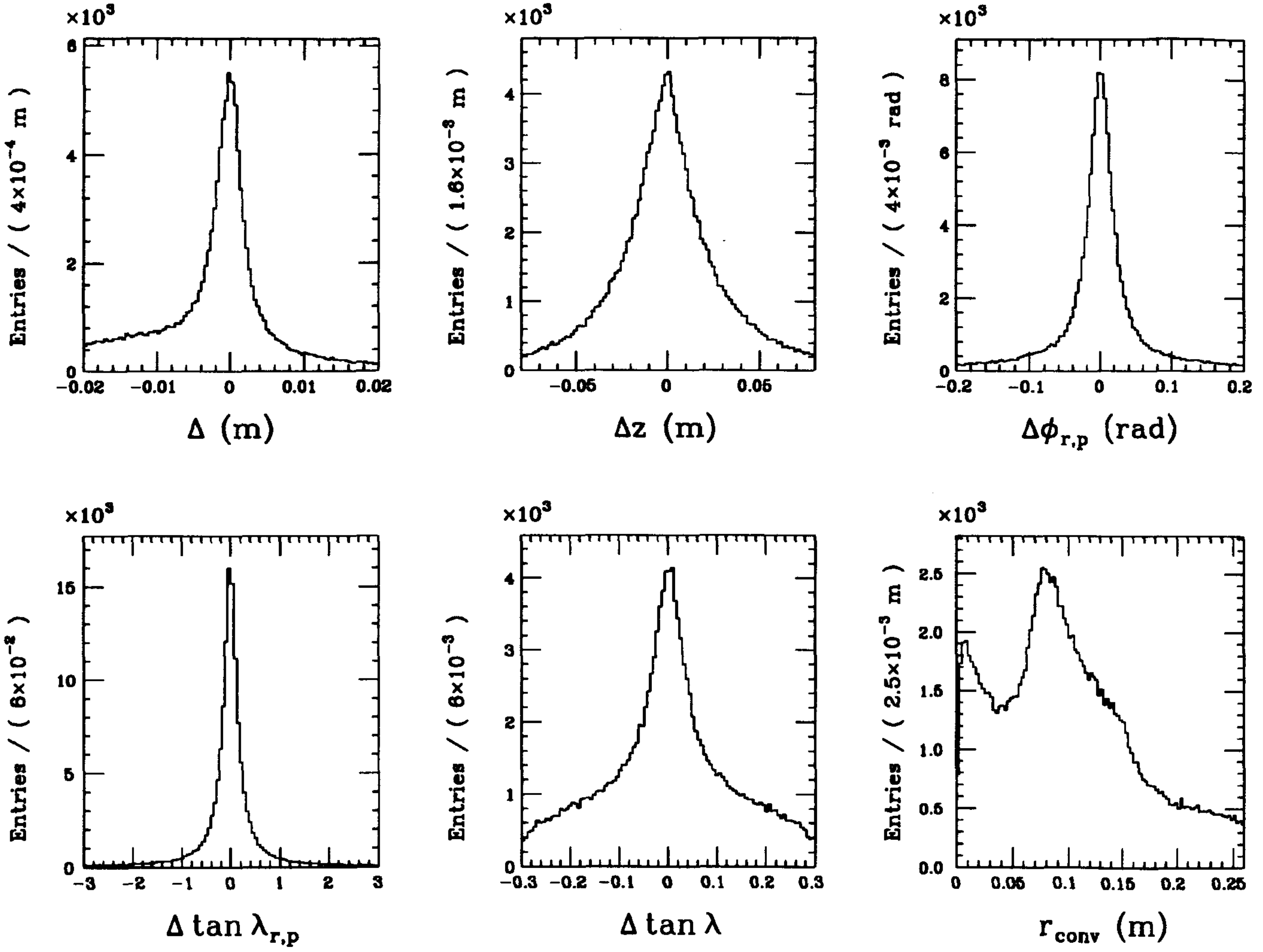

Figure 5.7 Distributions of the six pair characterization variables for events in the data which have passed the preliminary selection stage.

The selected set of requirements is:

$$-0.006\,\mathrm{m} < \Delta < 0.006\,\mathrm{m},$$

$$-0.04\,\mathrm{m} < \Delta z < 0.04\,\mathrm{m},$$

$$-50\,\mathrm{mr} < \Delta\phi_{r,p} < 50\,\mathrm{mr},$$

$$-0.75 < \Delta\tan\lambda_{r,p} < 0.75,$$

and

$$-0.1 < \Delta\tan\lambda < 0.1.$$

The distributions of the six variables for the Monte Carlo simulation and the data, following the application of these five conditions, are shown in Figures 5.8 and 5.9, respectively. For each of the five variables on which a requirement is imposed, Δ, Δz, $\Delta\phi_{r,p}$, $\Delta\tan\lambda_{r,p}$, and $\Delta\tan\lambda$, the distribution of that variable reflects the imposition of the requirements on the other four. This permits a visual evaluation of the relative importance of each requirement in the final selection.

The radius distribution shown includes the effects of the requirements on all five variables. Inspection of this distribution in the data shows a clean signal for external conversions in the detector material, with little background.

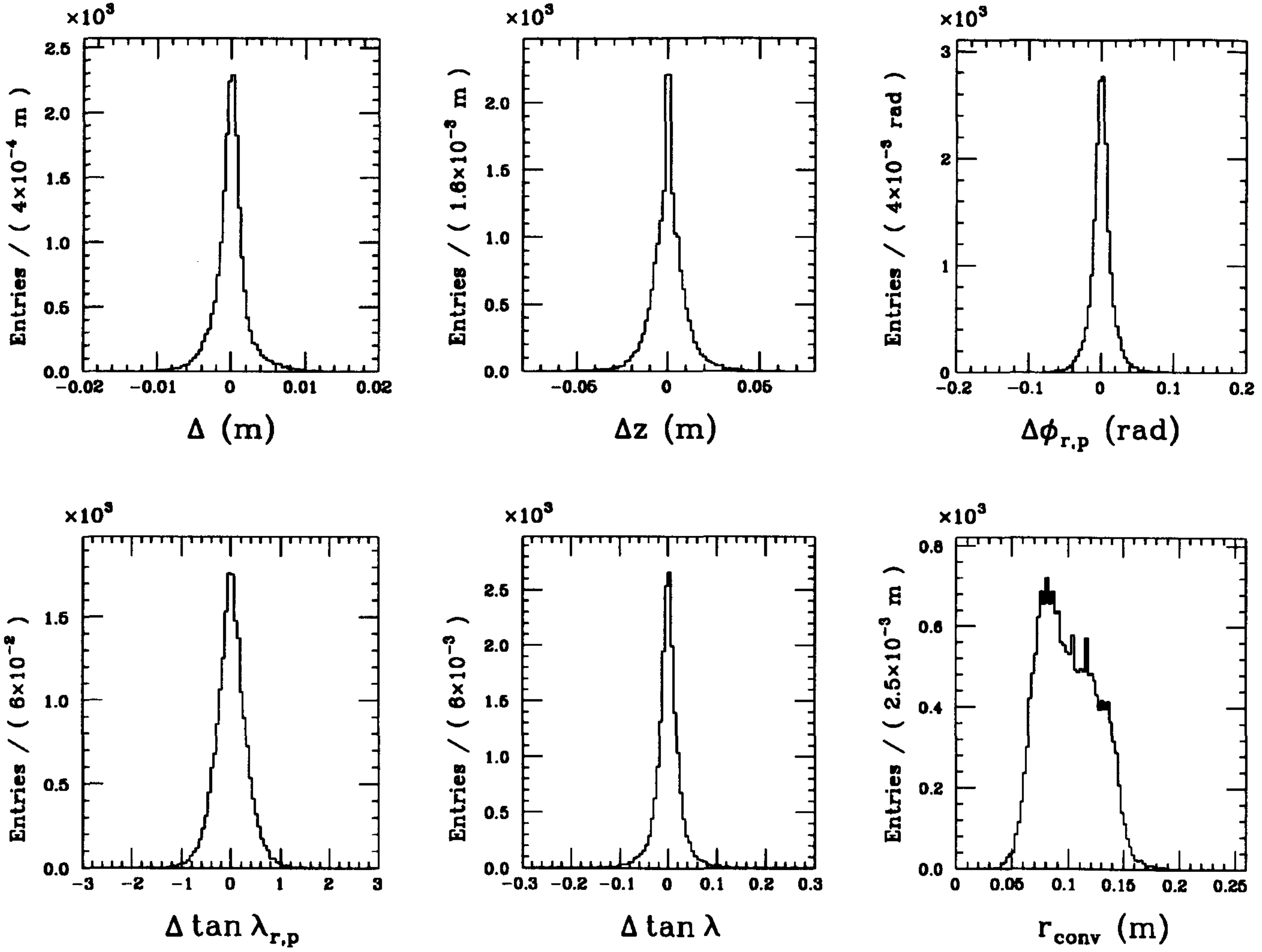

Figure 5.8 Distributions of the six pair characterization variables for Monte Carlo events. In each plot, the effect of the pair selection requirements imposed on the other parameters (excepting the conversion radius) is shown.

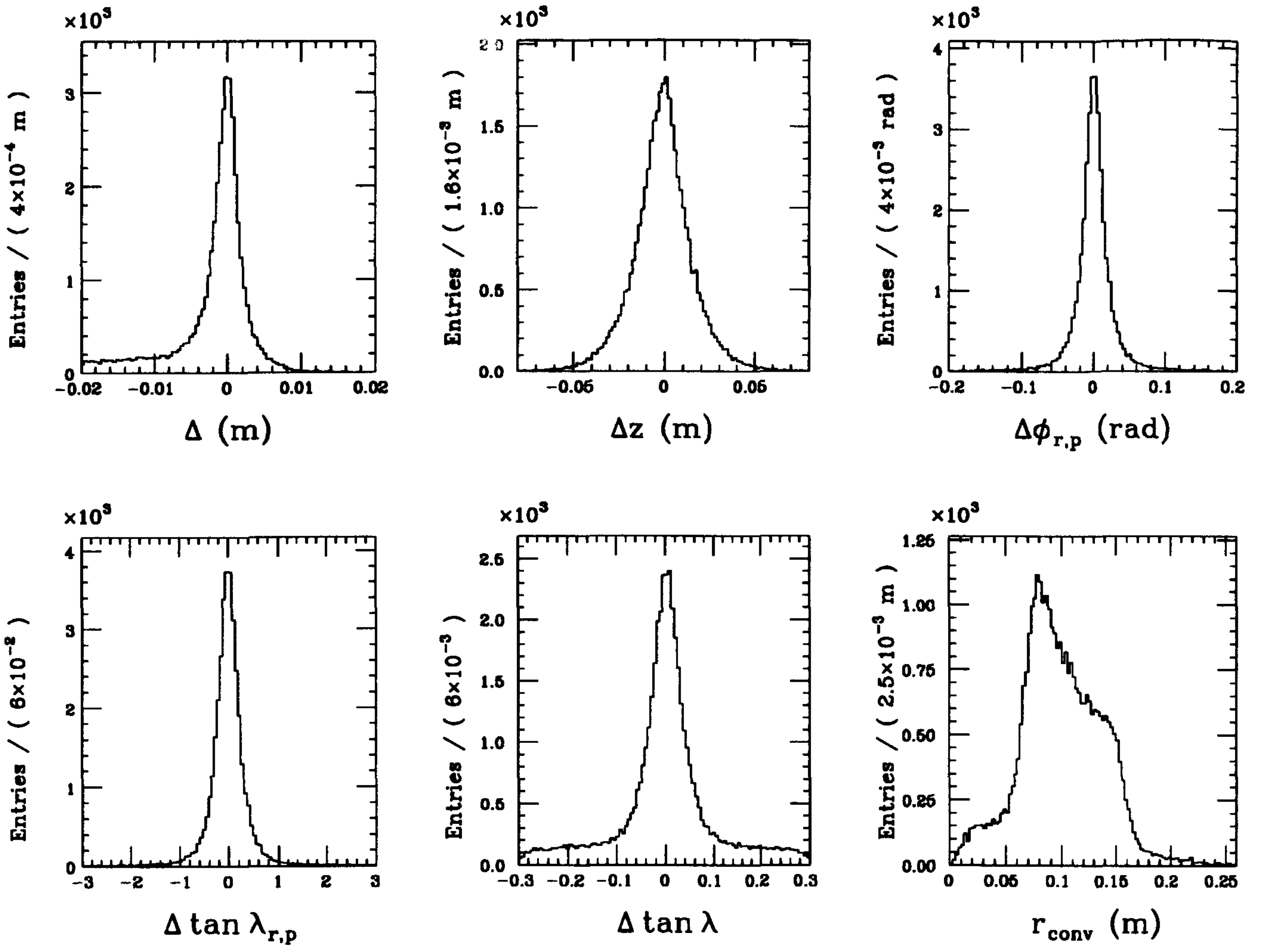

Figure 5.9 Distributions of the six pair characterization variables for events in the data. In each plot, the effect of the pair selection requirements imposed on the other parameters (excepting the conversion radius) is shown

The dominant background to the photon conversion signal arises from accidental combinations of nearly parallel tracks in the data. The effect of this background is most clearly visible in the distribution of the circle separation parameter Δ. Figures 5.10a and 5.10b are scatter plots of Δ versus r_{conv} in the Monte Carlo simulation and the data, respectively. In these plots, the requirements on Δz, $\Delta\phi_{r,p}$, and $\Delta \tan \lambda_{r,p}$ have already been imposed. No requirement has been imposed on $\Delta \tan \lambda$. The plots contain only a fraction of the total data samples, to avoid saturating the images.

The Monte Carlo plot shows the expected band at $\Delta = 0$ within the allowed range of radii. (The slight diagonal scatter reflects the correlated errors of the two parameters: measurement errors which lead to positive values of Δ also tend to lead to positive errors on r_{conv}, and vice-versa.) The plot for the data shows this band, but also another apparent structure: a band extending from negative values of Δ at large radii through to $\Delta = 0$ at small radii. This apparent structure, due to accidental combinations, underlies the desired signal, especially at radii in the vicinity of the beam pipe, $r_{conv} = 0.075\text{m}$.

Fortunately, the additional variable $\Delta \tan \lambda$ is available to further narrow the selection. Figure 5.11 shows the distribution of this variable following the restrictions on Δz, $\Delta\phi_{r,p}$, and $\Delta \tan \lambda_{r,p}$, but with no restriction on Δ, in the Monte Carlo simulation and the data. The effect of the restriction

$$-0.1 < \Delta \tan \lambda < 0.1$$

on the joint distribution of Δ and r_{conv} is shown in Figures 5.12a and b.

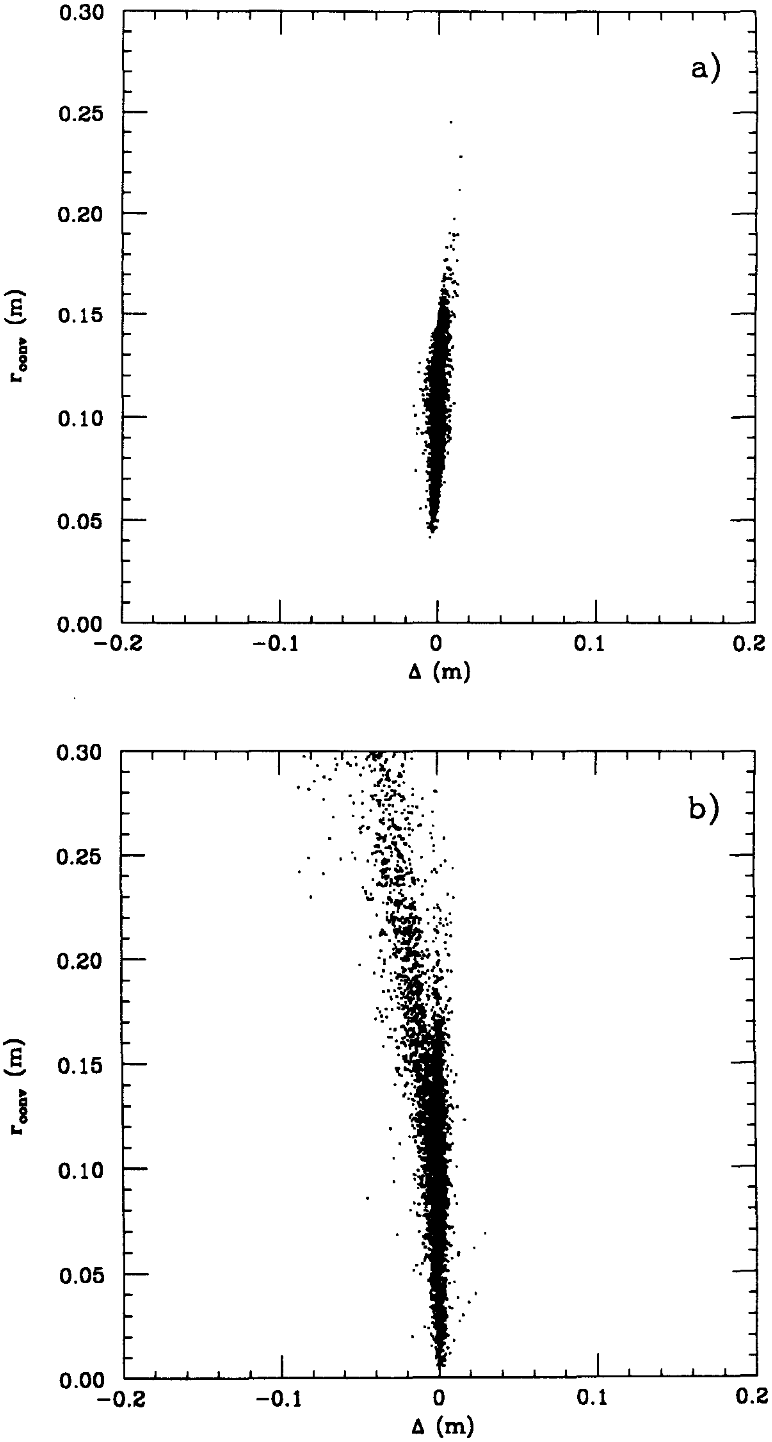

Figure 5.10 Scatter plots of the circle separation parameter Δ versus the estimated conversion radius r_{conv}: a) Monte Carlo, b) experimental data.

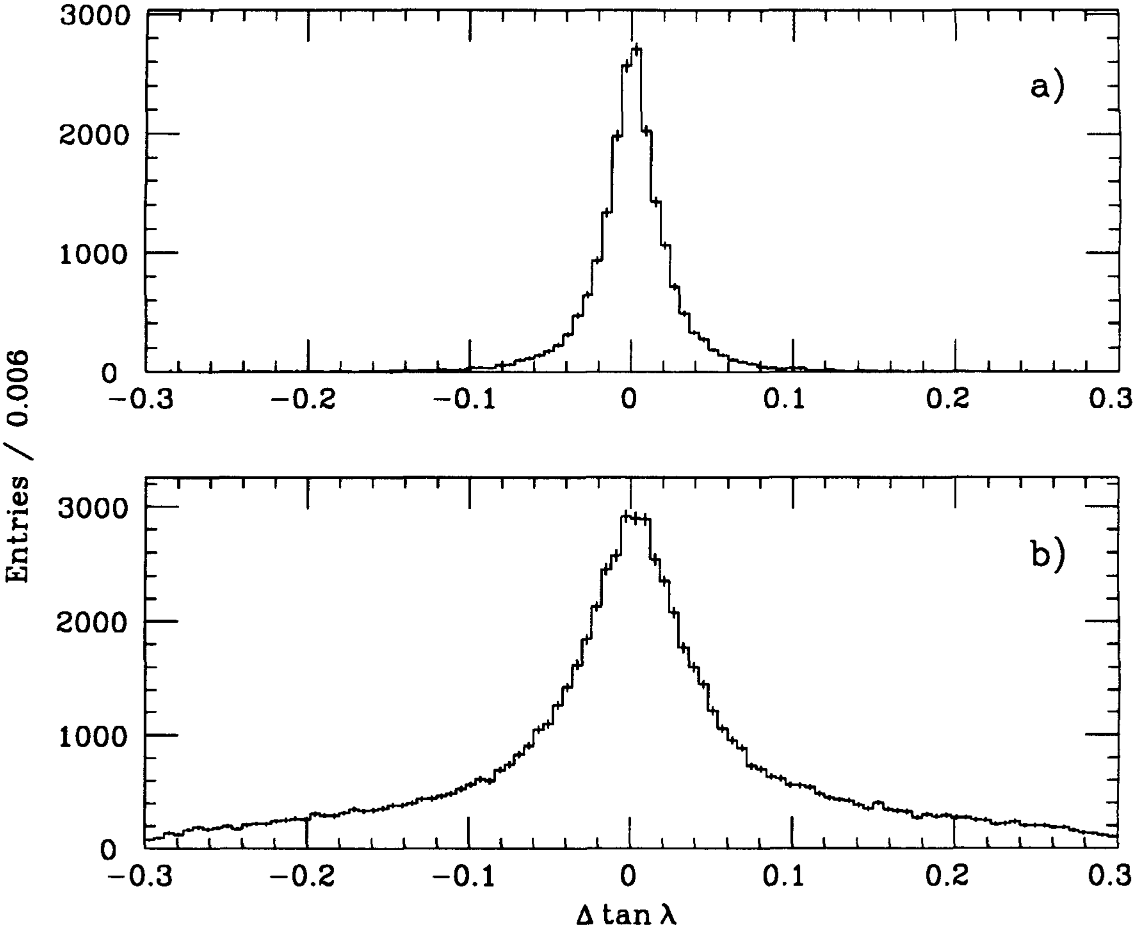

Figure 5.11 Distribution of the polar tangency parameter $\Delta \tan \lambda$ following the application of the conditions on Δz, $\Delta\phi_{r,p}$, and $\Delta \tan \lambda_{r,p}$: a) Monte Carlo, b) data.

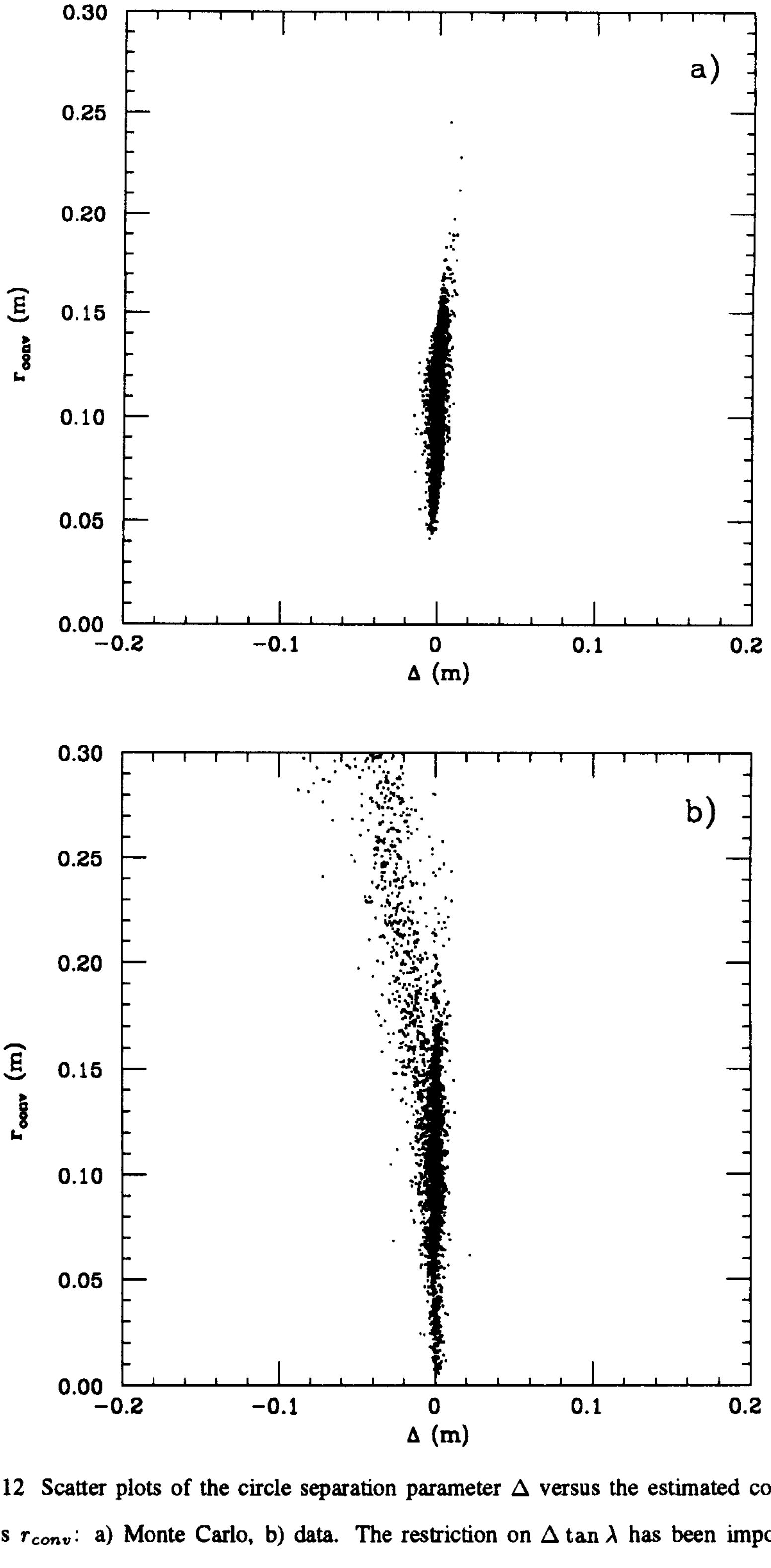

Figure 5.12 Scatter plots of the circle separation parameter Δ versus the estimated conversion radius r_{conv}: a) Monte Carlo, b) data. The restriction on $\Delta \tan \lambda$ has been imposed.

The rejection rates of the various requirements are summarized in Table 5.1. For each requirement, and for both the Monte Carlo simulation and the data, two numbers are displayed: the number of candidate pairs (assumed to have passed the preliminary selection) failing the test in the absence of the other requirements — the *independent* rejection; and the additional number of pairs failing the test when the other four requirements have already been imposed — the *marginal* rejection. Note that the rejection rates in the data are not quoted with errors — they are simply a report of the effect of the selection process. The Monte Carlo rejection rates are estimates of the rejection rates as applied to simulated data, and therefore are quantities with errors.

Table 5.1 Summary of the pair rejection percentages for the five pair quality requirements. The definitions of the "independent" and "marginal" rejection rates are in the text.

	Monte Carlo rejection		Data rejection	
Parameter	Independent	Marginal	Independent	Marginal
Δ	$(8.3 \pm 0.2)\%$	$(3.2 \pm 0.1)\%$	50.6%	30.1%
Δz	$(2.9 \pm 0.1)\%$	$(0.7 \pm 0.1)\%$	27.0%	3.3%
$\Delta\phi_{r,p}$	$(6.6 \pm 0.2)\%$	$(1.2 \pm 0.1)\%$	34.7%	9.0%
$\Delta \tan \lambda_{r,p}$	$(4.1 \pm 0.1)\%$	$(3.1 \pm 0.1)\%$	20.8%	7.8%
$\Delta \tan \lambda$	$(4.0 \pm 0.1)\%$	$(1.8 \pm 0.1)\%$	46.7%	25.4%

Note that the marginal rejection rates for the Δ and $\Delta \tan \lambda$ requirements in the data are considerably larger than the others. This implies that the restrictions on these two variables are the ones essential to defining the converted photon data sample.

Taken together, the five restrictions eliminate $(15.8 \pm 0.3)\%$ of the Monte Carlo converted photons (15.2% of those with generated energies above 0.5 GeV), and 89.5% of the pairs in the data.

The distributions of the conversion radius, r_{conv}, in the Monte Carlo and the data, following the application of all five requirements, are recapitulated in Figures 5.13a and

b. (These are the same histograms shown for r_{conv} in Figures 5.8 and 5.9.) The final step in the selection is accomplished by requiring that

$$0.05\text{m} < r_{conv} < 0.17\text{m}.$$

This condition rejects a further $(0.78 \pm 0.07)\%$ of the Monte Carlo converted photons (0.93% of those with generated energies above 0.5 GeV), and 10.4% of the pairs in the data.

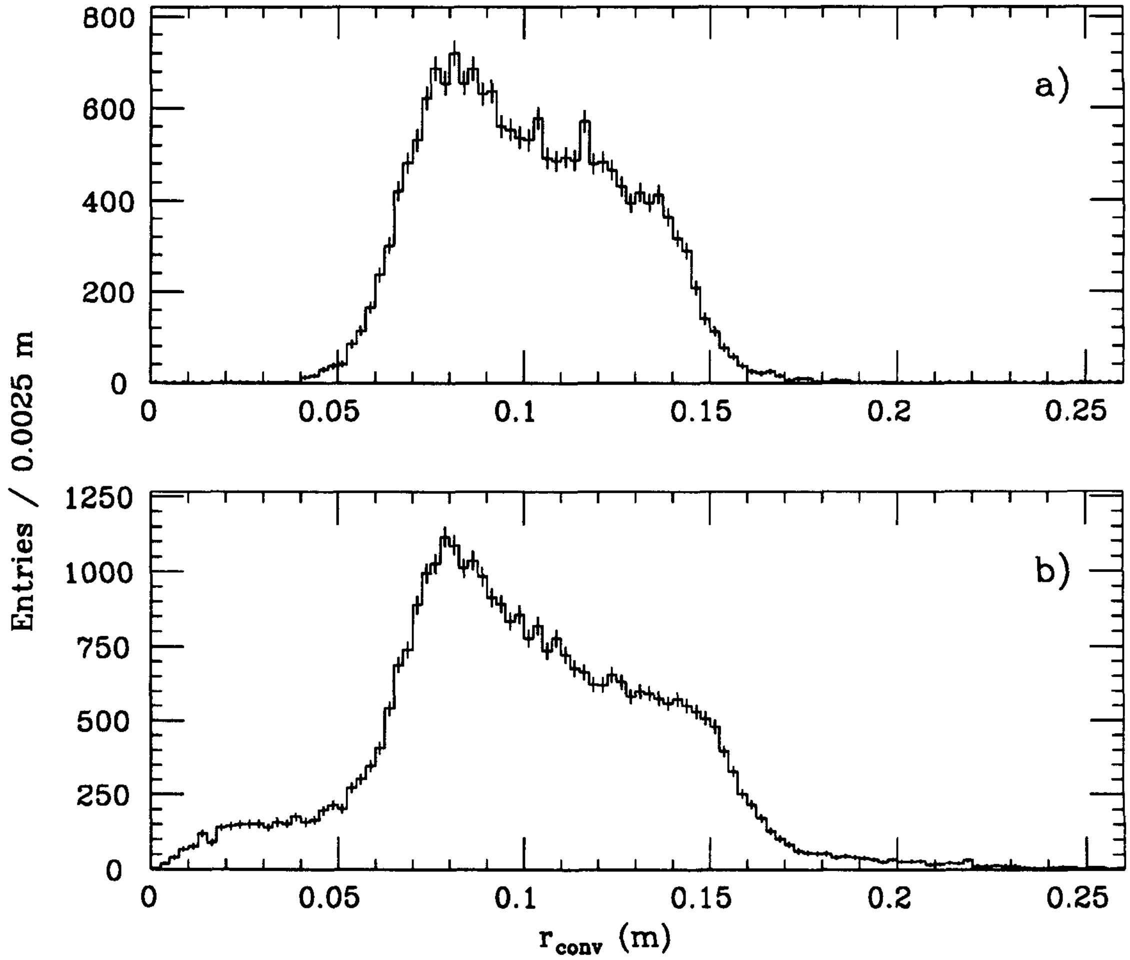

Figure 5.13 Distribution of the conversion radius, r_{conv}, following the application of the five pair quality conditions: a) Monte Carlo, b) data.

Note that the radius distribution does not show evidence for individual peaks corresponding to the seven discrete layers of material in the sensitive region (the beryllium beam pipe, the five layers of foam forming the structure of the inner drift chamber, and the inner wall of the main drift chamber). This is a result of the inherent difficulty of locating the precise point of tangency of the projected track circles along the line of tangency. This difficulty increases with increasing energy, as the curvature of the electron and positron tracks decreases.

The resolution on r_{conv} obtained from the Monte Carlo simulation varies from approximately 0.01 to 0.02 m over the range of energies from 0.5 to 1.55 GeV.

Section 5 Efficiency and Energy Resolution

The efficiency for observing a photon as a converted pair, subject to the analysis requirements outlined above, is determined from the Monte Carlo simulation. The probability for detecting a generated photon is displayed, as a function of generated photon energy, in Figure 5.14. The error bars arise from the Poisson statistics on the number of observed events in each bin.

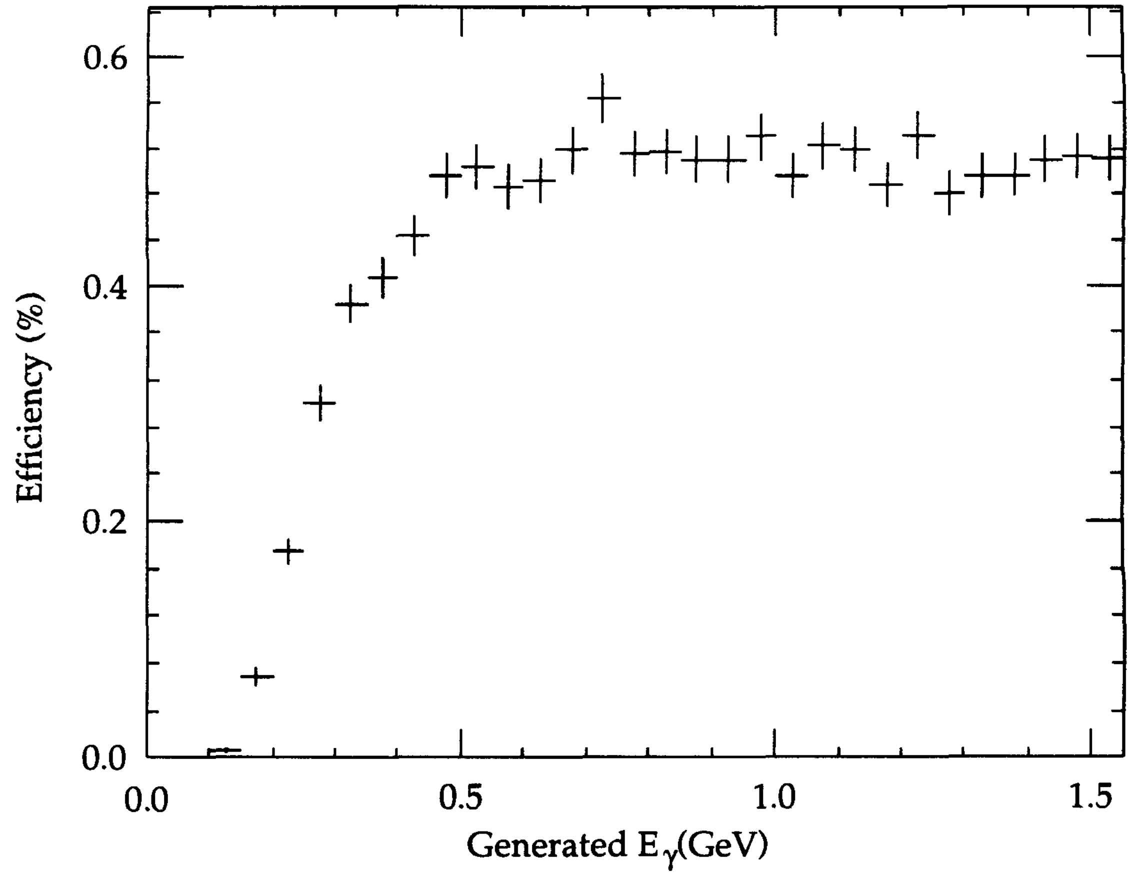

Figure 5.14 The detection efficiency for observing a photon as a converted pair, as a function of its generated energy, as determined by Monte Carlo simulation.

The efficiency may be seen to be extremely small for low energies, rising to a plateau of approximately 0.5% for energies greater than 0.5 GeV. A linear fit to the efficiency plot for energies above 0.5 GeV yields the result:

$$\epsilon_\gamma = \left((5.3 \pm 0.2) - (0.2 \pm 0.2)\frac{E_\gamma}{1\,\mathrm{GeV}}\right) \times 10^{-3}.$$

The slope is not statistically significant and will henceforth be ignored. The linear fit has a χ^2 per degree of freedom of 0.87. Fitting to a constant term alone, the χ^2/d.o.f. is 0.90, with a result of $\epsilon_\gamma = (5.11 \pm 0.04) \times 10^{-3}$. For the final value of the efficiency, we nevertheless choose to include a contribution to the uncertainty in the determination of the efficiency of 0.2×10^{-3}, based on the errors obtained in the linear fit. We also include an additional 5% uncertainty in ϵ_γ, or 0.26×10^{-3}, as an estimate of the uncertainty due to the selection procedure and the limited accuracy of the Monte Carlo simulation of the selection variables. The final value to be used for the efficiency is, then:

$$\epsilon_\gamma = (5.1 \pm 0.5) \times 10^{-3}.$$

The fractional energy resolution obtained for converted photons in the Monte Carlo simulation as a function of generated energy is shown in Figure 5.15. The quantity displayed is the Gaussian width obtained from a series of fits, in bins of generated energy, to the distribution of the quantity

$$\frac{E_{\gamma,meas} - E_{\gamma,gen}}{E_{\gamma,gen}}.$$

The fit function used was the sum of a Gaussian distribution and a polynomial background term. The values displayed are the results of fits using a constant background. The error bars displayed are derived from a combination of the statistical errors on the fits and the variation of the fit value with the choice of background polynomial. As expected due to the shape of the drift chamber momentum resolution curve, the converted photon energy resolution worsens slowly with energy.

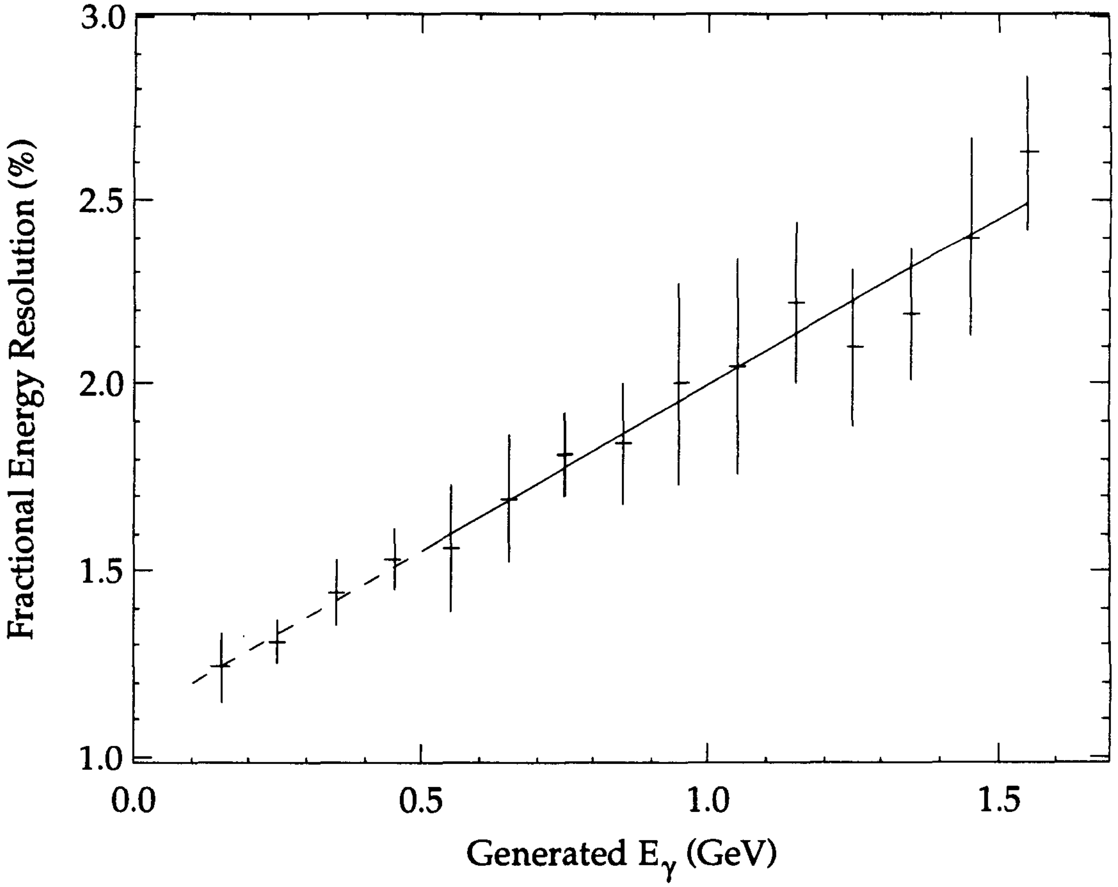

Figure 5.15 The fractional energy resolution, $\sigma_{E_\gamma}/E_\gamma$, for photons observed as a converted pair, as a function of generated energy, as determined by Monte Carlo simulation. Shown overplotted is a linear fit to the resolution as a function of energy over the range 0.5–1.55 GeV.

The variation of the fractional resolution with energy is then itself fit to an ad-hoc linear function over the range from 0.5 to 1.55 GeV, yielding the result

$$\frac{\sigma_{E_\gamma}}{E_\gamma} = \left((1.11 \pm 0.18) + (0.89 \pm 0.18)\frac{E_\gamma}{1\ \mathrm{GeV}}\right) \times 10^{-2}.$$

The fitted line is shown in the figure. The errors on the two terms in the fit are highly correlated; the actual uncertainty in the evaluation of the function over the fit interval varies in the range between 0.06×10^{-2} and 0.11×10^{-2}. The functional form has no theoretical significance; it is merely the simplest function adequately describing the variation in the data.

Section 6 Observed Energy Spectrum

The energy spectrum of pairs passing all the conversion identification requirements above is shown in Figure 5.16a. The spectrum falls rapidly with increasing energy; in order to clarify the details of the end point of the spectrum, an expanded view, for energies above 0.75 GeV, is shown in Figure 5.16b.

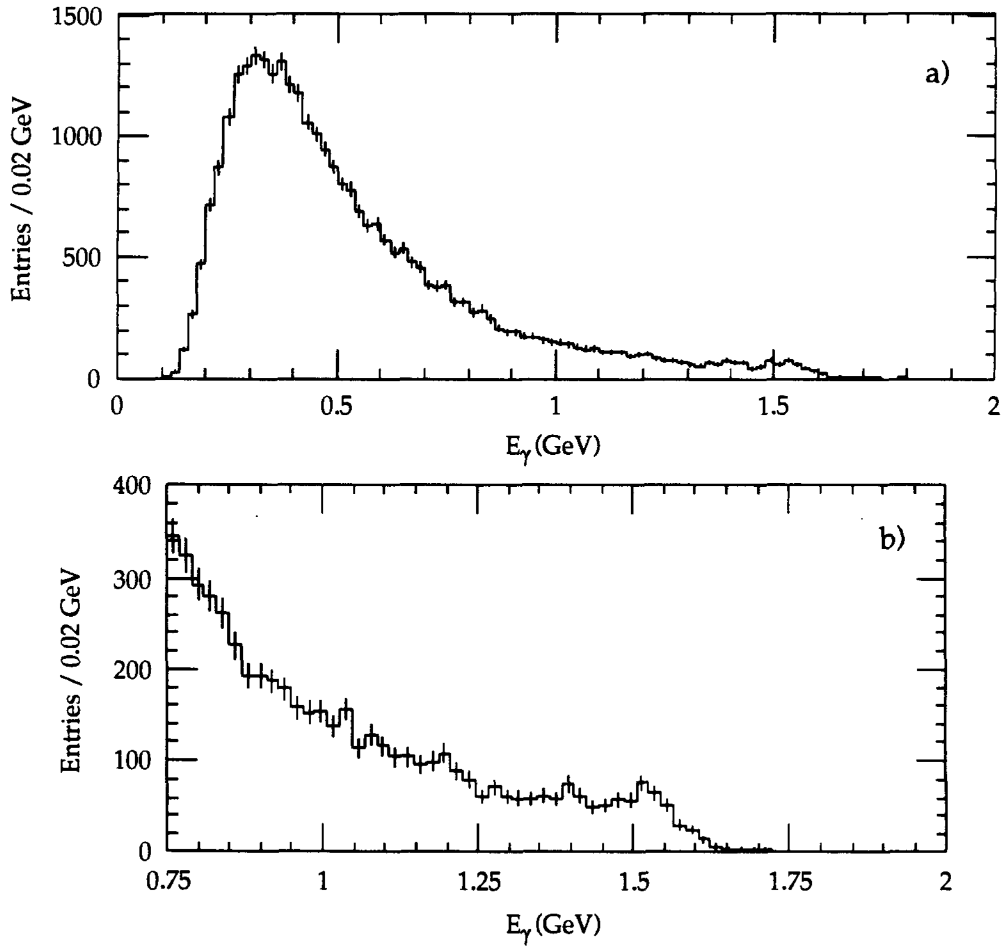

Figure 5.16 Observed energy spectrum of converted photons: a) for all observed energies, and b) for energies greater than 0.75 GeV.

The spectrum is shown binned in logarithmic energy units in Figure 5.17a, with an expanded view in Figure 5.17b. In this binning, the width, in bins, corresponding to the energy resolution is only slowly changing across the spectrum. The bin width corresponds to a 1.5% interval in energy.

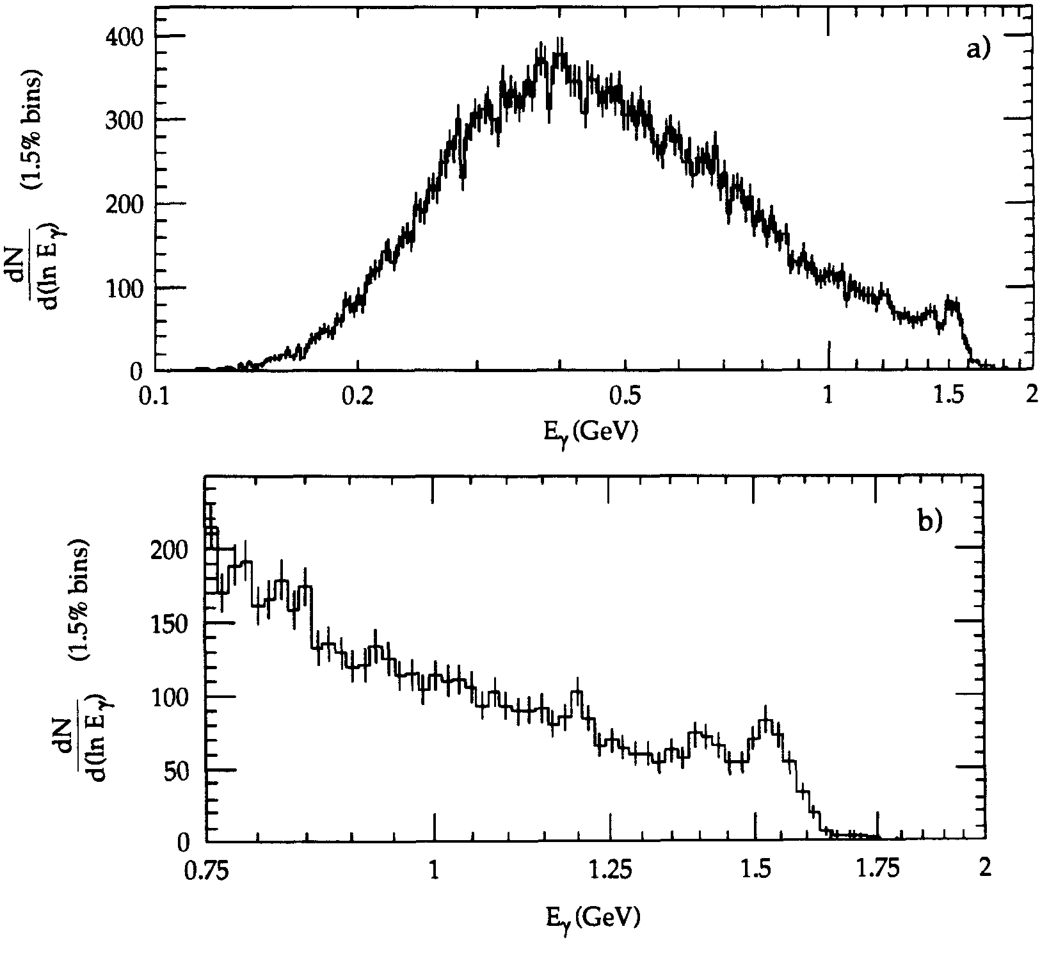

Figure 5.17 Observed energy spectrum of converted photons in 1.5% bins: a) the entire spectrum, and b) the spectrum for energies above 0.75 GeV.

The prominent peak at measured energies of 1.5 to 1.55 GeV arises from two QED processes. One is due to real conversions of high-energy photons, while the other is a background due to the reconstruction of spurious pairs.

1. $e^+e^- \to \gamma\gamma$.

   This reaction, where the two photons are radiated from an internal virtual electron line, has a large cross-section at SPEAR energies. The lowest order expression for the total cross-section for this process is:[53]

   $$\sigma^o_{e^+e^-\to\gamma\gamma} = \frac{2\pi\alpha^2}{s}\left(\ln\frac{s}{m_e^2} - 1\right),$$

   which evaluates to $\sim$ 220 nb at $s = m^2_{J/\psi}$. The photons are produced back-to-back, with the full beam energy. This process is normally not detectable by the Mark III apparatus, since the event trigger is not sensitive to events containing neutral tracks alone.

2. $e^+e^- \to \gamma e^+e^-$.

   A source of track pairs misidentified as photon conversions is the conventional final-state-radiative Bhabha reaction where a photon is emitted very close to the direction of one of the outgoing electrons. If the radiated photon converts in the detector structure, the conversion will occur very close to the trajectory of the parent electron. It is in this case possible to associate the parent with the conversion pair electron of opposite charge to the parent, forming a spurious pair of total energy very close to the beam energy.

The signatures of both of these processes are visible in the data. Events arising from process 1) may be selected by requiring that there be no charged tracks in the event other than the constituents of the photon conversion candidate. Figure 5.18 is a scatter plot of the conversion candidate energy for such events versus the energy measured in the electromagnetic calorimeter for the highest energy neutral shower in the event. A clear peak may be seen, associating large shower energies with pair energies in the 1.5 to 1.55 GeV region.

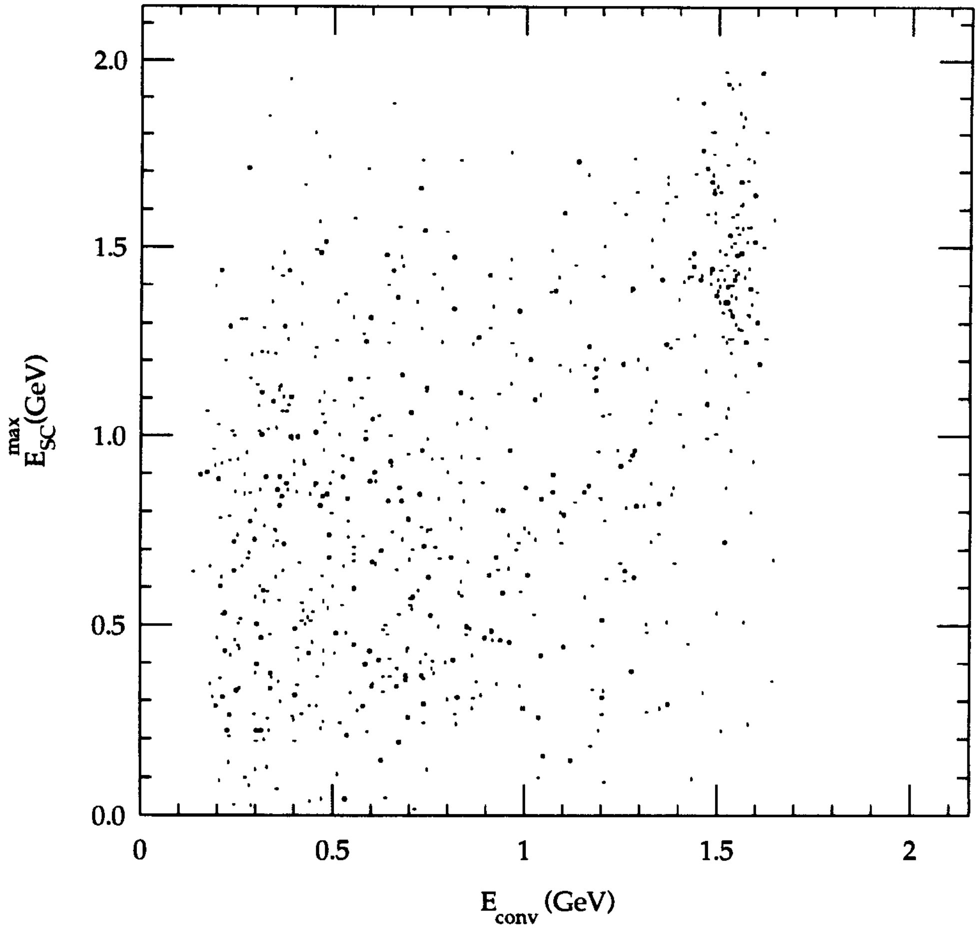

Figure 5.18 Scatter plot of the energy E_{conv} of photon conversion candidates versus the energy E_{SC}^{max} of the most energetic neutral shower in the event.

Events arising from process 2) may be identified by requiring that there be either three or four charged tracks in the event. As the radiated photons in this process are low in energy, it is very likely that, when they convert, one of the pair of produced electrons would fail to be detected due to insufficient transverse momentum. Figure 5.19 is a scatter plot of the conversion candidate energy for such events versus the momentum of the highest momentum charged particle not a member of the conversion candidate. The latter momentum would be expected to near that of the beam for the non-radiative electron. A clear peak may be seen, an association between conversion candidates near the beam energy and recoil tracks near the beam momentum.

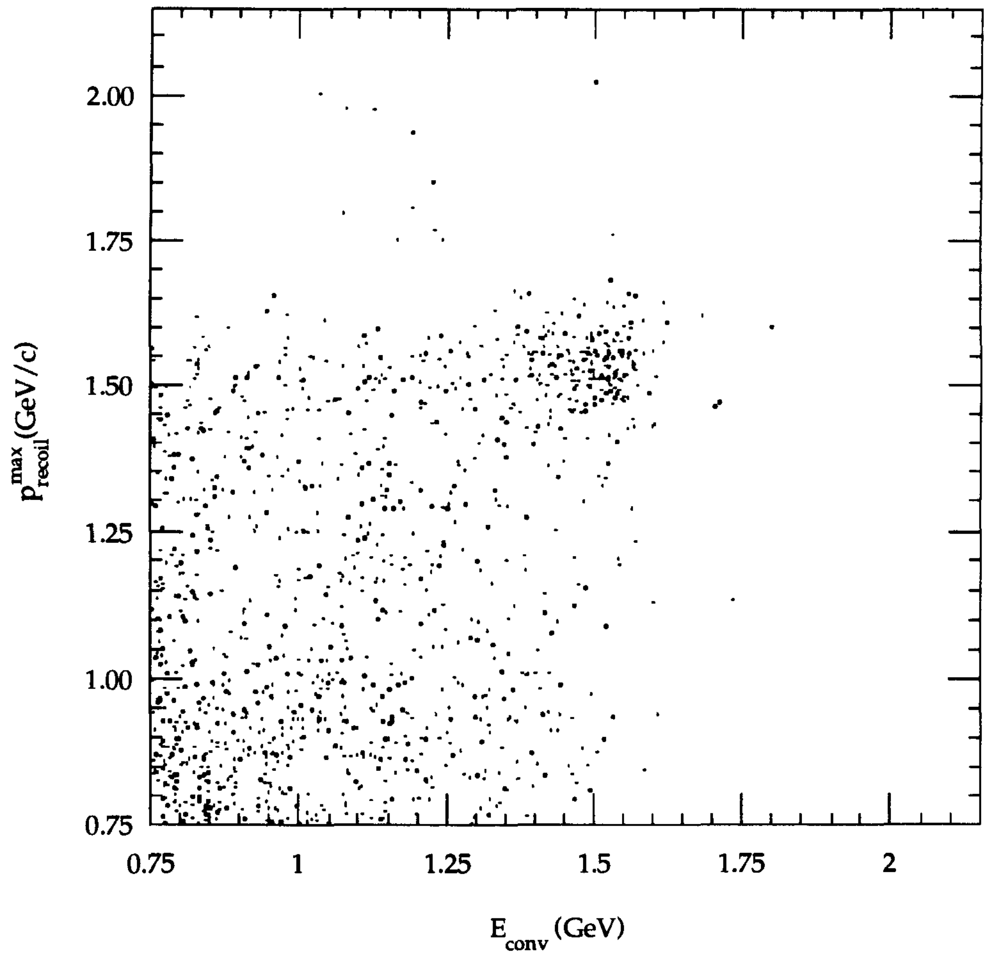

Figure 5.19 Scatter plot of the energy E_{conv} of photon conversion candidates versus the momentum p_{recoil}^{max} of the highest momentum charged particle not in the candidate pair.

Although it is possible to identify events as arising from these processes, this requires use of event information other than the parameters of the conversion candidate track pair itself. The subsequent analysis of the conversion energy spectrum is predicated on its being an inclusive analysis making minimal assumptions concerning the characteristics of the recoil against the e^+e^- pair. An attempt to remove events arising from the QED background might introduce such a recoil-dependent bias. We therefore choose to accept the presence of the background and simply avoid the energy region above 1.5 GeV in the subsequent analysis of the spectrum. An energy in this region corresponds to recoil masses less than or equal to that of the η meson.

Any other peak in this spectrum would be expected to reflect the presence of a large radiative branching fraction from J/ψ to a narrow resonance. The remainder of the spectrum appears to contain no such peaks of convincing statistical significance, although there are indications of structure near E_γ = 1.2 and 1.4 GeV. In the next chapter we proceed to quantify these assertions.

Chapter 6 Analysis of the Inclusive Photon Spectrum

Section 1 Overview

The final inclusive photon energy spectrum obtained from this analysis is shown in Figures 5.16 and 5.17, in the previous chapter. We limit further consideration of this spectrum to photon energies above 0.5 GeV, below which, as we have seen, the detection efficiency for converted photons begins to fall significantly.[1] The presence of a large two-body radiative decay mode $J/\psi \rightarrow \gamma + \mathrm{X}$, with X a narrow resonance, would be expected to manifest itself as a peak in the spectrum. As little statistically significant structure can be seen in the present data sample, we shall proceed to determine upper limits on the potential branching fractions to such two-body final states.

The energy of a photon produced in a two-body radiative decay is related to the mass of the recoiling state by:

$$E_\gamma = \frac{M_{J/\psi}}{2}\left(1 - \frac{M^2_{recoil}}{M^2_{J/\psi}}\right). \tag{6.21}$$

As a guide to interpretation of the results to follow, a conversion chart for photon energy, Feynman x (defined as $x_\gamma \equiv \frac{2E_\gamma}{M_{J/\psi}}$) and resonance mass is included as Figure 6.1. The masses and corresponding photon energies of a number of known and candidate resonances are marked and labeled.

We make the following assumption: that a large two-body decay mode will manifest itself as a narrow energy peak above a locally smooth background distribution.[2] It is

---

[1] The possibility of observing the charmonium transition $J/\psi \rightarrow \gamma\ \eta_c$ is completely excluded in this analysis. The detection efficiency for the 0.114 GeV photon produced in this decay to be observed as a converted pair is negligible.

[2] "Narrow" and "locally smooth" in this context are taken to mean that the width of the peak is small compared to the energy scales over which the slope of the underlying energy spectrum varies.

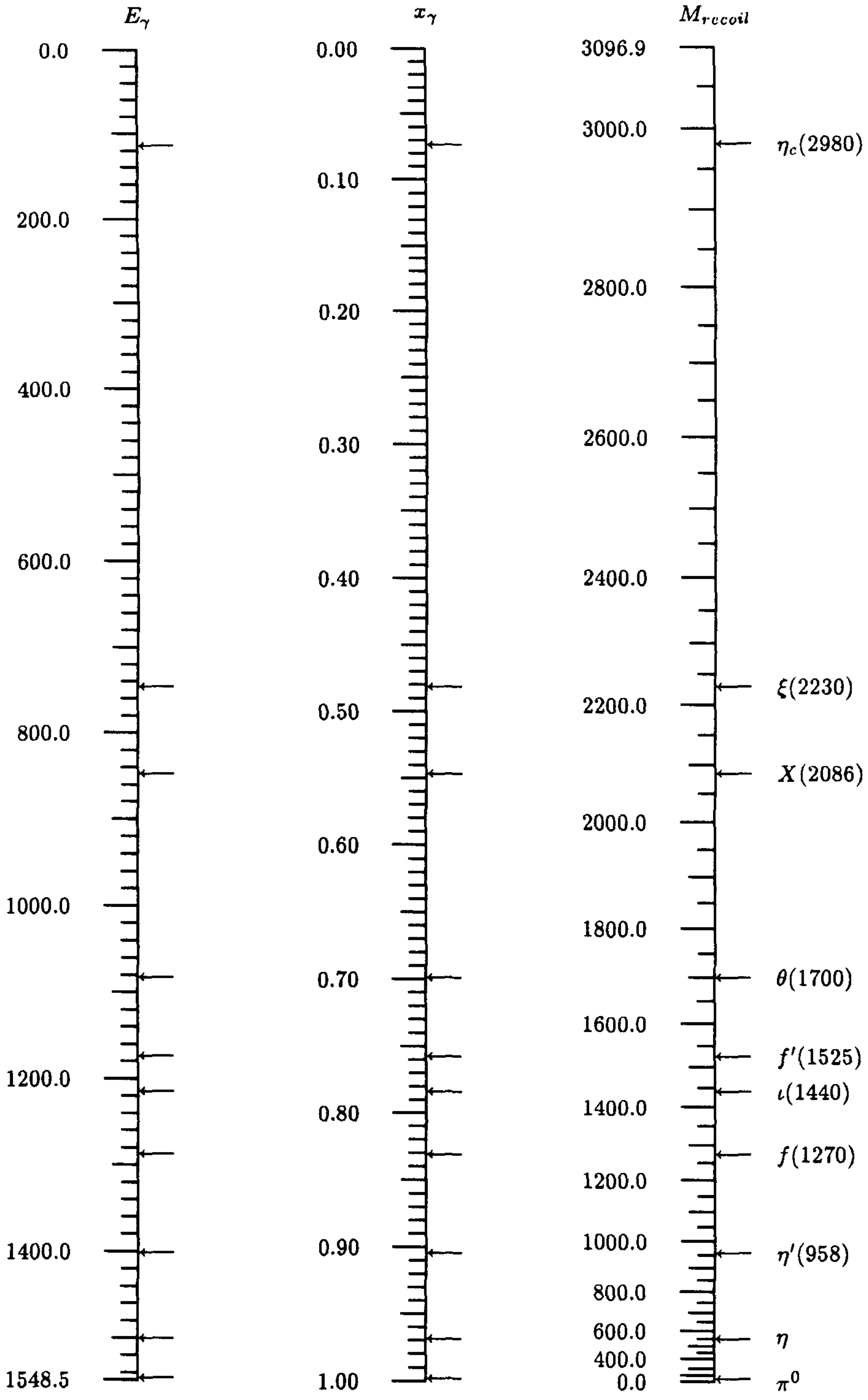

Figure 6.1 Chart showing the correspondence between photon energy, Feynman x, and resonance mass for two-body radiative decays $J/\psi \to \gamma + X$. Various known or suspected resonances are marked and labeled.

possible to imagine that, for a given decay mode, the photon energy spectrum resulting from the combination of all other radiative decays might have a peak or dip at the photon energy resulting from the decay of interest. In this case, our assumption would result in an incorrect estimate of the branching fraction for this decay. The presence of a dip would invalidate an upper limit determined under the assumption of a smooth underlying distribution.

In this analysis, we shall see that we are in any event sensitive only to branching fractions comparable to or larger than the largest previously observed for exclusive non-charmonium radiative decay modes. The presence of dips of comparable size in the background distribution seems unlikely, given the large number of individual decays combining to make up the spectrum, together with the photons arising from sources other than two-body radiative decays. A future attempt to measure the inclusive photon spectrum with higher efficiency or with a larger data sample would require additional consideration to be given to this issue.

The Mark III computer program BWGNEW[54] is used to perform binned maximum likelihood fits to the spectrum and to derive upper limits. Two categories of fits are performed. First, for each of four resonances previously observed in radiative J/ψ decays in exclusive final states, the spectrum is inspected for a peak with the line shape parameters predicted from the exclusive measurements, and upper limits are determined for the inclusive radiative branching fractions to these resonances. Then, the entire spectrum is inspected for statistically significant peaks: fits are performed at a series of test energies across the spectrum, for each of three nominal resonance widths, 0, 0.05, and 0.10 GeV/c^2, and the statistical significances of the fits are shown as a function of energy.

It should be noted that, in the case of a two-body radiative decay, it is the *mass* of the resonance that is distributed according to a Breit-Wigner function. The resulting

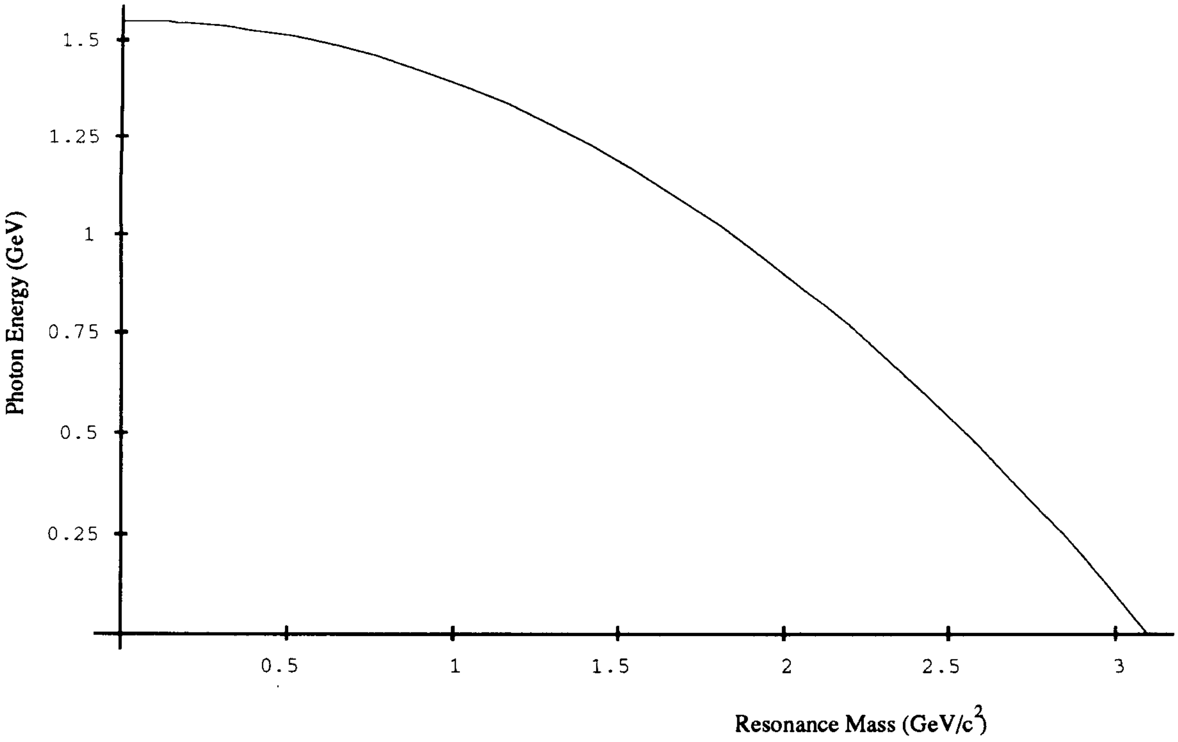

Figure 6.2 Photon energy-resonance mass relation for two-body J/ψ radiative decays.

photon energy is related to the mass according to equation 6.21, and it is to this energy that the detector energy resolution is applied. The energy-mass relationship is exhibited in Figure 6.2. Since the transformation is not linear, the true photon energies are not in fact distributed according to a Breit-Wigner function. Using a Breit-Wigner function in the fit to the energy spectrum, therefore, is an approximation. This approximation corresponds to the use of an "effective width" in energy space, Γ^*, obtained from the true Breit-Wigner width, Γ, according to

$$\Gamma^* = \left|\frac{dE_\gamma}{dM_{res}}\right|\Gamma = \frac{M_{res}}{M_{J/\psi}}\Gamma.$$

Qualitatively, this effect may be considered unimportant as long as the variation in the effective width across the resonance is a small relative change. This can be expressed as:

$$\frac{|\Gamma^*(M_{res}+\Gamma) - \Gamma^*(M_{res}-\Gamma)|}{\Gamma^*(M_{res})} \ll 1, \text{ or } \frac{2\Gamma}{M_{res}} \ll 1.$$

This requirement is well satisfied for all the resonances of interest. Nonetheless, for a sufficiently large data sample, even a small distortion of the fit function might have a significant effect on a goodness-of-fit criterion. Therefore, the effect of this distortion on the results of this analysis has been investigated using a Monte Carlo test. This test discovered no detectable effect of the distortion for the sample sizes relevant to this analysis.

Section 2 Upper Limits for Known States

We begin with the analysis of four specific final states with known properties: $\eta'(958)$, ι/X(1450), $\theta/f_0(1710)$, and X(2230) (the "ξ"). In each case, we perform fits to the spectrum to extract candidate signals, if possible, and set upper limits on the inclusive branching fractions.

The function used for these binned maximum likelihood fits is the expected line shape superposed on a smooth background function in a surrounding interval, just as above. The line shape used is a nonrelativistic Breit-Wigner distribution convoluted with a Gaussian resolution function. In each fit, the centroid and the shape parameter(s) of the signal function are fixed to their expected values, as determined from previous experimental results and by Monte Carlo simulation. The standard background function used is a quadratic polynomial. The size of the signal function, and the size and shape of the background function, are permitted to vary in the fit.

Upper limits are determined using the following procedure: first, the best fit to the combined signal and background function is obtained, allowing the signal size and the coefficients of the polynomial background to vary, while constraining the integral of the fit function to the number of observed events in the fit interval. The relative size of the fit function is then varied through a series of test points in a seven standard deviation interval (never allowing the signal fraction to become negative) around the best fit value. At each point, the fit is repeated with its parameters allowed to vary, maintaining the overall normalization. The likelihood profile obtained from this procedure is then integrated to obtain a confidence level profile. The 90% C.L. point on this curve is then returned as the upper limit.

The fits yield numbers of observed events. In order to convert these into branching fractions, the event counts must be corrected for detection efficiency and divided by the number of J/ψ events in the data sample used in this analysis,

$$N_{J/\psi} = (4.83 \pm 0.37) \times 10^6.$$

The detection efficiency is determined from a Monte Carlo simulation specific to the final state of interest.

The resulting branching ratios are further adjusted to take into account the identifiable sources of systematic uncertainty in the analysis: the determination of the detection efficiency, the selection of the signal parameters, background function, and fit interval, and the normalization to $N_{J/\psi}$.

The systematic errors reflect lack of knowledge rather than statistical imprecision, and so we cannot assign any *a priori* probability distribution function (p.d.f.) to them in order to perform a rigorous calculation of the 90% C.L. upper limit including their effects. Nonetheless, we must provide at least a heuristic evaluation of their effects. We therefore use what has become a commonly accepted procedure: we add linearly the contributions from the various sources, and then add 1.28 times the total,[3] as though the sum of the errors were distributed according to a Gaussian p.d.f., to the upper limits obtained above.

$\eta'(958)$

Alone among these states, the $\eta'(958)$ does appear to manifest itself as a clear peak in the inclusive photon spectrum, at the expected 1.400 GeV energy, although not with

---

[3] Reflecting the fact that 90% of the area of a Gaussian is found below a point 1.28σ above its mean.

the statistical significance that would be required for the observation of a new state. The intrinsic width of the $\eta'(958)$ is $(2.08 \pm 0.21) \times 10^{-4}$ GeV$/c^2$ — negligible compared to the converted photon energy resolution. We therefore perform a fit to the spectrum using only a single Gaussian resolution function above the standard quadratic background. The central energy is fixed to its expected value, and the resolution to that determined by Monte Carlo analysis for this specific final state. Only the size of the signal and the polynomial coefficients of the background are permitted to vary in the fit. The fit is performed over the interval 1.25–1.46 GeV, which is somewhat abbreviated on the high side in order to avoid the peaking of the QED background. The fit, with a χ^2 per degree of freedom of 0.91, is displayed in Figure 6.3. The fit finds 116 ± 50 events in the signal line shape, after correction for the tail of the Gaussian outside the fit interval. The statistical significance of the signal, obtained by comparing the likelihood for the fit with that for a fit with the signal function removed, is 2.30 standard deviations.

The efficiency is determined by Monte Carlo analysis to be $(3.9 \pm 0.5) \times 10^{-3}$, significantly less than the value of $(5.1 \pm 0.5) \times 10^{-3}$ determined in the previous chapter. This is due to the additional requirement here imposed that the measured photon energies fall into the Gaussian resolution function. The converted photon energy resolution distribution has extended non-Gaussian tails. In the fit to the energy spectrum in the data, photons in these tails will be absorbed into the polynomial background, and so must not be counted in the efficiency. The uncertainty in the evaluation of the efficiency resulting from the application of this requirement has been added in quadrature with the uncertainty in the converted photon selection procedure.

After correction for efficiency and normalization to the J/ψ flux, the resulting value for the inclusive branching ratio is

$$B(J/\psi \to \gamma\eta'(958)) = (6.1 \pm 2.7) \times 10^{-3}.$$

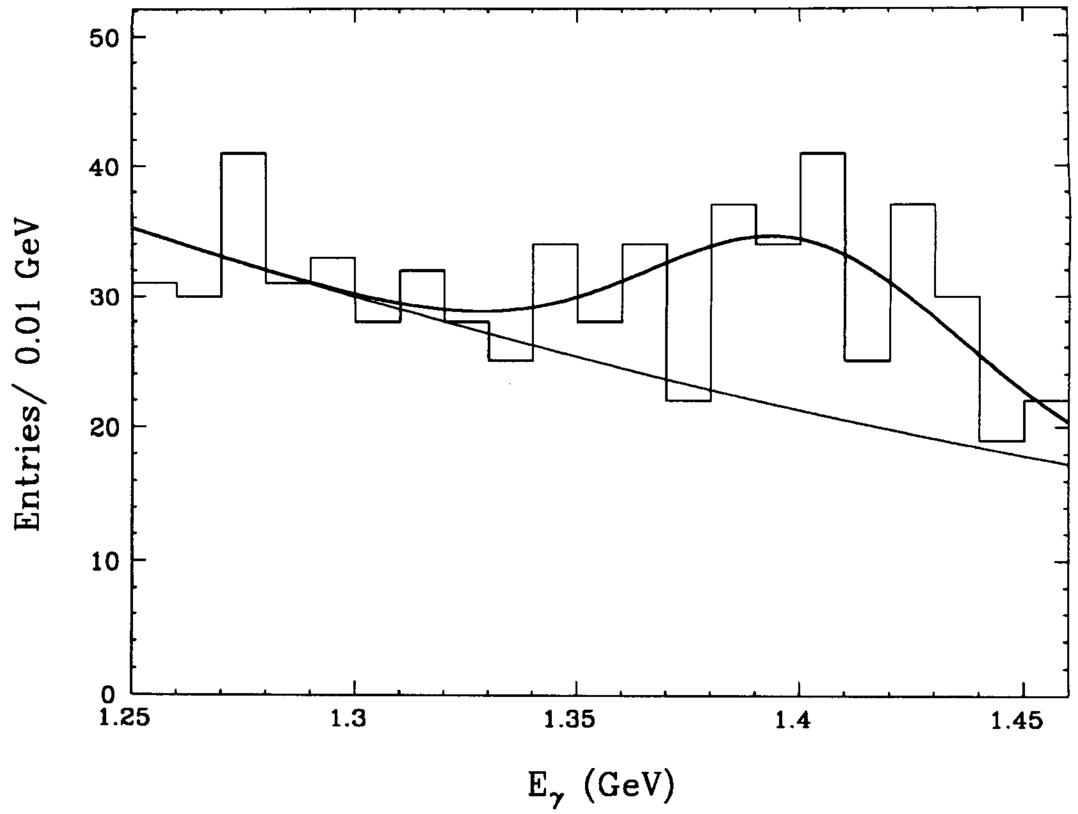

Figure 6.3 Result of the fit to the observed spectrum using the parameters expected for the line shape at 1.400 GeV/c^2 resulting from the decay $J/\psi \rightarrow \gamma\ \eta'(958)$.

The size of the signal is very sensitive to the choice of the upper boundary of the fit interval. As a further check on this, we perform a modified fit over an interval extending to 1.64 GeV, including an ad-hoc Gaussian distribution in the fit function as a representation of the QED background. Allowing the centroid and width of this Gaussian to vary, we obtain the result shown in Figure 6.4. The fit has a χ^2 per degree of freedom of 1.09. The $\eta'(958)$ signal in this fit contains 136 ± 49 events, corresponding to the branching ratio

$$B(J/\psi \rightarrow \gamma\eta'(958)) = (7.2 \pm 2.6) \times 10^{-3}.$$

The statistical significance of the $\eta'(958)$ signal in the fit is 2.18 standard deviations.

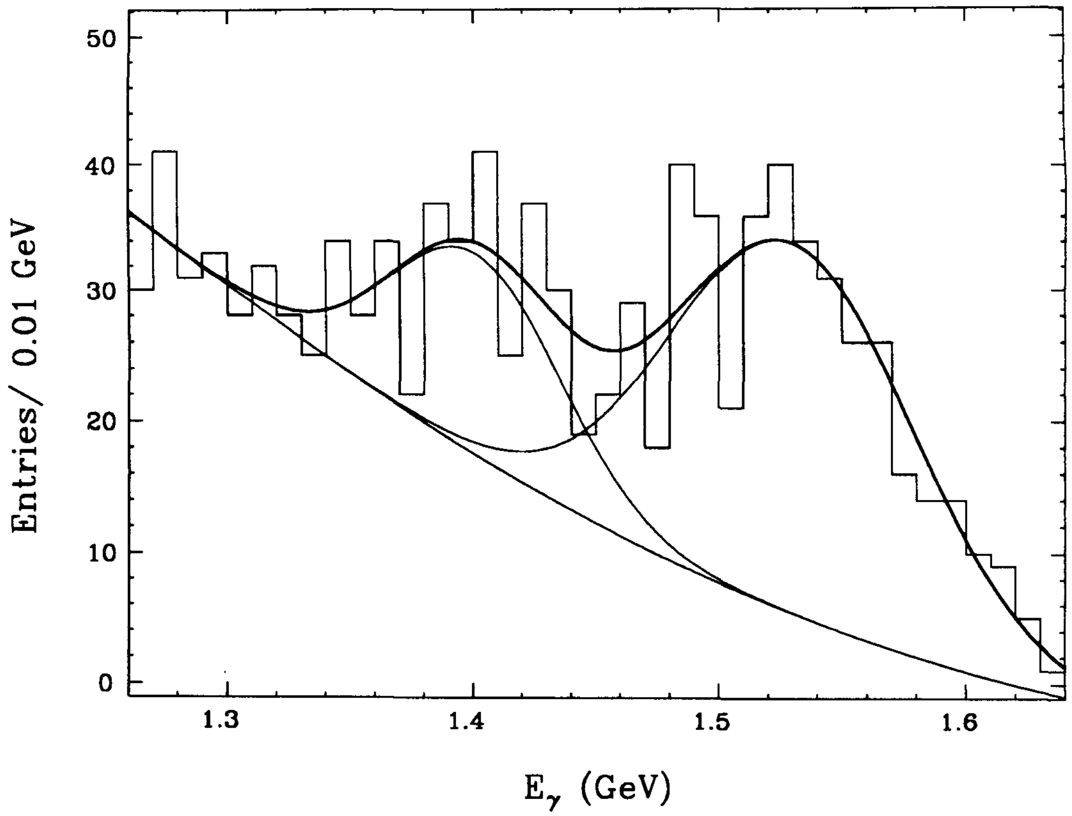

Figure 6.4 Results of the fit to the observed spectrum using the parameters expected for the line shape at 1.400 GeV resulting from the decay $J/\psi \rightarrow \gamma\ \eta'(958)$, and including a term in the fit to represent the QED background at 1.5–1.55 GeV.

In light of the somewhat reduced goodness of fit and the lesser statistical significance of the latter result, we choose the branching fraction from the initial fit over the truncated interval as our final result. The systematic uncertainty in the measurement is determined by adding in quadrature the contributions from the determination of the efficiency, 13%, and the overall normalization, 7.6%, together with 16% from the uncertainty introduced by the choice of fit interval, energy resolution, and background function. The final result is, therefore,

$$\boxed{B(J/\psi \rightarrow \gamma\eta'(958)) = (6.1 \pm 2.7 \pm 1.3) \times 10^{-3}.}$$

Within the large statistical and systematic uncertainties, this is in agreement with the accepted value[21] of $(4.2 \pm 0.4) \times 10^{-3}$. This result provides some confirmation of the correctness of the Monte Carlo determination of the photon conversion detection efficiency, and of the analysis procedure in general.

We also determine, for consistency with the remainder of this analysis, and in view of the limited statistical significance of the measurement, an upper limit for this signal. The result, at the 90% C.L., is 181 events, for an upper limit on the branching fraction of 9.6×10^{-3}. The inclusion of the effects of systematic errors, following the procedure outlined above, raises this limit to

$$\boxed{B(J/\psi \to \gamma\eta'(958)) < 12.3 \times 10^{-3} \text{ at the 90\% C.L..}}$$

$\iota/X(1450)$

The history of the observation of structure in the 1.45 GeV/c^2 mass region in J/ψ radiative decays is summarized in Section 4. Structure has been observed in three final states: $\gamma + K\bar{K}\pi$, $\gamma + \eta\pi\pi$, and $\gamma + \gamma\rho$. Recent analyses indicate that the final state mass peaks observed result from the interplay of three underlying resonances. With the limited statistics available to this analysis, however, we are unable to resolve any underlying structure. We can only examine the question of whether there is a large total radiative branching fraction to a combination of states clustered in the 1.45 GeV/c^2 mass region. A comparison of such a result with the known branching fractions might yield information on the possible presence of hitherto unobserved structure in this region in other exclusive final states.

The photon recoil energies corresponding to masses in the range 1.4–1.5 GeV/c^2 are approximately 1.23–1.19 GeV. A modest clustering of events is visible in this region of the inclusive photon spectrum. In order to perform a fit to the spectrum to obtain a measurement of and an upper limit on the size of this signal, we must select an appropriate energy distribution to parametrize the signal. This distribution will then, as above, be convoluted with a Gaussian resolution function and superposed on a quadratic background distribution.

The natural choice for the signal shape might be a superposition of Breit-Wigner terms for each of the three resonance observed in the 1.45 GeV region. However, since the various branching fractions $B(X \to K\bar{K}\pi)$ are not known, the relative contributions of the three underlying resonances to the process $J/\psi \to \gamma + X(1400\text{-}1500)$ cannot be fixed in the fit. When a fit is performed using three Breit-Wigner distributions, with centroids and widths fixed to their expected values,[4] but with their relative sizes permitted to vary, the limited statistics available appear to preclude any attempt to discriminate between the three terms. Almost invariably, the broadest of the three, corresponding to the $J^{PC} = 0^{-+}$ K^*K state at 1.490 GeV/c^2, dominates the fit, and the other two signal sizes are returned as zero.[5] However, the three signal sizes are highly correlated, with error estimates allowing almost arbitrary readjustment of the relative branching fractions.

As our only concern is the determination of the total radiative branching fraction to the aggregate of resonances in this mass region, we therefore choose to parametrize the signal with a single Breit-Wigner distribution selected to fit the entire structure observed in $\gamma + K\bar{K}\pi$, the final state dominating the known exclusive decay modes. Although this is admittedly a poor match to the high statistics $\gamma + K\bar{K}\pi$ data, it appears to be a necessary simplification. The resonance parameters chosen are those from the earlier Mark III analysis of the $K\bar{K}\pi$ structure as a single state:[24] $M_X = 1.456$ GeV/c^2 and $\Gamma_X = 0.095$

---

[4] The expected values are calculated from the masses and widths for the three states observed in the Mark III analysis of the $K\bar{K}\pi$ final state.[25]

[5] More precisely, the other two signal sizes resulting from the fit are consistent with zero to within the calculational roundoff of the fitting program.

GeV/c^2, leading to line shape parameters $E_{\gamma,X} = 1.206$ GeV and $\Gamma_{eff} = 0.045$ GeV. Variations on this assumption will be used to determine the systematic errors on the result.

The results of a fit to the spectrum, fixing the above parameters, using a Gaussian photon energy resolution of 0.026 GeV, as determined in the Monte Carlo simulation, and allowing the signal size and background parameters to vary, are shown in Figure 6.5. The fit finds 99 ± 79 events in the signal region.

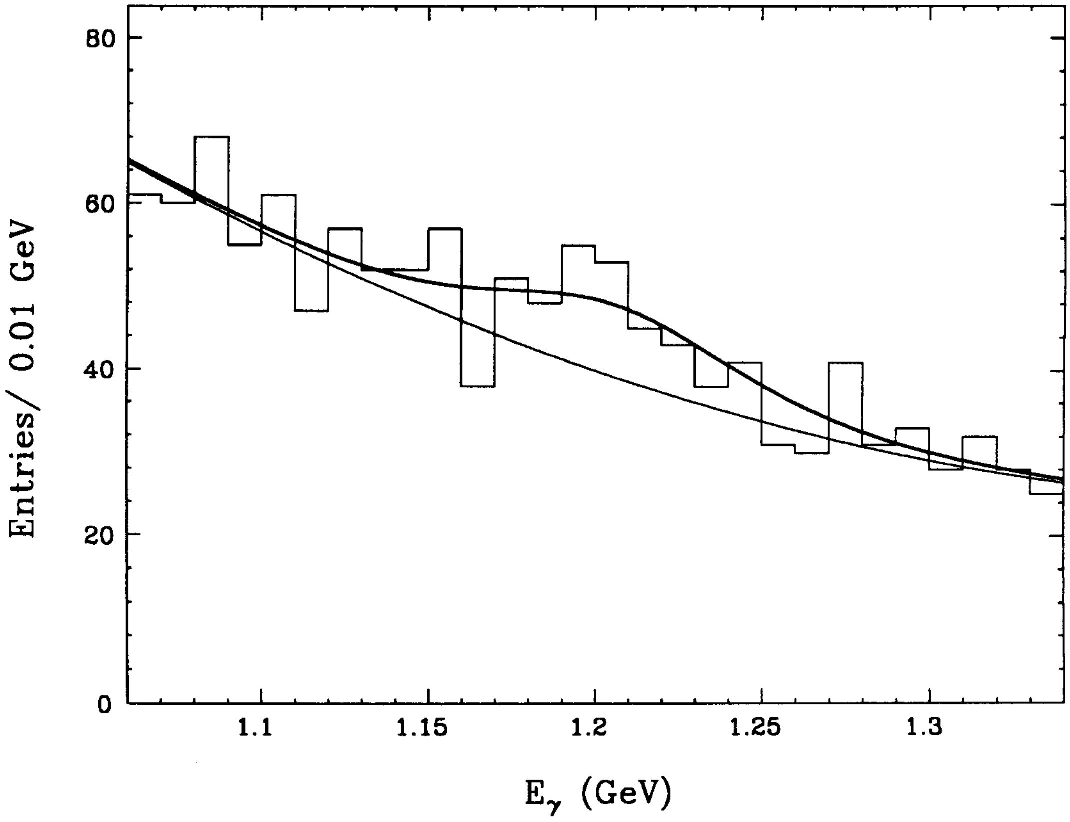

Figure 6.5 Fit to the inclusive photon energy spectrum in the $\iota/X(1450)$ mass range, with parameters as described in the text.

The efficiency for detecting the radiative photon in this final state was determined by Monte Carlo simulation to be $(4.3 \pm 0.6) \times 10^{-3}$. The inclusive branching fraction obtained after normalization and correction for efficiency is

$$B(J/\psi \rightarrow \gamma\ \iota/X(1450)) = (4.8 \pm 3.8) \times 10^{-3}.$$

As is apparent by inspection of the energy spectrum, this measurement is of limited statistical significance — 1.2 standard deviations. We therefore proceed to set an upper limit on the inclusive branching fraction. The result of the maximum likelihood analysis is an upper limit of 210 events at the 90% C.L. Correcting for efficiency and dividing by $N_{J/\psi}$, we obtain the result

$$B(J/\psi \rightarrow \gamma\ \iota/X(1450)) < 10.1 \times 10^{-3}, \text{ at the 90\% C.L.}$$

for the resonance parameters assumed above. Varying the mass over a range of ±0.020 GeV/c^2, and the width over a range of ±0.025 GeV/c^2, the maximum value obtained for the upper limit is 12.2×10^{-3}. Using this value, and adding contributions to the systematic uncertainty of 15% from the determination of the efficiency, and 7.6% from the overall normalization, we obtain the final result:

$$\boxed{B(J/\psi \rightarrow \gamma\ \iota/X(1450)) < 14.8 \times 10^{-3}.}$$

Figure 6.6 shows a signal size corresponding to this upper limit superposed on the background function obtained from the best fit to the spectrum.

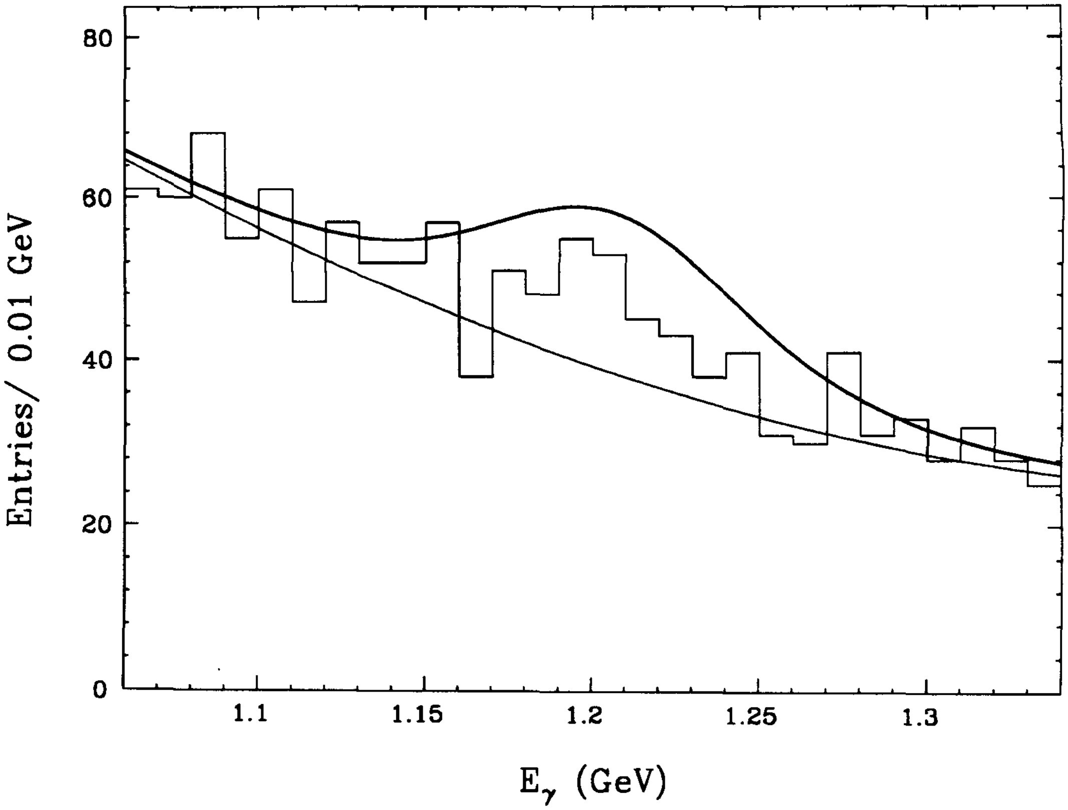

Figure 6.6 Signal shape in the inclusive photon energy spectrum corresponding to the upper limit obtained for $B(J/\psi \rightarrow \gamma + \iota/X(1450))$.

$f_0(1710)$

The history of the state now known as $f_0(1710)$ is summarized in Section 5. The parameters of the $J^P = 0^+$ state seen by the Mark III experiment[30, 55] in the exclusive final states $J/\psi \rightarrow \gamma K^+K^-$ and $J/\psi \rightarrow \gamma K_S^o K_S^o$ are

$$M_{f_0(1710)} = 1.710 \pm 0.020 \text{ GeV}/c^2$$

$$\Gamma_{f_0(1710)} = 0.186 \pm 0.030 \text{ GeV}/c^2$$

$$B(J/\psi \rightarrow \gamma f_0(1710)) \cdot B\big(f_0(1710) \rightarrow K\bar{K}\big) = (6.47 \pm 1.14 \pm 0.84) \times 10^{-4},$$

where the contribution from the unobserved $K_L^o K_L^o$ decay mode has been computed using $CP(f_0(1710)) = +1$, as required by the production mechanism, and assuming the

$f_0(1710)$ is an isoscalar state. A structure with similar parameters seen by Mark III in the final state $J/\psi \rightarrow \gamma\pi^+\pi^-$ is assumed to arise from the $\pi\pi$ decay of the same resonance. The measured product branching fraction is

$$B(J/\psi \rightarrow \gamma f_0(1710)) \cdot B(f_0(1710) \rightarrow \pi\pi) = (1.94 \pm 0.60 \pm 0.25) \times 10^{-4},$$

where the $\pi^o\pi^o$ mode, unobserved in the Mark III analysis, has been taken into account by assuming the $f_0(1710)$ is an isoscalar state.

No signal is visible in the inclusive spectrum at the expected photon energy of 1.076 GeV/c^2 for this two-body process. We determine an upper limit on the signal size that can be accommodated by the data, and calculate an upper limit on the inclusive branching fraction for $J/\psi \rightarrow \gamma f_0(1710)$.

The spectrum is fit with a single Breit-Wigner distribution, convoluted with a Gaussian resolution function, over a quadratic background. The centroid of the signal function is set to the expected photon energy. The Breit-Wigner effective width, Γ^*, is set to 0.103 GeV, the result of scaling the central value of Γ, 0.186 GeV/c^2, by the slope of the resonance mass-photon energy relation at this energy. The Gaussian resolution is set to 0.027 GeV, as determined from the Monte Carlo analysis. The efficiency obtained from this analysis is $(4.8 \pm 0.5) \times 10^{-3}$. The upper limit obtained, at the 90% C.L., is $B(J/\psi \rightarrow \gamma f_0(1710)) < 7.7 \times 10^{-3}$.

In order to determine the systematic uncertainty in this limit due to the choices of the conditions of the fit, the signal and background shape parameters were allowed to vary within the ranges allowed by the experimental and Monte Carlo uncertainties. Furthermore, a fit was performed including a contribution from the candidate $J/\psi \rightarrow \gamma + \iota/X(1450)$ signal at $E_\gamma = 1.2$ GeV. The inclusion of this term depresses the background in the fit, allowing a larger contribution in the $f_0(1710)$ region. The upper limit obtained, taking these variations in fit conditions into account, is

$$B(J/\psi \to \gamma f_0(1710)) < 16.5 \times 10^{-3}.$$

The remaining contributions to the systematic uncertainty for this final state are 10% from the determination of the efficiency and 7.6% from the overall normalization. Applying these, as above, the final upper limit for the inclusive radiative branching fraction to the $f_0(1710)$ is

$$\boxed{B(J/\psi \to \gamma f_0(1710)) < 19.2 \times 10^{-3}.}$$

The size of a signal with this magnitude is shown in Figure 6.7, superposed on the best fit to the spectrum, including a contribution from $J/\psi \to \gamma + \iota/X(1450)$.

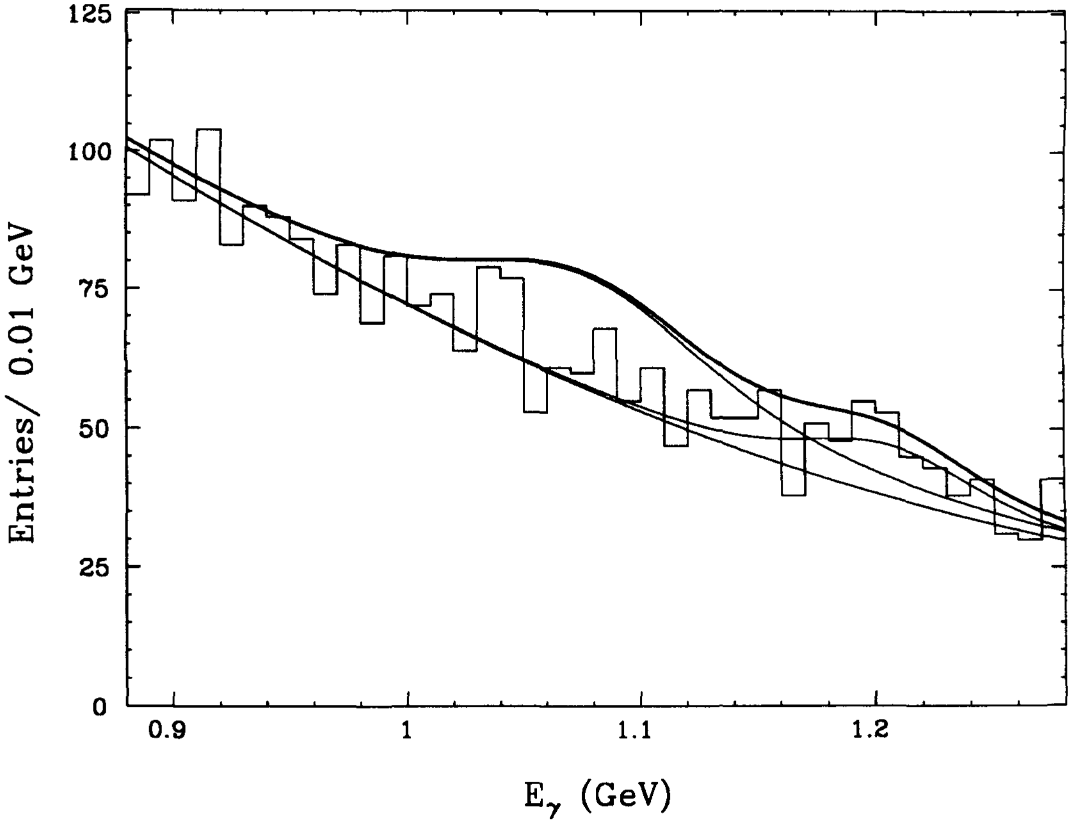

Figure 6.7 Graph of the line shape of a hypothetical signal for $J/\psi \to \gamma\, f_0(1710)$, with branching fraction equal to the upper limit determined in this analysis.

$X(2230)$

A state identified as X(2230), formerly known as the $\xi(2230)$, has been observed by the Mark III experiment[56] in the exclusive final states $J/\psi \rightarrow \gamma K^+K^-$ and $J/\psi \rightarrow \gamma K^o_S K^o_S$ with product branching fractions

$$B(J/\psi \rightarrow \gamma X(2230)) \cdot B\big(X(2230) \rightarrow K^+K^-\big) = \big(4.2^{+1.7}_{-1.4} \pm 0.8\big) \times 10^{-5}$$

and

$$B(J/\psi \rightarrow \gamma X(2230)) \cdot B(X(2230) \rightarrow K^o_S K^o_S) = \big(3.1^{+1.6}_{-1.3} \pm 0.7\big) \times 10^{-5},$$

a mass of 2.231 ± 0.005 ± 0.015 GeV/c^2, and a width in the range 0–0.050 GeV/c^2. The existence of this state is not firmly established, as it has not been seen by the DM2 experiment in a somewhat larger sample of J/ψ decays than was available to Mark III. It is therefore of interest to search for evidence of its existence in the inclusive photon spectrum. No exclusive final states other than $K\bar{K}$ have been observed to date, so, including an assumed branching fraction for $J/\psi \rightarrow \gamma K^o_L K^o_L$ equal to that for $J/\psi \rightarrow \gamma K^o_S K^o_S$, the total known branching fraction for $J/\psi \rightarrow \gamma X(2230)$ is approximately 10^{-4}. Since no signal is visible in the inclusive spectrum at the expected photon energy of 0.746 GeV/c^2 for this two-body process, we proceed to set an upper limit.

The spectrum is once again fit with a convoluted Breit-Wigner-Gaussian function over a quadratic background. The centroid of the signal function is set to the expected photon energy. The Breit-Wigner effective width, Γ^*, is set to 0.018 GeV, the result of scaling the central value of Γ, 0.025 GeV/c^2, by the slope of the resonance mass-photon energy curve at this energy. The Gaussian resolution is set to 0.014 GeV, as determined from the Monte Carlo analysis. The efficiency obtained from this analysis is $(4.5 \pm 0.3) \times 10^{-3}$. Taking variations of the fitting procedure — and of the resonance parameters within their experimental limits — into account, an upper limit of 144 observed events is obtained, at the 90% C.L., yielding a limit on the radiative decay branching fraction of

$$B(J/\psi \to \gamma X(2230)) < 6.6 \times 10^{-3}.$$

The remaining contributions to the systematic uncertainty for this measurement are 7% from the determination of the efficiency and 7.6% from the overall normalization. Applying these, as above, the final upper limit for the inclusive radiative branching fraction to the X(2230) is

$$\boxed{B(J/\psi \to \gamma X(2230)) < 7.5 \times 10^{-3}.}$$

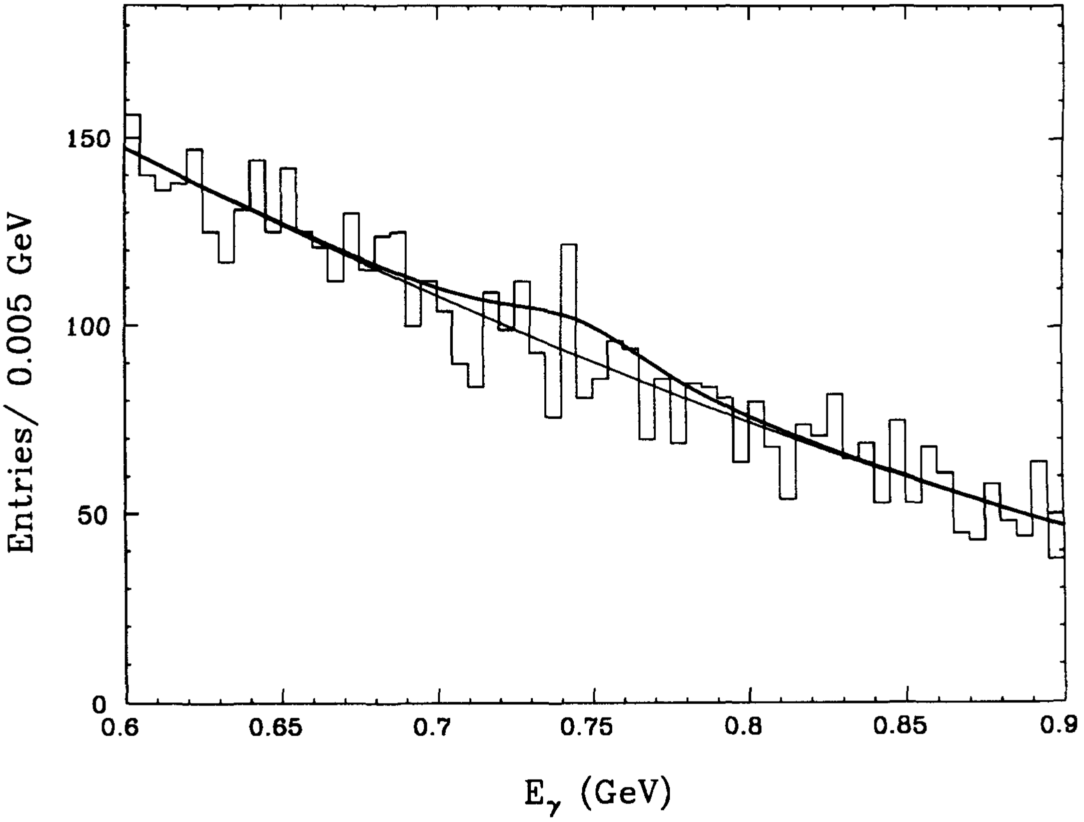

Figure 6.8 Graph of the line shape of a hypothetical signal for $J/\psi \to \gamma$ X(2230), with branching fraction equal to the upper limit determined in this analysis.

The size of a signal with this magnitude is shown in Figure 6.8, superposed on the best fit to the spectrum.

Summary

The upper limits derived for the four states of interest are summarized in Table 6.1.

Table 6.1 Summary of the upper limits, at the 90% C.L., on various inclusive radiative branching fractions, as derived from the observed photon energy spectrum. The rightmost column includes the effects of systematic errors.

Resonance	Observed Events	Statistical Upper Limit	Upper Limit, $B(J/\psi \to \gamma X)$
$\eta'(958)$	< 181	$< 9.6 \times 10^{-3}$	$< 12.3 \times 10^{-3}$
$\iota/X(1450)$	< 210	$< 10.1 \times 10^{-3}$	$< 14.8 \times 10^{-3}$
$f_0(1710)$	< 383	$< 16.5 \times 10^{-3}$	$< 19.2 \times 10^{-3}$
$X(2230)$	< 144	$< 6.6 \times 10^{-3}$	$< 7.5 \times 10^{-3}$

Section 3 Significance Tests for Nominal-Width Resonances

Apart from the candidate peaks associated with the processes $J/\psi \to \gamma + \eta'$ and $J/\psi \to \gamma + \iota/X(1450)$, no further meaningful structure is apparent in the inclusive spectrum. In order to quantify this statement, a series of fits to peaks of standardized parameters is repeated across the spectrum, resulting in a tabulation of the statistical significance of any potential structure as a function of energy. This procedure is performed for peaks corresponding to resonances of three hypothetical widths: 0, 0.050, and 0.100 GeV/c^2. Each series of fits is performed with the true width, in M_{res} space, held constant. The width of the fit function in energy space, $\Gamma_{eff}(E_\gamma)$, therefore, varies across the spectrum.

The Breit-Wigner function in the fit is convoluted with a Gaussian of width fixed to the converted photon energy resolution, $\sigma_{E_\gamma}(E_\gamma)$, varying with energy as determined by the Monte Carlo procedure described in the previous chapter and displayed in Figure 5.15.

In addition to the signal fit function, each fit includes a quadratic polynomial representing the assumed smooth underlying distribution. For each candidate signal photon energy, the fit is performed over an interval of energies surrounding the centroid that is sufficiently broad that the parameters of the quadratic are well-determined. The size of this interval depends on the assumed width of the candidate signal.

The spacing between test points is chosen to be one-third of the predicted energy resolution, $\sigma_{E_\gamma}(E_\gamma)$, at the test energy. The fits are carried out under these conditions for test energies in the range from 0.50 GeV to 1.40 GeV. The QED background previously discussed dominates above the latter energy and invalidates the essential assumption of a smooth underlying spectrum. The fit intervals at the highest energies are constrained to end at 1.46 GeV to avoid bias from this source. Below 0.50 GeV, where the efficiency begins to fall off rapidly, the presumption of smoothness is again invalid.

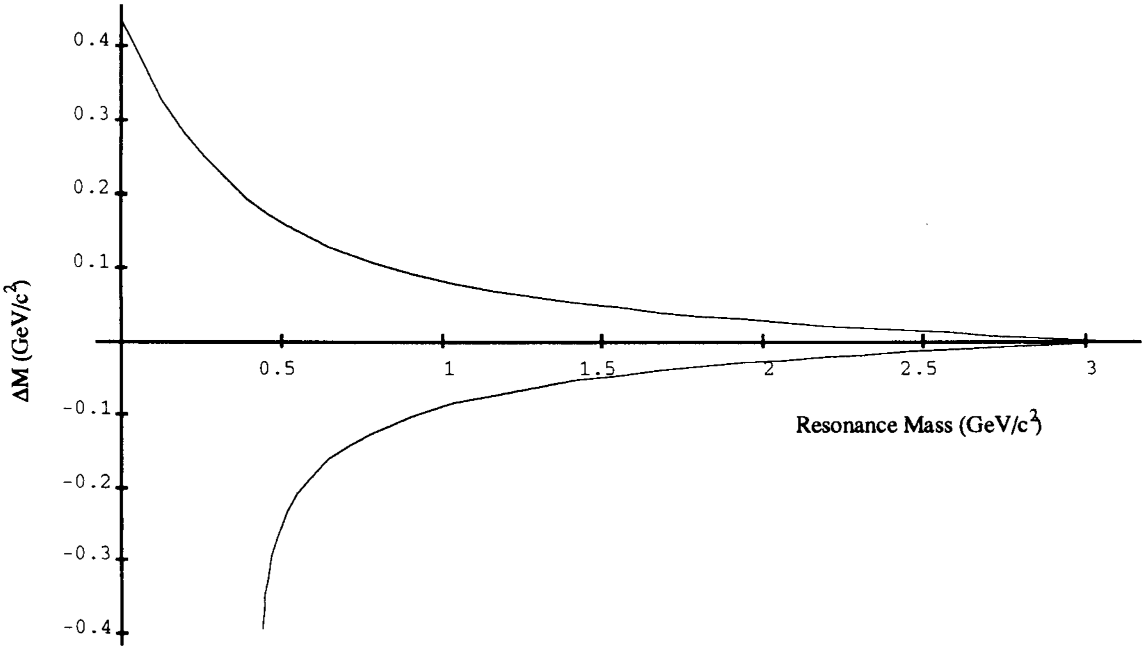

Figure 6.9 Ideograph of resonance mass interval corresponding to a ±2% resolution interval on the photon energy in two-body J/ψ radiative decays.

While the energy range over which the fits are performed corresponds to the range of resonance masses 0.96–2.55 GeV/c^2, it should be noted that the photon energy is quite insensitive to the resonance mass for small masses, and that the effective mass resolution obtained from these fits is therefore poor in that region. This is exhibited in Figure 6.9, which displays the interval in resonance mass corresponding to a ±2% variation in photon energy, as a function of resonance mass.

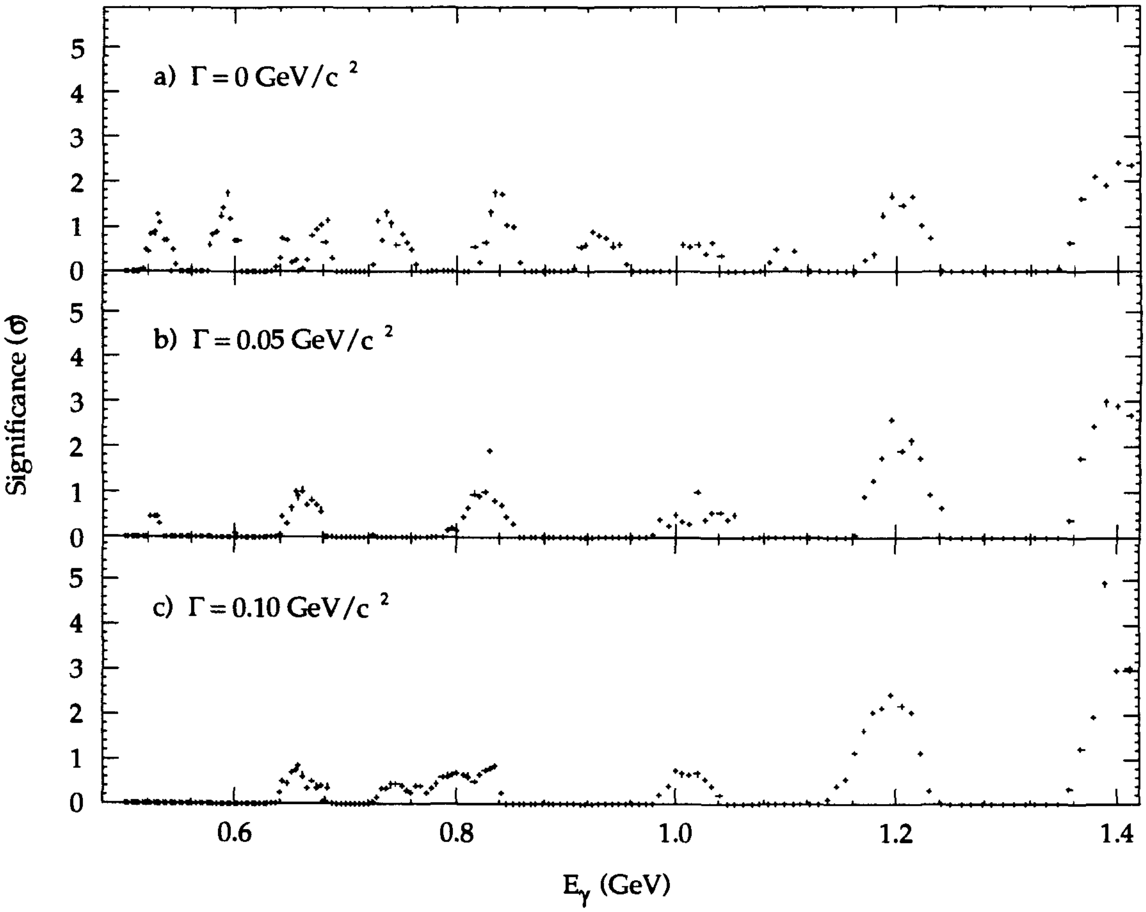

Figure 6.10 Statistical significances of fits to the inclusive photon spectrum using the line shapes expected for $B(J/\psi \rightarrow \gamma + X)$, for a) $\Gamma_X = 0$, b) $\Gamma_X = 0.050$, and c) $\Gamma_X = 0.100$ GeV/c^2.

The statistical significance of the signal amplitude in each fit is computed as the ratio of the signal size to the fitted uncertainty in the signal size. Figures 6.10a, b, and c display the resulting values, in standard deviations, as a function of photon energy for the three nominal values of Γ_{res}: 0, 0.05, and 0.10 GeV/c^2, respectively.

Inspection of the figure shows that the spectrum contains no structures of comparable statistical significance to those at 1.2 and 1.4 GeV discussed above, and none at all with the significance that would be required for the meaningful observation of a new effect.

Chapter 7 Conclusions

We have performed an analysis of the inclusive photon spectrum arising from J/ψ decays. By searching for converted photons we have achieved good energy resolution at the cost of an approximately 0.5% detection efficiency for high-energy photons. This limits our sensitivity to the monochromatic peaks expected in the spectrum from two-body radiative decays to branching fractions of the order of 1% or higher.

We have set an upper limit at a moderately interesting level on the inclusive branching fraction $B(J/\psi \to \gamma X(1450))$ of 14.8×10^{-3}, and thus a lower limit on the branching fraction of this composite structure to $K\bar{K}\pi$ of approximately 35%. The masses of the $X(1450)$ states are low enough that there are only a limited number of exclusive final states available for their decay. Many of these have been accounted for already by the Mark III and other experiments. Some of them, however, most notably $K\bar{K}\pi\pi$ and $K\bar{K}\pi\pi\pi$, have not yet been examined in detail. The results presented here cannot exclude the presence of modest branching fractions from the $X(1450)$ states through these or other channels. We would very much welcome a future high-precision measurement of the inclusive photon spectrum in order to settle this question.

The upper limits on the inclusive radiative branching fractions $B(J/\psi \to \gamma f_0(1710))$ and $B(J/\psi \to \gamma X(2230))$ are at the considerably less interesting levels of 23 and 75 times the known exclusive branching fractions to these states, respectively. These limits provide few meaningful constraints on the possible interpretation of these states, as they are sufficiently large that, were the true inclusive branching fractions near the upper limits, these states would very likely already have been observed in other exclusive decay channels.

Appendix A The Track Recognition Dictionary

The drift chamber track finding algorithm recognizes tracks by comparing the hits in the detector to a dictionary of hit patterns of valid tracks. The algorithm operates on cells within drift chamber layers, rather than on individual wires. This provides a certain amount of robustness in the face of the presence of inefficient wires, since the definition of a "hit cell" does not require all the wires in the cell to be hit. The dictionary patterns are then generated assuming perfect detection efficiency at the cell level. This is not entirely satisfactory, however, because it is possible to miss an entire cell due to wire inefficiencies, and because tracks with large dip angles exiting through the end walls of the drift chamber will appear to miss its outer layers. There is therefore a provision for missing cells along found tracks.

The dictionary patterns are built from cells in the axial layers only, excluding Layer 8. For layers 3, 5, and 7, hit cells are defined as cells with at least two of their three wires hit. Layer 2 is split into two sublayers, 2A and 2B,[1] consisting of the inner and outer six, respectively, of the twelve wire cylinders in the layer. Within these sublayers, hit cells are defined as cells with at least four of their six wires hit. Layer 1 is also divided into two sublayers, defined in terms of the four wire cylinders, 1a, ..., 1d. Since adjacent cylinders in Layer 1 are offset azimuthally by ½ cell, alternate cylinders, which are aligned, are grouped together to form the sublayers: sublayer 1A is the combination 1a–1c, and sublayer 1B is the combination 1b–1d. A sublayer cell is considered hit if at least one of its two wires is hit.

The dictionary is a binary file which, once built, is permanently stored and is then loaded every time the track reconstruction package is initialized. The file is actually

---

[1] Note that the sublayers in Layer 2 defined for the purposes of the dictionary are different from those defined in the drift chamber data acquisition: sublayers 2a ... 2d, each composed of three wire cylinders (see Chapter 4).

built by a separate stand-alone program. This program has only one readily adjustable parameter: the pattern of missing cells permitted. Missing-cell patterns are defined by considering the ideal sequence of layers (1A, 1B, 2A, 2B, 3, 5, 7) along a track and then enumerating the layers or combinations of layers in which cells are to be permitted to be missing. The pattern thus defined is applied to all tracks in the dictionary; there is no provision for, *e.g.*, varying the missing-cell conditions as a function of the transverse momentum of a track.

Table A.1 displays the missing-cell patterns permitted in the track reconstruction of the data used in this work. The shaded patterns are those added to the original set, as described in Chapter 5, in order to increase the detection efficiency for converted photons. The original patterns required that a photon convert before reaching Layer 1d in order that the resulting electron and positron be recognized by the track-finding program. The added patterns permit the detection of tracks resulting from conversions in the outer wall of Layer 1 or the inner wall of the main drift chamber. The 3–miss pattern ensures that the angular acceptance for such conversions is not limited to those tracks which reach Layer 7 before exiting the drift chamber.

Table A.1 Required patterns of cells on found tracks, showing the cells permitted to be missing for the track recognition dictionary used in the reconstruction of the data for this analysis. The shaded patterns are those which were added in order to improve the detection efficiency for converted photons. A bullet indicates that a hit in the designated layer or sublayer is required for the pattern to be satisfied.

	Layer or Sublayer						
Missing Cells	1A	1B	2A	2B	3	5	7
0	•	•	•	•	•	•	•
1		•	•	•	•	•	•
	•		•	•	•	•	•
	•	•		•	•	•	•
	•	•	•		•	•	•
	•	•	•	•		•	•
	•	•	•	•	•		•
	•	•	•	•	•	•	
2	•	•	•	•	•		
		•	•	•	•	•	
	•		•	•	•	•	
			•	•	•	•	•
3			•	•	•	•	

Bibliography

[1] J. J. Aubert et al. Experimental Observation of a Heavy Particle *J. Phys. Rev. Lett.*, **33**(23):1404–1406, 1974.

[2] J.-E. Augustin et al. Discovery of a Narrow Resonance in e^+e^- Annihilation. *Phys. Rev. Lett.*, **33**(23):1406–1408, 1974.

[3] M. K. Gaillard, B. W. Lee, and J. L. Rosner. *Revs. Mod. Phys.*, **47**:277, 1975.

[4] G. Goldhaber et al. *Phys. Rev. Lett.*, **37**:255, 1976.

[5] I. Peruzzi et al. *Phys. Rev. Lett.*, **37**:569, 1976.

[6] S. L. Glashow, J. Iliopoulos, and L. Maiani. Weak Interactions with Lepton-Hadron Symmetry. *Phys. Rev. D*, **2**(7):1285–1292, 1970.

[7] G. Eigen. Experimental Status of J/ψ Decays. In Ugo Gastaldi, Robert Klapisch, and Frank Close, editors, *Spectroscopy of Light and Heavy Quarks*, volume 37 of *Ettore Majorana international science series*, New York, 1989. Plenum Press. Proceedings of the second course of the International School of Physics with Low Energy Antiprotons on Spectroscopy of Light and Heavy Quarks, held May 23–31, 1987, in Erice, Italy. See also references therein.

[8] L. Köpke and N. Wermes. J/ψ Decays. *Physics Reports*, **174**:67–227, 1989. See also references therein.

[9] S. Okubo. *Physics Letters*, **5**:165, 1963.

[10] G. Zweig. Technical Report CERN-TH-401, 402, 412, CERN, 1964.

[11] J. Iizuka. *Prog. Theor. Phys. Suppl.*, **37–38**:21, 1966.

[12] K. Koller and T. Walsh. Gluons in Quarkonium Decay. *Nucl. Phys.*, **B140**:449–467, 1978.

[13] C. J. Biddick et al. Inclusive γ-ray Spectra from $\psi(3095)$ and $\psi'(3684)$ Decays. *Phys. Rev. Lett.*, **38**(23):1324–1327, 1977.

[14] J. S. Whitaker et al. Radiative Decays of $\psi(3095)$ and $\psi(3684)$. *Phys. Rev. Lett.*, **37**(24):1596–1599, 1976.

[15] G. S. Abrams et al. Measurement of High-Energy Direct Photons in ψ Decays. *Phys. Rev. Lett.*, **44**(3):114–118, 1980.

[16] D. L. Scharre et al. Direct Photon Production at the ψ. *Phys. Rev. D*, **23**(1):43–55, 1981.

[17] R. D. Field. The Direct Photon Spectrum in the Inclusive Decay of the Upsilon. *Phys. Lett.*, **133B**:248, 1983.

[18] D. M. Photiadis. The Photon Spectrum in Upsilon Decay for $z \to 1$. *Phys. Lett.*, **164B**:160, 1985.

[19] C.-H. Chang, G.-P. Chen, Y.-P. Kuang, and Y.-P. Yi. Nonperturbative Approach to the Direct Photon Spectrum near $x = 1$ in the Inclusive Radiative Decay of J/ψ. *Phys. Rev. D*, **42**:2309, 1990.

[20] Elliott D. Bloom and Charles W. Peck. Physics with the Crystal Ball Detector. *Ann. Rev. Nucl. Part. Sci.*, **33**:143–197, 1983. See also references therein.

[21] Particle Data Group. Review of Particle Properties. *Physics Letters B*, **239**:1–516, 1990.

[22] D. L. Scharre et al. Observation of the Radiative Transition $\psi \to \gamma E(1420)$. *Phys. Lett.*, **97B**(2):329, 1980.

[23] C. Edwards et al. Identification of a Pseudoscalar State at 1440 MeV in J/ψ Radiative Decays. *Phys. Rev. Lett.*, **49**:259–262, 1982.

[24] Jeffrey D. Richman. *A Study of the iota in Radiative J/ψ Decays*. Ph.D. thesis, California Institute of Technology, 1985.

[25] Z. Bai et al. Partial-Wave Analysis of $J/\psi \rightarrow K_S^oK^{\pm}\pi^{\mp}$. *Phys. Rev. Lett.*, **65**(20):2507–2510, 1990.

[26] C. Edwards et al. Evidence for an $\eta\eta$ Resonance in J/ψ Radiative Decays. *Phys. Rev. Lett.*, **48**:458–461, 1982.

[27] Melissa E. B. Franklin. *Selected Studies of Charmonium Decay*. Ph.D. thesis, Stanford University, 1982. Published as SLAC preprint SLAC-254.

[28] R. M. Baltrusaitis et al. Radiative Decays of the J/ψ into $\gamma\pi^+\pi^-$ and γK^+K^-. *Phys. Rev. D*, **35**(7):2077–2091, 1987.

[29] J. E. Augustin et al. Measurement of Radiative J/ψ Decays in $K\bar{K}$ States. *Phys. Rev. Lett.*, **60**:2238–2241, 1988.

[30] Liang-ping Chen. An Amplitude Analysis of the $K\bar{K}$ and $\pi^+\pi^-$ Systems ($M <$ 2 GeV/c^2) Produced in J/ψ Radiative Decay. Technical Report SLAC-PUB-5669, Stanford Linear Accelerator Center, 1991.

[31] Burton Richter. The Stanford Storage Ring — SPEAR. Technical Report SLAC-PUB-780, Stanford Linear Accelerator Center, 1970.

[32] J. Voss et al. The SLAC Storage-Ring Project — SPEAR. Technical Report SLAC-PUB-965, Stanford Linear Accelerator Center, 1971.

[33] M. A. Allen et al. SPEAR: Status and Improvement Program. Technical Report SLAC-PUB-1424, Stanford Linear Accelerator Center, 1974.

[34] M. A. Allen et al. SPEAR II Performance. Technical Report SLAC-PUB-1562, Stanford Linear Accelerator Center, 1975.

[35] K. Wille. A Proposed Mini Beta Insertion for SPEAR. Technical Report SLAC/AP–9, Stanford Linear Accelerator Center, 1984.

[36] Frank Porter. Private communication, 1991. Some SPEAR parameters not available in the literature were calculated using Prof. Porter's `MACHINE` storage ring

calculator program. I thank him for his assistance.

[37] D. Coffman et al. A Direct Measurement of the J/ψ Leptonic Branching Fractions. Technical Report SLAC-PUB-5592, Stanford Linear Accelerator Center, 1991. Submitted to Phys. Rev. Lett.

[38] G. T. Blaylock et al. Observation of $e^+e^- \rightarrow D_s^\pm D_s^{*\mp}$ at $\sqrt{s} = 4.14$ GeV. *Phys. Rev. Lett.*, **58**(21):2171–2174, 1987.

[39] J. Adler et al. A Reanalysis of Charmed D Meson Branching Fractions. *Phys. Rev. Lett.*, **60**:89, 1988.

[40] R. M. Baltrusaitis et al. Decays of the J/ψ into Two Pseudoscalar Mesons. *Phys. Rev. D*, **32**(3):566–574, 1985.

[41] David Hitlin. A Third Generation Detector for SPEAR. *Physica Scripta*, **23**:634–641, 1981.

[42] D. Bernstein et al. The Mark III Spectrometer. *Nucl. Instr. Meth.*, **226**:301–318, 1984.

[43] J. Adler et al. The Mark III Vertex Chamber. *Nucl. Instr. Meth. A*, **276**:42, 1989.

[44] J. Roehrig et al. The Central Drift Chamber for the Mark III Detector at SPEAR. *Nucl. Instr. Meth.*, **226**:319–329, 1984.

[45] J. S. Brown et al. The Mark III Time-of-Flight System. *Nucl. Instr. Meth.*, **221**:503–522, 1984.

[46] Walter Toki et al. The Barrel Shower Counter for the Mark III Detector at SPEAR. *Nucl. Instr. Meth.*, **219**:479–486, 1984.

[47] R. Fabrizio et al. The Endcap Shower Counters for the Mark III Detector. *Nucl. Instr. Meth.*, **227**:220–226, 1984.

[48] Daniel M. Coffman. *The Properties of Semileptonic Decays of Charmed D Mesons.* Ph.D. thesis, California Institute of Technology, 1987.

[49] Anthony L. Spadafora. *Phi Meson Production in J/psi Decays and Determination of the Spin and Parity of the eta-c(2980)*. Ph.D. thesis, University of Illinois, 1984.

[50] J. Thaler et al. *IEEE Trans. Nucl. Sci.*, **NS–30**:236, 1982.

[51] S. Neddermeyer et al. *Rev. Sci. Inst.*, **18**:488, 1947.

[52] A. Seiden et al. Cosmic Ray Trigger Circuit for Large Solenoidal Particle Detectors. Technical Report SCIPP 81/2, Institute for Particle Physics, University of California at Santa Cruz, 1981.

[53] F. A. Berends and R. Kleiss. Distributions for Electron-Positron Annihilation into Two and Three Photons. *Nucl. Phys.*, **B186**:22–34, 1981.

[54] William S. Lockman. BWGNEW 2.1 User's Guide. Technical Report SCIPP-89/08, Santa Cruz Institute for Particle Physics, 1990.

[55] Liang-ping Chen. *An Amplitude Analysis of the $K\bar{K}$ System ($M < 2\,GeV/c^2$) Produced in J/ψ Radiative Decay*. Ph.D. thesis, Vanderbilt University, 1991.

[56] R. M. Baltrusaitis et al. Observation of a Narrow $K\bar{K}$ State in J/ψ Radiative Decays. *Phys. Rev. Lett.*, **56**(2):107–110, 1986.